

High-Content Analysis Approach for phenotypic Screening and Characterization of Histone H3 Lys27 Trimethylation Modulation in Cancer Cells

vorgelegt von
M.Sc. Svenja Lünse
geb. in Hamburg

von der Fakultät III – Prozesswissenschaften
der Technischen Universität Berlin
zur Erlangung des akademischen Grades

Doktor der Ingenieurwissenschaften
- Dr.-Ing. -
genehmigte Dissertation

Promotionsausschuss:

Vorsitzender: Prof. Dr. P. Neubauer
Gutachter: Prof. Dr. R. Lauster
Gutachter: Dr. B. Haendler
Gutachter: Prof. Dr. J. Rappsilber

Tag der wissenschaftlichen Aussprache: 11. Juli 2014

Berlin 2015

The present work was performed from September 2010 to December 2013 in the department Lead Discovery Berlin-Screening, High-Content Analysis I, Bayer Pharma AG, under the supervision of Dr. Stefan Prechtel.

Für meine Familie

Acknowledgement

A number of people contributed to the success of this work by supporting me in their own personal way. To start, I would like to express my sincere gratitude to my supervisor Dr. Stefan Prechtel for his unlimited support and guidance. I thank him particularly for allowing me to work independently while encouraging me to think outside the box.

I would like to give my special thanks to Dr. Carlo Stresemann for his unlimited support, constructive criticism and inspiration.

Also, a huge thank you to Professor Roland Lauster and Dr. Bernard Haendler for their support and evaluation of the work.

Many thanks to the Screening Department and, especially the HCA group, for the familiar work atmosphere. To Sebastian Raese for his support in journaling and image analysis, to Marc Osterland and my desk neighbor Alexander Kaminke for their help at all times.

I would especially like to thank Dr. Karsten Parczyk, Director of the Screening Department, for the opportunity to conduct this work at Bayer and for his support.

I would like to thank Petrina Bertram for her technical assistance.

Many thanks to the PhD and postdoctoral students at Bayer Pharma AG for their helpful and inspiring thoughts, the journeys in our free time, and their friendship.

And, finally, never enough thanks to my family and friends for their unconditional wholehearted support.

Svenja Lünse, Berlin 2014

Content

1.	Introduction.....	- 1 -
1.1	Definition of the term epigenetics	- 1 -
1.2	Posttranslational methylation of histone molecules.....	- 1 -
1.3	The histone code hypothesis.....	- 3 -
1.4	The repressive mark H3K27me3 and Polycomb-regulated gene-silencing.....	- 4 -
1.5	The maintenance of H3K27me3 through DNA replication	- 6 -
1.6	The link of EZH2 and other HKMTs to cancer.....	- 8 -
1.7	Drug discovery and Screening	- 11 -
1.8	Methods for the analysis of histone modifications.....	- 12 -
1.9	High-Content-Analysis	- 13 -
1.10	Aim of the study	- 14 -
2.	Material and methods.....	- 16 -
2.1	Cell biological methods	- 16 -
2.1.1	Cell lines and maintenance.....	- 16 -
2.1.2	siRNA mediated downregulation of different HKMTs	- 16 -
2.1.3	Compound plate preparation and compound addition	- 17 -
2.1.4	Immunofluorescence.....	- 17 -
2.1.5	Chromatin staining	- 18 -
2.1.6	EdU detection	- 18 -
2.1.7	High-Content Analysis using the Opera Reader™ (Perkin Elmer)	- 19 -
2.1.7.1	Algorithm I: Nuclei segmentation and methylation profile	- 20 -
2.1.7.2	Algorithm II: Cell scoring and methylation profile	- 22 -
2.1.7.3	Algorithm III: Cell cycle classification and methylation profile.....	- 24 -

2.2	Molecular biological methods.....	- 26 -
2.2.1	RNA isolation, concentration and quality determination.....	- 26 -
2.2.2	Reverse Transcription (cDNA-Synthesis).....	- 27 -
2.2.3	Semi-quantitative Real-Time PCR (qRT-PCR).....	- 27 -
2.3	Biochemical methods.....	- 28 -
2.3.1	BCA protein assay	- 28 -
2.3.2	SDS-Polyacrylamide-gel-electrophoresis	- 28 -
2.3.3	Cell lines and maintenance.....	- 29 -
2.3.4	Immune detection	- 29 -
2.3.5	Data analysis	- 30 -
3.	Results	- 31 -
3.1	Development and validation of a histone methylation HCA assay	- 31 -
3.1.1	Phenotypic evaluation of siRNA-mediated HKMT knockdown	- 31 -
3.1.2	Analysis of chromatin modulation induced by small-molecule inhibitors	- 37 -
3.2	Functional investigation of induced H3K27me3 suppression	- 48 -
3.2.1	Characterization of induced H3K27me3 suppression	- 48 -
3.2.2	Search of mechanisms involved in induced H3K27me3 reduction	- 53 -
3.2.3	Investigation of H3K27me3 recovery	- 60 -
4.	Discussion.....	- 66 -
4.1	HKMT HCA assay	- 66 -
4.1.1	Global versus local histone modification levels.....	- 66 -
4.1.2	Mechanistic assay validation	- 67 -
4.1.2.1	A symmetrical antagonistic course for H3K27ac.....	- 68 -
4.1.3	Technical assay quality.....	- 69 -

4.1.4	Evaluation of the EZH2 HCA assay	- 71 -
4.2	Characteristics of H3K27me3 reduction in response to EZH2 inhibition	- 72 -
4.2.1	Identification of a dynamic, cell cycle independent H3K27me3 fraction.....	- 72 -
4.2.2	Distinct separation of H3K27me3 reduction and proliferative effects.....	- 76 -
4.2.3	Reversibility of H3K27me3 modulation.....	- 80 -
4.3	Outlook.....	- 83 -
5.	Summary	- 85 -
6.	Appendix	- 88 -
6.1	Follow up: Miniaturization and automation for HTS purposes.....	- 88 -
6.2	Proliferation of the cell lines HeLa S3, MDA-MB-231 and MCF-7	- 89 -
6.3	Materials and reagents.....	- 89 -
6.3.1	Applied chemical compounds	- 89 -
6.3.2	siRNA (small interfering RNA).....	- 90 -
6.3.3	TaqMan [®] -assays	- 91 -
6.3.4	Antibodies.....	- 92 -
6.3.5	Chemicals and reagents.....	- 93 -
6.3.6	Kits	- 94 -
6.3.7	Materials.....	- 95 -
6.3.8	Devices.....	- 95 -
7.	Abbreviations	- 97 -
8.	Figures and tables	- 100 -
9.	References	- 104 -

1. Introduction

1.1 Definition of the term epigenetics

Epigenetics is defined by stably heritable changes in phenotype or gene expression in an organism or cell, resulting from changes in a chromosome that are not caused by a change in DNA sequence. It can be molecularly and mechanistically defined as the sum of alterations to the chromatin template that mutually establish and propagate different patterns of gene expression and silencing from the same genome [22, 23]. However, the term is very often used more loosely, referring to elements of chromatin structure that control genome function, regardless of whether the control is heritable *rev.* [24].

1.2 Posttranslational methylation of histone molecules

Histones are a group of highly evolutionarily conserved proteins that play a critical role in the proper packaging of DNA within the eukaryotic nucleus. DNA (~147 bp) wound around a histone core containing two copies of the histone proteins H2A, H2B, H3 and H4, form the fundamental repeating subunit of chromatin, known as the nucleosome [25-27]. The human genome is composed of around three billion bases of DNA; it is likely that there are tens of millions of nucleosomes within a single human nucleus. Nucleosomes regulatory activity is mediated by a variety of factors including ATP-dependent chromatin remodeling complexes [28], *rev.* [29] or histone posttranslational modifications (PTMs) [30] *rev.* [31, 32].

Histones are subject to a wide array of PTMs, often located along their amino - terminal domains *rev.* [33]. Changes in chromatin structure, including the addition or removal of histone modifications, play a central role in eukaryotic transcriptional regulation *rev.* [34]. These PTMs are defined by the histone, the modified amino acid, its position in the polypeptide chain and the nature of the modification (e.g. trimethylation on lysine 27 of histone H3 is abbreviated to H3K27me3). Covalent histone modifications are transduced by histone-modifying enzymes (“writers”) and removed by antagonizing activities (“erasers”). Together, they govern a steady-state balance of the respective modification. Although not considered in this work, a third group of proteins are needed for epigenetic control; the “readers” which recognize the modified sites and signal downstream effects. “Writers” and

“erasers” are classified into families according to the type of enzymatic action they perform as for example: histone acetylases (HATs) and deacetylases (HDACs); histone kinases and phosphatases (PPTases), histone methyltransferases (HMTs) (comprising histone lysine methyltransferases (HKMTs) and histone arginine methyltransferases (HRMTs)), and, identified for some HKMTs, respective histone lysine demethylases (KDMs). Several of the histone modifying enzymes also target non-histone substrates [35, 36].

HKMTs act on lysine residues [37]. Over 50 human genes are known to encode HKMTs [38, 39]. HKMTs sequentially transfer a donor methyl group from the S-adenosyl-L-methionine (SAM) cofactor to the terminal amine of specific acceptor lysine residues on protein substrates [40, 41]. All of them, with the exception of the DOT1-like (DOT1L) HKMT, share the conserved SET domain, which contains the catalytically active site and allows binding by the SAM cofactor. The transfer of the donor methyl group from SAM to an acceptor peptide substrate generates S-adenosyl homocysteine (SAH) and a methylated histone side chain product *rev.* [21].

Unlike acetylation or phosphorylation of histones, histone methylation can be either activating or repressive towards transcription. Lysines can be subject to multiple methylations (mono-, di-, and tri-methylation), increasing the complexity of different nucleosomal methylated patterns. This combinational potential of methylated nucleosomes may be necessary to allow a transcriptional regulation which requires sequential and precisely timed events *rev.* [31, 42, 43]. The most characterized methylation sites are lysine 4 on histone H3 (H3K4), H3 (K9, K27, K36, K79) and H4K20. A methylation at H3K4, H3K36 and H3K79 is in general associated to an activation of transcription, while a methylation at the others is linked to repression [44-46].

Methylated lysine residues appear to be chemically more stable, having a much slower turnover rate, comparable to that of the entire histone (e.g. the half-life of H3K27me3 is approx. 3 days, whereas most acetyl groups at the four core histones exhibit a half-life of only a few minutes) [47-49]. Several tri-methylated residues in the histone H3 and H4 amino termini appear to have the potential to be stably propagated during cell divisions [50]. In fact, histone methylation was thought to be irreversible before the discovery of the first histone demethylase, the flavin-dependent monoamine oxidase lysine-specific demethylase

(LSD-1) and later the JmjC-domain containing lysine demethylase family [51-53]. LSD-1 acts by FAD-dependent oxidative destabilization of the amino-methyl bond, resulting in the formation of unmodified lysine and formaldehyde. The enzyme was shown to specifically demethylate di- and monomethyl on histone H3 at K4, reversing an active chromatin mark, but it did not work on trimethylated H3K4. Further, LSD-1 interacts with the androgen receptor, promoting androgen-dependent transcription of target genes by demethylation of di- and monomethyl on histone H3 at K9 [54].

In contrary to LSD-1, JmjC-domain containing demethylases can also demethylate trimethylated lysines. The catalysis involves an oxidative mechanism requiring iron and 2-oxoglutarate as co-factors and probably occurs through direct hydroxylation of the affected methyl group [55, 56]. The timed regulation of genes is crucial throughout a cell's lifespan. Genes can be active at certain times, but inactive at other times. At present, histone methylation is considered to be a dynamically regulated process [57-59].

1.3 The histone code hypothesis

Histone modifications do not occur in isolation, but rather in a combinational manner. It has been hypothesized that PTMs may generate a “histone code” in which particular marks provoke a specific physiological response [32, 60] *rev.* [31]. The covalent PTMs arise in form of modification cassettes comprising adjacent residues but also different histone tails or different nucleosomes. Chromatin regulation may be accomplished either by directly altering the chromatin structure and charge or through modulation of binding of chromatin-associated proteins (“readers”) to the modification marks. These specific protein binders hold one of three distinct types of methyl lysine recognition domains: the chromo-, tudor-, and plant homeo- (PHD) domains. This binding causes down-stream alterations in the chromatin structure, consequently mediating processes such as gene expression, apoptosis, and DNA damage repair [61] *rev.* [62, 63].

Histone modifications correlate with activating or repressing function, dependent on which amino acid residue(s) in the histone amino - terminal domain the modification is located. Synergistic and antagonistic pathways are reported, which can lead to a combination of activating marks, while repressive marks were counteracted [64, 65] *rev.* [42]. However,

although specific modifications contribute to gene expression, other alternative views exist, arguing that clear combinatorial codes, comparable to the triplet genetic code, are not likely in histones. Evidence suggests that histone modification patterns are varying considerably from one organism to the other, indicating that if a histone code exists, it is not likely to be universal. Considering the dynamic nature of the PTMs in space and time complicates the conception of a combinatorial code even more *rev.* [66, 67].

Even though it is under debate if it is a true "code" formed by histone modifications [32] *rev.* [66, 68] , modifications appear in combination or cumulatively, defining and leading to biological functions *rev.*[66]. For instance, there exist strong correlations of H3K4me3 with activated promoter regions [32, 69, 70]. A methylation of H3K9 [71, 72] and H3K27 [73] is strongly correlated with silenced heterochromatin. Overall, it is suspected that both, specific combinations of PTMs and general net charge effects are mechanisms for a regulation of chromatin structure and gene expression [22].

1.4 The repressive mark H3K27me3 and Polycomb-regulated gene-silencing

During development or adult homeostasis, it is critical that the characteristic gene expression profiles are faithfully maintained, especially after each cell division. A large number of regulatory genes are classified. Among them, Polycomb group (PcG) proteins are required to maintain a silenced state of developmental regulators, originally discovered in *Drosophila* as regulators of *Hox* genes [74]. Alterations in these gene expression profiles distinguish stem cells from fibroblasts, signal-responding cells from unsigned cells, and healthy cells from malignant cancer cells *rev.* [75]. PcG proteins are organized into large multimeric complexes which act in consecutive steps on their target genes through chromatin modulation. The two best characterized polycomb-repressive complexes are Polycomb repressive complex 1 (PRC1) and PRC2. Once recruited, they establish a silent chromatin state which can be inherited over several cell divisions [76].

The multimeric complex PRC2 maintains the transcriptional repression of a large number of genes with key regulatory roles in development and differentiation [77] *rev.* [78]. It contains the HKMT EZH2 and at least two non-enzymatic partners: embryonic ectoderm development (EED) and the polycomb repressive complex 2 subunit (SUZ12) [79]. Moreover, it comprises

the two proteins AEBP2 in complex with either RBBP4 or RBBP7 [80] *rev* .[21, 81]. EZH2, as catalytic subunit of PRC2, mediates the repressive mark H3K27me3 in human cells. The enzyme is the human homolog of the *Drosophila* ENHANCER OF ZESTE [E(Z)] protein. EZH2 can catalyze each of the three successive methyltransfers that ultimately form the repressive mark H3K27me3. The HKMT can further methylate itself, as well as other proteins including H1 and GATA4 [5, 82]. EZH2 methylation of GATA4 attenuated its transcriptional activity by reducing its interaction with and acetylation by p300, thus, inhibiting its transcriptional activity [5].

Interestingly, it is impaired on substrates with preinstalled activating histone modifications. A preacetylation at H3K27 (H3K27Ac) for example provides a robust biochemically strategy to impede PRC2 output [83]. This preacetylation first needs to be removed by a HDAC to enable methylation of K27 by PRC2 and gene silencing, as illustrated in figure 1.1.

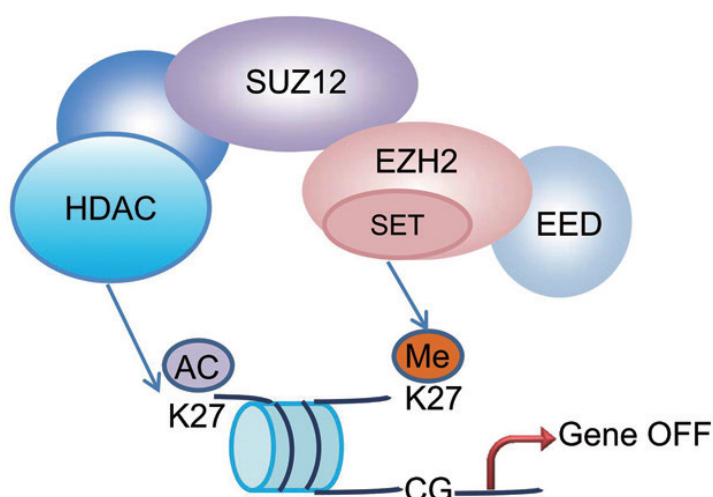


Figure 1.1: Gene silencing: a model for a collaboration of PRC2 and HDAC. H3K27 may show a preacetylation. HDAC may first deacetylates H3K27ac to enable methylation of K27 by EZH2. Ac, acetylation; Me, methylation. Figure adopted and modified from [38].

H3K27me3 and the monoubiquitylation of histone H2A on lysine 119 (H2AK119ub1) are the two key modifications that have been widely viewed as operative chromatin marks for PcG silencing [81, 84]. However, it is still not clear how exactly these two chromatin marks may somehow induce gene silencing. One common opinion is that H3K27me3 is a key recruiter of RPC1 to the target chromatin sites. PRC1 components recognize and bind the repressive methylation mark and induce structural changes in the chromatin sites via catalyzing H2AK119ub1 [65, 85]. H2AK119ub1 is supposed to play an important role in PRC1-mediated

gene silencing [84, 86, 87]. Moreover, it is suggested that EZH2 recruits DNA methyltransferases to promoter regions of PcG target genes strengthening gene silencing [88].

Besides, there may be other possible consequences of nucleosomes being modified with H3K27me3. Suggestions are: a recruitment of other silencing factors in addition to PRC1; an influence on nucleosome density, on nucleosome dynamics and on chromatin remodelers; and a prevention of the binding of transcriptional activators, initiation factors or elongation factors *rev.* [75, 89]. Furthermore, it is discussed if the two repressive marks H3K27me3 and H2AK119ub1 are rather correlative markers instead of inducers of the silent chromatin state [90] *rev.* [89, 91]. Although it has been shown that the inhibition of EZH2 is able to decrease global levels of the repressive mark H3K27me3, and thereby, reactivates silenced genes (e.g. upregulation of *TXNIP* and *TNFRSF21* *in vitro* and *in vivo* after treatment with GSK126) [92, 93], a study was recently reported which demonstrates that H3K27me3 accumulates after the onset of silencing of the well-established Polycomb target gene *CYP26a1* [90].

1.5 The maintenance of H3K27me3 through DNA replication

How the repressive H3K27me3 mark is initially established, reversed or maintained through an indefinite number of cell cycles is an important area of current research. For initial recruitment of PRC2, it is suggested that a sum of relatively weak interactions by each of the PRC2 complex partners function together to recruit PRC2 to a defined gene [94]. H3K27me3 is considered to be fine-tuned by the opposing activities of the PRC2 complex and the two H3K27-specific demethylases identified to date, the ubiquitously transcribed tetratricopeptide repeat (UTX) and Jumonji domain-containing protein 3 (JMJD3). The JmjC-domain containing demethylases UTX and JMJD3 have been suggested to enable a dynamic switch of transcriptional repression by active H3K27me2/3 demethylation [59, 95-98].

However, if a gene requires H3K27me3 for repression, the stability of H3K27me3 needs to be ensured throughout the cell cycle, in spite of intense chromatin reorganizations during DNA replication, but also histone exchange and demethylation. One model for repressive signal propagation is the described 'self- propagation' mechanism of PRC2, suggesting the ability of the PRC2 complex to bind its own mark to be key, as illustrated in figure 1.2 [99, 100]. The

PRC2 component, embryonic ectoderm development (EED), can bind H3K27me3 through an aromatic cage and the enzymatic activity of EZH2 becomes allosterically stimulated. Thus, pre-existing H3K27me3 activates the complex to carry out further methylation of unmodified H3K27 on nearby nucleosomes, generating a positive-feedback loop [99, 101, 102]. As a consequence, H3K27me3 becomes enriched during the early S-phase. After the replication is accomplished, an H3K27me3 redistribution on the daughter strands reestablishes H3K27me3 to the previous amount [102]. Yet, it is not known whether the initial recruitment of PRC2 and the maintenance of its H3K27me3 mark involve the same mechanisms *rev.in* [94].

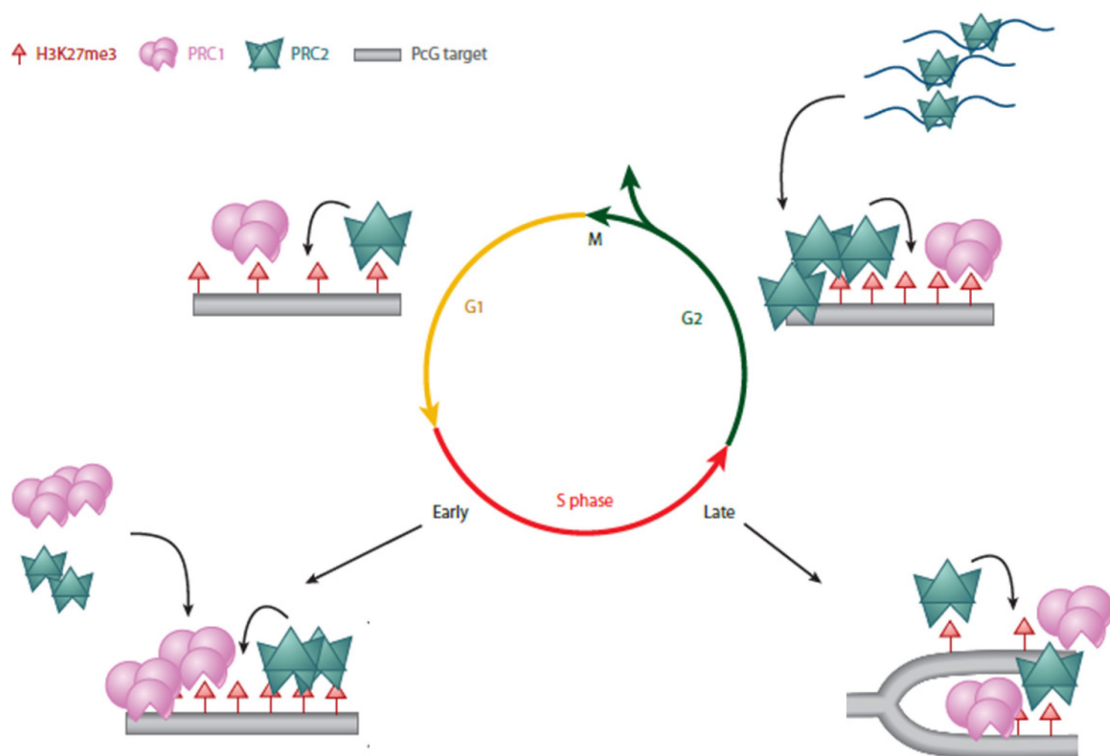


Figure 1.2: Model for the self- propagation mechanism of PRC2: Transmission of H3K27me3 through the cell cycle. In G1 phase, H3K27me3 sufficient for transcriptional repression is present on PRC2 target genes. In early S phase, PRC2 binds its own mark and EZH2 becomes allosterically activated to carry out further methylation on H3K27me3, as described in the text. Enriched H3K27me3 becomes redistributed on the daughter strands after replication to the previous level. Figure adopted and modified from [103]

1.6 The link of EZH2 and other HKMTs to cancer

A deregulation of epigenetic control, through misregulated HKMTs and resulting aberrant histone methylation patterns, is associated with a variety of diseases, including neurological diseases, autoimmune diseases and cancers *rev.* [104-106]. In several different tumor types, genetic alterations of HKMTs have been discovered leading to global aberrant patterns of histone modifications [107-109]. Table 1.1 displays a selection of characterized HKMTs which are found, if misregulated, to be implicated in several types of cancer.

The H3K27-specific HKMT EZH2 (also named as KMT6) of the multimeric complex PRC2, has been shown to be overexpressed in a number of various cancers, including breast, prostate and B-cell lymphoma [6, 7]. EZH2 overexpression and increased levels of H3K27me3 were correlated with poor prognosis and the promotion of metastasis in different solid tumors including breast, kidney, lung and prostate cancer [6, 7, 110-112]. Similarly correlated were inactivating mutations of its counterpart enzyme, the H3K27-specific demethylase UTX (also named as KDM6A) [113, 114]. In addition to this, heterozygous point mutations in the catalytic SET domain of EZH2 were shown to induce an uncommon gain of function in follicular and diffuse large B-cell lymphoma (DLBCL). ‘Gain-of-function’ point mutations resulting in a switch from tyrosine to histidine at Tyrosine 641 (Tyr641) in the catalytical active SET domain of the EZH2 protein were the most frequent mutation with up to 22% of the follicular lymphoma and DLBCL cases, respectively [4]. Here, mutated EZH2 showed a shift in its substrate preference. Cooperation between wild type (WT) and Tyr641 mutant EZH2 is boosting the repressive trimethylated state of H3K27 [4, 115, 116]. While WT EZH2 is most efficient at catalyzing monomethylation of non-methylated H3K27, the EZH2 Tyr641 mutant enzymes have the opposite substrate preference and are most efficient at catalyzing the conversion of dimethylated H3K27 into trimethylated H3K27 [3, 117]. Overall, EZH2 overexpression or point mutations lead to aberrant H3K27me3 methylation in different tumor types, demonstrating a repression of different tumor-suppressor genes [118]. It has been shown that the inhibition of EZH2 is able to decrease global levels of the repressive mark H3K27me3, and thereby, reactivates silenced tumor suppressor genes [92, 93]. A small-molecule inhibitor of HKMTs, as for EZH2 and its repressive mark H3K27me3, is therefore

regarded as promising therapeutic cancer intervention, reversing the oncogenic state. [92, 119, 120].

Another HKMT is DOT1L (also named as KMT4), which specifically methylates the core histone H3 residue lysine 79 (H3K79). DOT1L lacks a SET domain, commonly present in HKMTs, but the enzyme can catalyze a transfer of one, two or three methyl groups to the amino -terminal domain of H3K79. A mistargeting of DOT1L contributes to a transcriptional activation of different genes implicated in the initiation and development of MLL-rearranged leukemia, as described further below [1, 121].

Table 1.1: Selected HKMTs and their disease indications:

Chromatin-binding protein	Modifications	Disease indications
DOT1L (KMT4)	H3K79	Various cancers including mixed lineage leukemia [1, 2]
EZH2 (KMT6)	H3K27me1/2/3, including H1 and GATA4	Various cancers including breast, prostate and B-cell lymphoma [3-7]
G9a/GLP1 (EHMT2/1; KMT1C/D)	H3K9me1/2 P53K3373	Various cancers including lung, prostate, colon and hepatocellular carcinoma [8, 9]
MLL1/2 (KMT2A/ KMT2B)	H3K4	lymphoid and myeloid leukemia [10, 11]
NSD1 (KMT3B)	H3K36 and H3K20	acute myeloid leukemia, multiple myeloma, and lung cancer [12-17].
SMYD2 (KMT3C)	H2B, H3, H4 p53K370 and other proteins	Various cancers including esophageal squamous-cell [19, 20].

The HKMT G9a (also named euchromatin histone methyltransferase 2 (EHMT2)) catalyzes the methylation of the histone protein H3 on lysine 9 (H3K9), generating a repressive methylation mark. G9a and the catalytic enzyme GLP1 (also named euchromatin histone methyltransferase 1 (EHMT1)) form heteromeric complexes via their SET domains, to yield H3K9 HKMT activity [122]. Misregulated G9a leads to increased levels of methylated H3K9 in the promoter regions of tumor suppressor genes leading to aberrant silencing in different

cancer cells [123]. G9a is upregulated in several cancers including lung, prostate, colon and hepatocellular carcinoma [124].

Activating methylation marks at H3K4 are catalyzed by a number of different HKMTs in mammals, including the MLL family MLL1-5 (mixed-lineage leukemia proteins). The MLL1 gene (also named as KMT2A) is very frequently rearranged in human lymphoid and myeloid leukemia. The protein is implicated in more than 50 chromosomal translocations, usually associated with poor prognosis [10, 11]. One common feature in different oncogenic MLL1-fusions is the loss of the SET domain harboring the HKMT activity for H3K4 methylation [125]. MLL1-fusion proteins still upregulate gene expression of several target genes via their translocation partners, which is suggested to be essential for its oncogenic potential [126]. A transformation by the fusion protein MLL1-DOT1L, for example, results in a mistargeting of DOT1L with a subsequent change in the PTM pattern from H3K4 to H3K79, leading to aberrant activation of leukemia-relevant genes [121, 126]. Mutations in MLL2 (also named as KMT2B) have been associated with tumor initiation and progression too [127].

The HKMT NSD1 (also named KMT3B) is a member of the nuclear receptor binding SET domain family (NSD) which consist three NSD proteins in total (NSD1-3). NSD1 specifically methylates H3K36 and H3K20 [128]. The NSD family has been suggested to play an important role in chromatin integrity. However, an alteration in the loci of NSD genes or the aberrant expression of the enzyme is associated with a number of diseases including cancer. NSD1 is involved in translocations of a nucleoporin gene (*NUP98*) in childhood acute myeloid leukemia with the NUP98-NSD1 fusion protein being an active H3K36-methyltransferase. The HKMT is associated with acute myeloid leukemia, multiple myeloma, and lung cancer [12-17].

SMYD2 (SET and MYND domain-containing protein 2 or also named as KMT3C) methylates histones (H2B, H3 and H4) and other proteins, as for example the tumor suppressor p53 and Rb [129, 130]. Some defined roles have been established for SMYD2 in cancer. In esophageal squamous-cell carcinoma, for example, higher SMYD2 levels correlate with tumor cell proliferation and survival rates, demonstrating oncogenic potential of the HKMT [19, 20].

Large efforts have been made in order to identify probe molecules for chromatin-modifying enzymes like HKMTs, aiming to investigate their role in normal physiology and pathology and, eventually, to find and optimize drug candidates for the clinic [21, 38, 131]. It still has been challenging to develop cell-based assays amenable to screening for HKMT inhibitors and compound profiling, as described in chapter 1.7 and 1.8. Nevertheless, several selective and highly potent EZH2 inhibitors were disclosed by the end of 2012 [38]. They are summarized in table 1.2 together with selective and highly potent small-molecule inhibitors targeting the HKMTs DOT1L and G9a. To identify inhibitors of the mentioned HKMTs, high-throughput biochemical screening experiments have been performed (e.g. using the PRC2 complex). A most potent inhibitor of EZH2 thus far is GSK126. Its selectivity for EZH2 is more than 1000-fold higher than its selectivity for 20 other human HKMTs. The selective EZH2 inhibitor EPZ-6438 (E7438) is currently being tested in Phase II clinical trials for treatment of diffuse large B cell lymphoma [132] *rev.* [38]. For the DOT1L inhibitor EPZ-5676, clinical trials have been initiated in patients with acute leukaemia [133] *rev.*[21].

Table 1.2: Small-molecule inhibitors of selected HKMTs:

Chromatin-binding protein	Small-molecule inhibitors
DOT1L (KMT4)	EPZ004777, EPZ-5676, SGC0946
EZH2 (KMT6)	GSK126, GSK343, EPZ005687, EPZ-6438, EI1, UNC1999
G9a/GLP1 (EHMT2/1)	BIX01294, UNC0321, UNC0638, NC0642, BRD4770

Table altered from *rev.* [21]

1.7 Drug discovery and Screening

The goal of a drug discovery approach is the development of safe and efficacious therapeutics for the treatment of various human diseases. The early drug discovery approach often starts with the identification of a drug-target, relevant to the disease of interest. A drug-target can be, for instance, an abnormal function of a specific protein, an aberrant signaling pathway, or a mutation in a specific gene, identified in basic research and linked to a specific disease [134]. After target identification and validation, the assay development is conducted. Here, a biochemical or cellular assay will be developed and validated, amenable

for a miniaturization and automation, so that the assay can be applied for High-Throughput-Screening (HTS) *rev. in* [135]. HTS is the fast measurement of many experimental steps, describing the use of the assay to screen large compound libraries, composed of up to 3 million compounds [136] *rev. in* [137]. The aim is to find a drug molecule, which can potentially interact and affect the identified and validated target. Orthogonal assays are subsequently used to confirm and validate the most effective compounds [136]. In the following steps, the very few compounds of interest will be chemically optimized to determine the structure-activity relationship (SAR) and to optimize characteristics such as absorption, distribution, metabolism, and excretion (ADME) and pharmacokinetic / pharmacodynamic properties of the compounds [134] *rev. in* [137]. If appropriate compounds have been gained successfully throughout this process, they will be further processed in preclinical drug development, toxicology studies and eventually in clinical trials. The most common molecular targets are G-protein-coupled receptors (GPCRs), ion channels and enzymes [138-141]. A traditional approach to develop a drug until approval of the food and drug administration (FDA) usually takes up to 10-15 years [134].

1.8 Methods for the analysis of histone modifications

Traditionally, the analysis of histone modifications has been conducted using site-specific antibody-based methods such as western blot analysis or enzyme-linked immunosorbent assay (ELISA) measuring global levels of PTMs. Targeted or large-scale gene expression analyses are chromatin immunoprecipitation (ChIP) [142-144] coupled to PCR, DNA microarrays (CHIP) [145, 146] and deep sequencing (Seq.) [147-149]. Additionally, quantitative mass spectrometry-based methods are described, representing a sensitive method enabling an unbiased analysis of also yet unknown histone modifications [150] *rev.*[151, 152].

Although mass spectrometry is reported to offer the ability to examine PTMs in a high-throughput fashion *rev.*[151], it still has been challenging to develop cell-based assays amenable for HTS and compound profiling for the use in a drug discovery approach. Antibody based cellular assays for the detection of global H3K27me3 levels, which are amenable to HTS, are the LanthaScreen[®] assay and the AlphaLISA[®] assay (Perkin Elmer) [153, 154]. The AlphaLISA[®] assay is a chemiluminescent assay which uses luminescent oxygen-

channeling chemistry [155]. The Lanthascreen[®] assay comprises a terbium-based time resolved fluorescence resonance energy transfer (TR-FRET) technology in conjunction with the BacMam gene delivery system [155]. However, both assay systems detect exogenous levels of epigenetic markers from cellular extracts. Therefore, responses are averaged cell population effects and are, due to an additional cell lysis step, less close to the native cellular state.

1.9 High-Content-Analysis

High-Content-Analysis (HCA), as a phenotypic cellular assay, uses cellular imaging to collect quantitative datasets from complex biological systems in combination with an automated image analysis, using quantitative software analysis. Applying appropriate probes (e.g. antibodies, fluorescent protein fusion partners or biosensors), cellular and subcellular impact induced by external stimuli, as for instance small-molecule compounds or siRNA oligonucleotides, can be quantified. It represents an important tool in the drug discovery process with the clear benefit towards common cellular assays in generating biologically relevant and multi-parametric data sets with high statistical quality [137, 156, 157]. In contrast to traditional cellular assays, which average the biological response of thousands of cells, high content analysis acquires functional and morphometric information from a collection of individual cells which is representing one of the most important features in HCA [158]. In contrast to biochemical assays using purified recombinant proteins, HCA assays offer additional biological information, with the cellular context of interacting proteins and signaling networks. This leads to a high level of complexity comprising for example changes in cellular morphology, subcellular localization or expression level of a protein [159].

In general, a characteristic associated with the disease is exploited to develop a cell-based assay for HCA *rev.* [137]. Many diseases are associated with an altered activity or expression level of certain proteins due to disease status or genetic mutation, causing a misregulation of important cellular pathways or functions. Compounds will be screened for forming the desired phenotype, as for example, activating or inhibiting a signaling pathway or normalizing a phenotypic change associated with the disease (e.g. a reduction of the global level of specific histone modifications, as applied in this work). The most common cell-based

phenotypic assays performed in drug discovery are cell viability assays, cell signaling assays or disease-related phenotypic assays [160] *rev.* [137, 156, 161].

HCA in combination with the ability to perform a capacity of HTS is defined as High-Content-Screening (HCS) [162-164]. To enable HCS, robotic screening platforms and highly sensitive automated fluorescence imaging systems are used (e.g. the OPERA[®] reader by Perkin Elmer is used in this work), allowing the phenotypic assay to be miniaturized and used to screen large compound libraries. The assessment of large datasets is followed by an automated image analysis of the resulting fluorescence-based images, using quantitative software analysis (e.g. MetaXpress[®] by Molecular Devices or Acapella[®] by Perkin Elmer). Dealing with the complexity of intact cells, image analysis algorithms automatically extract multi-dimensional information from cellular images which can be categorized in fluorescence intensity changes, fluorescence distribution, morphology, and cell movement [157, 159]. This qualitative and quantitative information, such as number, intensity, size, morphology, texture or special distribution of single objects can be acquired for further statistical analysis [156]. HCS is integrated into all different stages of contemporary drug discovery, including primary compound screening, post-primary screening capable of supporting structure-activity relationships, early evaluation of ADME or toxicity properties and complex drug profiling *rev.* [157, 159].

1.10 Aim of the study

The main goal of this work was to establish an HKMT HCA assay, which would enable a monitoring of HKMT inhibitor effects on the physiology of single cells, suitable for screening of large compound libraries. To address this, siRNA nucleotides and small-molecule inhibitors, targeting different HKMTs, were to be applied to establish and validate an HKMT HCA assay, using different cancer cell lines. Downregulation of a set of HKMTs using siRNA was aimed to primarily prove the assay concept, in order to quantify a possible induced modulation of a respective histone methylation mark.

Based on the results gained from the siRNA mediated knockdown analysis, a HKMT was to be picked as the target enzyme to conduct the development of a HKMT HCA assay amenable to compound screening. With the established assay, different small-molecule inhibitors were

aimed to be characterized and benchmarked on their cellular activity for modulating histone H3 modification levels over broad inhibitor concentration ranges. Furthermore, the assay was to be applied to functionally investigate and characterize a small-molecule induced modulation (decrease and recovery) of a histone H3 modification and to possibly contribute to the understanding of the mechanisms involved.

2. Material and methods

2.1 Cell biological methods

2.1.1 Cell lines and maintenance

The cell lines MDA-MB-231 and MCF7 breast adenocarcinoma and HeLa S3 cervix adenocarcinoma were obtained from the American Type Culture Collection (ATCC). The PC3 prostate adenocarcinoma cell line was obtained from the Deutsche Sammlung von Mikroorganismen und Zellkulturen (DSMZ). All cell lines were maintained in the recommended media conditions at 37 °C in a humidified atmosphere (5% CO₂ and 95% air) and monthly tested for mycoplasma. The cells were cultivated using 25 cm², 75 cm² and 162 cm² cell culture flasks and passaged when 80-90% confluent. For passaging, the cells were washed using 10 ml DPBS and then treated with 2 ml trypsin. Excessive trypsin was removed and the cells were incubated for 2-5 min at 37 °C. Cell detachment was ensured via microscopy and the cells were diluted in fresh culture media and transferred into new cell culture flasks using a dilution factor of 1:5 to 1:15, depending on doubling times. For all experiments, viable cells were counted using the Casy (Innovatis) and plated 24 hours prior to siRNA or inhibitor treatment in 384-well plates at 20-50 µl/well volume or 6-well plates at 200 µl/well volume and at the desired cell densities.

2.1.2 siRNA mediated downregulation of different HKMTs

Different HKMTs were targeted by the use of siRNA-mediated knockdown. The used siRNA nucleotides are listed in table 6.22. For the transfection, the cells were plated in 96-well plates (200 µl volume) or 384-well plates (50 µl volume) in cell culture medium and incubated for over twenty -four hours at 37°C and 5% CO₂. On the next day, 75% of the medium was discarded and 50% fresh medium was added. The transfection reagent HiPerFect (Qiagen) was mixed with siRNA in serum-free medium (Opti-MEM[®] I Reduced Serum Media without phenol red, Life Technologies) and incubated at RT for 5-10 min. From the siRNA-transfection reagent mix, 25% of the starting volume was carefully added to the cells and the cells were incubated for over another twenty -four hours at 37°C and 5% CO₂. The medium containing the siRNA-transfection reagent mix was exchanged against fresh

culture medium. Depending on the experimental design, the cells were cultivated for another 24 hours, 48 hours or 72 hours. At various time points after the transfection, the cells were subjected to immunofluorescence analysis (cultivated in 384-well plates) or harvested for real-time quantitative PCR (cultivated in 96-well plates).

2.1.3 Compound plate preparation and compound addition

All compounds were stored at high concentration stock (10 mM) dissolved in dimethyl sulfoxide (DMSO) at -80°C. For the compound plate preparation, the compound stock was diluted in cell culture medium to the desired concentration. For IC₅₀ determination, serial compound dilutions were automatically prepared using the Biomek 2000 (Beckman Coulter). The final DMSO assay concentration was 0.3% at a maximum and was kept equal throughout the entire assay plate. One compound plate was used for several cell plates to ensure similar assay conditions and reducing assay variance. For the 384-well plates, compounds were added to the cells at 20 µl/well to achieve a final assay volume of 40 µl/well.

2.1.4 Immunofluorescence

The cells were fixated with 4% paraformaldehyde (PFA) for 15 min at RT. PFA fixated cells were washed three times using DPBS and permeabilized using the Permeabilisation buffer (all solutions are listed in table 2.1). After this, the cells were incubated with Blocking solution I for 1 hour at RT, followed by incubation with specific primary antibodies diluted in Blocking solution I for 16 hours at 4°C (all antibodies are listed in table 6.2.4). The cells were washed three times using DPBS and incubated with the secondary antibodies, diluted in Blocking solution II, for 1 hour at 37°C. For the DNA counter staining, see 2.1.5. Cells were washed three times using DPBS after each antibody or Hoechst incubation step. DPBS was added prior to the analysis using the automated confocal imaging system. For 384-well plates, antibodies and Hoechst were added at a volume of 20 µl/well. All liquid handling steps were executed using MultidropTM Combi Reagent Dispensers (Thermo Scientific) and the automated stand-alone pipettors CyBi[®]-Well (CyBio).

Table 2.1: Working solutions immunofluorescence:

Working solutions	
Permeabilisation buffer:	DPBS, 0.5 % Triton-X-100
Blocking solution I:	DPBS, 0.5 % Triton-X-100, 1 % BSA
Blocking solution II:	DPBS, 0.5 % Triton-X-100, 0.5 % BSA and immunoglobulin at 22 µg/ml

2.1.5 Chromatin staining

The cell-permeable nucleic acid dye Hoechst 33342 (Invitrogen) was used to stain the chromatin in PFA fixated cells. It binds to adenine and thymine- (AT) rich regions within the DNA [165]. It is excited by ultraviolet light at a maximum of 350 nm and emits blue fluorescence light at an emission maximum at 461 nm. With the Opera ReaderTM (Perkin Elmer), the wavelengths 405 nm for excitation and 450 nm for emission were used. Prior to the staining, the cells were fixated with 4% PFA for 15 min at RT. The fixated cells were washed three times using DPBS and were incubated for 10 minutes at RT using Hoechst 33342. Excessive Hoechst molecules were removed by washing three times with DPBS and DPBS was added prior to the analysis using the confocal imaging system. Using 384-well plates, Hoechst 33342 was added at a volume of 20 µl/well. All liquid handling steps were executed using MultidropTM Combi Reagent Dispensers (Thermo Scientific) and the automated stand-alone pipettors CyBi[®]-Well (CyBio).

2.1.6 EdU detection

The fluorescently labeled thymidine analogue EdU (5-ethynyl-2'-deoxyuridine) was used to detect cells which passed DNA replication during a certain time of inhibitor treatment. It incorporate into newly synthesized DNA. For EdU detection, the Click-iT[®] EdU Alexa Fluor[®] 488 Imaging Kit (Life Technologies) was used, according to the manufacturer's recommendation. A 10 mM stock solution of EdU, a working solution of Alexa Fluor[®] azide, a 1X Click-iT[®] EdU reaction buffer and 10X Click-iT[®] EdU reaction buffer additive were prepared as recommended (provided by the kit). The cells were plated in 384-well plates in cell culture

medium and incubated over twenty-four hours at 37°C and 5% CO₂. On the next day, the cells were treated with chemical inhibitors as stated in the experiments. EdU at a concentration of 20 µM was mixed with the culture medium containing the chemical inhibitor. The inhibitor/EdU mix was then added to the cells in culture with an equal volume per well resulting in a final EdU concentration of 10 µM. The cells were incubated at 37°C and 5% CO₂ as stated in the experiment. After that, the cells were fixated with 4% PFA for 15 min at RT. PFA fixated cells were washed three times using DPBS and permeabilized using the Permeabilisation buffer (see 2.1). After this, the cells were incubated with Blocking solution I for 1 hour at RT. The sample preparation for the detection of EdU is summarized in table 2.2, the addition order is important for the reaction.

Table 2.2: Click-iT[®] reaction solution:

Component	Reaction volume
Master Mix	4.0 µl
RNA template	up to 16 µl
Nuclease-free H ₂ O	ad to 20 µl
Total	20 µl

The cells were washed twice using DPBS. The Click-iT[®] reaction solution was added at 20 µl/well and the assay plate was incubated for 30 min at RT, protected from light and with gentle agitation. Following that, the cells were washed three times using DPBS, followed by incubation with specific primary antibodies diluted in Blocking solution I for 16 hours at 4°C. The following steps for the immunofluorescence were identical as described in 2.1.4.

2.1.7 High-Content Analysis using the Opera ReaderTM (Perkin Elmer)

HCA is an important tool in research and drug discovery, employing cellular imaging based on fluorescence microscopy in combination with automated image analysis, as described in chapter 1.8. External stimuli (e.g. a treatment with chemical compounds or siRNA oligonucleotides) can be quantified and characterized for modulating a chosen phenotype, as for example a reduction of the global level of specific histone modifications, as applied in this work. The imaging was conducted using the Opera ReaderTM (Perkin Elmer), a spinning disc

confocal microscope. High resolution digital images which display the fluorescent intensities over a broad range were acquired using three peltier cooled 12-bit CCD-(charged coupled device) cameras and up to three different lasers with different filter combinations simultaneously. Images were captured using the channels: Hoechst stain (DNA), DyLight™488 and/or DyLight™649 (for enzyme or modified histone H3-specific staining). A 12-bit digitalization shows 4096 intensity levels, allowing the image to display very dim to very bright fluorescent signals. Reference images for each fluorescence channel were made prior to the image acquisition to correct a possibly uneven field illumination. In order to ensure proper colocalization of the different fluorescent signals (to correct laser beam misalignment called pixel shift), images from control beats were acquired for all used lasers. Algorithm based correction of the pixel shift was conducted on every acquired image. All Opera Reader™ settings (e.g. acquisition of reference images, choice of wavelengths, choice of immersion objectives and binning) were set using the software Acapella 2.0. The Opera Reader™ was implemented in a fully robotic system (CRS Catalyst Robot, Thermo Scientific) enabling unattended imaging. For the analysis of the obtained images, developed algorithms, using the image analysis software MetaXpress® were applied.

2.1.7.1 Algorithm I: Nuclei segmentation and methylation profile

First of all, the regions of interest (ROI) to be quantified from the images needed to be recognized and marked. The standardized image-analysis module ("Count Nuclei") and the imaging fields from the DNA-channel (Nuclei stained with Hoechst) were used for the nuclei recognition, as exemplified in figure 2.1. Within this module, the boundaries of the stained nuclei were recognized by setting a gray-level threshold value, which discriminates noise from signal, as well as a minimum and a maximum diameter of the nuclei to be analyzed (figure 2.1, red rectangle). By choosing these parameters carefully, based on control cells (DMSO or transfection lipid treated cells), contiguous nuclei were segmented and recognized as single objects.

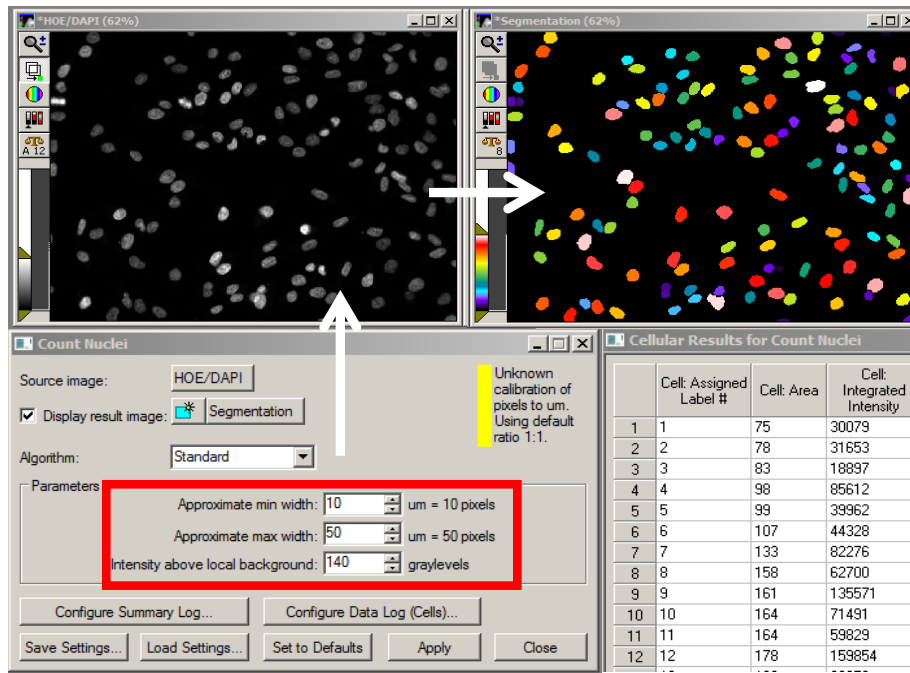


Figure 2.1: The standardized image-analysis module (“Count Nuclei”) provided by the image analysis software MetaXpress®. Nuclei from the DNA channel (monochromatic) were segmented and recognized as single objects using the “Count Nuclei” module. After conducting the entire algorithm I, results were exported to a spread sheet for further statistical analysis.

The algorithm I for nuclei segmentation and quantification of global histone modification levels started with the application of the described (“Count Nuclei”) module, as displayed in the figure 2.2. In the following, the segmented nuclei were filtered for size, shape and signal intensity to exclude possible non-viable cells (e.g. cell debris, recognized by size and shape) along with metaphase nuclei (recognized by size and increased signal intensity).

For further processing, the segmented nuclei were reduced to binary code (binary object mask), consisting of yes-(signal)- and no-(background)-information. Peripheral pixels were reduced to smooth signal edges and objects touching the image border were spared from the analysis. Finally, in order to locate the histone H3 modification-specific antibody signal to be quantified, the generated binary mask is used as a template to be superimposed over the respective fluorescent signal of the image set (identical pixel-x/y-coordinates). The nuclear integrated signal intensity (total signal intensity of the nucleus) was quantified for every nucleus in every image set and the results were exported to a spread sheet for further statistical analysis.

Use the "Count Nuclei" module for nuclei segmentation.

1: Overwrite "Segmentation" = Count Nuclei(Src="HOE/DAPI")

2: Threshold Image("Segmentation", 1, 16383, Inclusive)

Use generated segmentation mask to exclude objects, which are too small or too large. Create an object mask.

3: Integrated Morphometry - Load State("Filter nuclei size")

4: Integrated Morphometry - Measure([1: Count Nuclei])

5: Integrated Morphometry - Create Objects Mask()

Threshold object mask and create binary. Remove border objects and shrink objects by 1 pixel.

6: Threshold Image("IMA Objects Mask", 1, 16383, Inclusive)

7: New "binary nuclei" = Binarize("IMA Objects Mask"), high = current value, low = current value

8: Overwrite "Border Objects" = Suppress Light Border Objects([7: Binary Operations])

9: Overwrite "Distance Map" = Distance Map([8: Morphological Border Objects])

10: Threshold Image([9: Distance Map], 2, 16383, Inclusive)

11: Overwrite "Binary" = Binarize([9: Distance Map]), high = current value, low = current value

12: Close([1: Count Nuclei])

13: Close("IMA Objects Mask")

Subtract the created binary mask from the images showing modification-specific stained nuclei.

14: New "Arithmetic" = "Cy5" AND [11: Binary Operations]

15: Threshold Image([14: Arithmetic], 1, 16383, Inclusive)

16: Set Logging Row and Column(SUMMARY, RELATIVEROW and ABSOLUTE COLUMN, 0, 0)

Quantify the integrated signal intensity of the modification-specific staining for every selected nuclei.

17: Integrated Morphometry - Load State("IntegratedIntens")

18: Integrated Morphometry - Measure([14: Arithmetic])

19: Integrated Morphometry - Log Data([Last Result], SUMMARY, CURRENTDATA, 27, 2)

20: Close([11: Binary Operations])

21: Close([7: Binary Operations])

22: Close([14: Arithmetic])

23: Close([9: Distance Map])

*** End of Journal ***

Figure 2.2: Algorithm I: Nuclei segmentation and quantification of histone methylation mark. Nuclei from the DNA channel (monochromatic) were segmented and recognized as single objects using the "Count Nuclei" module. Generated binary object masks based on the nuclei segmentation were used to identify the nuclei of the methylation mark image set and nuclear integrated signal intensities were quantified.

2.1.7.2 Algorithm II: Cell scoring and methylation profile

The algorithm II was used to discriminate a cell population based on their expression of a protein (e.g. the HKMT EZH2) after siRNA transfection targeting EZH2, followed by a quantification of histone modification (e.g. H3K27me3). The algorithm II was used subsequently to the algorithm I. In this case, algorithm I was conducted to quantify the nuclear integrated signal intensity of the EZH2-specific antibody for every nucleus. In algorithm II, as shown in figure 2.3, the nuclei were then discriminated based on the EZH2-specific signal intensity and a set threshold value.

----- Low intensity protein-----

Select nuclei with a protein-specific staining intensity below threshold.

16: Set Logging Row and Column(SUMMARY, RELATIVEROW and ABSOLUTE COLUMN, 0, 1)

17: Integrated Morphometry - Load State("Signal below threshold")

18: Integrated Morphometry - Measure([14: Arithmetic])

19: Integrated Morphometry - Log Data([Last Result], SUMMARY, CURRENTDATA, 27, 2)

20: Integrated Morphometry - Create Objects Mask()

21: Threshold Image("IMA Objects Mask", 1, 65535, Inclusive)

22: Overwrite "binary FITC" = Binarize("IMA Objects Mask"), high = current value, low = current value

Subtract the created binary mask for low protein from the images showing modification-specific stained nuclei.

23: New "Low protein" = "Cy5" AND [22: Binary Operations]

24: Threshold Image([23: Arithmetic], 1, 16383, Inclusive)

25: Set Logging Row and Column(SUMMARY, RELATIVEROW and ABSOLUTE COLUMN, 0, 1)

26: Close("IMA Objects Mask")

Quantify the integrated signal intensity of the modification-specific staining for every selected nuclei.

27: Set Logging Row and Column(SUMMARY, RELATIVEROW and RELATIVE COLUMN, -1, 3)

28: Integrated Morphometry - Load State("IntegratedIntensity")

29: Integrated Morphometry - Measure([23: Arithmetic])

30: Integrated Morphometry - Log Data([Last Result], SUMMARY, CURRENTDATA, 27, 2)

31: Close([22: Binary Operations])

32: Close([23: Arithmetic])

Figure 2.3: Algorithm II (subsequently to algorithm I): Scoring for cells with low enzyme expression, quantification of histone methylation mark and export to a spread sheet. Algorithm II was used subsequently to algorithm I, where first EZH2-specific antibody signal intensities were quantified. In algorithm II, the nuclei were filtered for low EZH2-specific antibody signal intensities and subsequently quantified for H3K27me3. The identical algorithm was used to quantify H3K27me3 within cells with high EZH2-specific antibody signal (staining intensity above the threshold).

Figure 2.3 displays the algorithm II, scoring for nuclei with downregulated EZH2 after siRNA knockdown. The same algorithm was used to score nuclei expressing EZH2 above the threshold. After discrimination based on the EZH2-specific signal intensity, the segmented nuclei were reduced to binary code (binary object mask), consisting of yes-(signal)- and no-(background)-information. In order to locate the histone H3 modification-specific antibody signal to be quantified, the generated binary mask is used as a template to be superimposed over the respective fluorescent signal of the image set (identical pixel-x/y-coordinates). The nuclear integrated signal intensity (total signal intensity of the nucleus) was quantified for every nucleus in every image set and the results were exported to a spread sheet for further statistical analysis.

2.1.7.3 Algorithm III: Cell cycle classification and methylation profile

When stated in the experiment, the algorithm III was used to classify cell cycle phases, followed by a quantification of histone modification. In the algorithm III, the standardized image-analysis module (“Cell Cycle”) was used to classify the different cell cycle phases (figure 2.4).

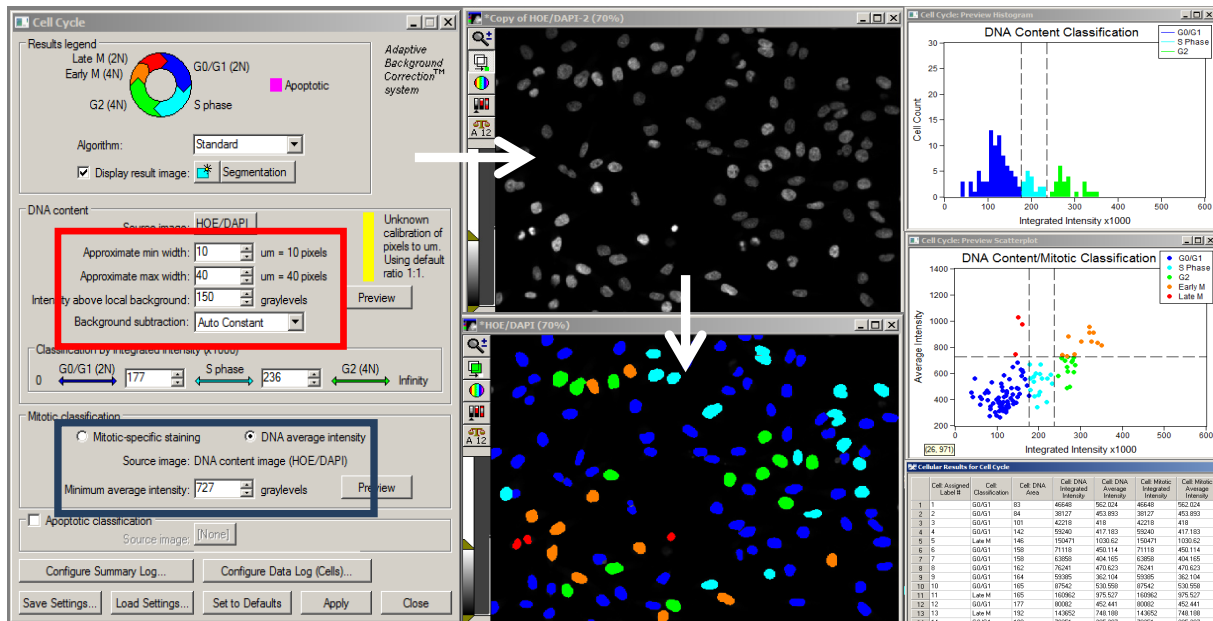


Figure 2.4: The standardized image-analysis module (“Cell Cycle”) provided by the image analysis software **MetaXpress®** Nuclei from the DNA channel (monochromatic) were segmented and classified into different cell cycle phases, based on Hoechst signal intensity and nuclear morphology.

A classification into different cell cycle phases was based on Hoechst signal intensity and nuclear morphology, using the integrated intensity (interphase nuclei, see figure 2.4 red rectangle) or the average intensity (M phase nuclei, see figure 2.4 blue rectangle) of the chromatin stain. Algorithm III started with loading the (“Cell Cycle”) module and defining variables to log the results for the different cell cycle stages, as shown in figure 2.5, part1. After nuclei segmentation and classification into different cell cycle phases, using the (“Cell Cycle”) module, the segmented nuclei were reduced to binary code (binary object mask), consisting of yes-(signal)- and no-(background)-information. For each cell cycle phase, one binary mask was created.

Log stage label

1: LV.StageLabel = "No Label"

2: Log Variable(LV.StageLabel, NEWLINE, NO HEADER)

Use the "Cell Cycle" module for nuclei segmentation and cell cycle phase classification.

3: Configure Cell Cycle Summary Log()

4: New "Segmentation" = Cell Cycle(DNA content = "HOE/DAPI", Mitotic = "HOE/DAPI", Apoptotic = [None])

↳ DNA content: Approximate min width = Current Value

↳ DNA content: Approximate max width = Current Value

↳ DNA content: Intensity above local background = Current Value

↳ DNA content: Background subtraction value = Current Value

↳ DNA content: G0/G1 to S phase cutoff = Current Value

↳ DNA content: S phase to G2 cutoff = Current Value

Log the results.

5: LV.G0G1Cells = CellCycle.G0G1Cells

6: LV.SCells = CellCycle.SPhaseCells

7: LV.G2MCells = CellCycle.G2MCells

8: LV.TotalCells = CellCycle.G0G1Cells+ CellCycle.G2MCells+ CellCycle.SPhaseCells

9: Log Variable(LV.G0G1Cells, NONEWLINE, NO HEADER)

10: Log Variable(LV.SCells, NONEWLINE, NO HEADER)

11: Log Variable(LV.G2MCells, NONEWLINE, NO HEADER)

Create a binary mask for every cycle stage.

12: New "G0G1_Binary" = Binarize([4: Cell Cycle]), 1, 1

13: New "S_Binary" = Binarize([4: Cell Cycle]), 2, 2

14: New "G2_Binary" = Binarize([4: Cell Cycle]), 3, 3

Erode binary masks to prevent background detection.

15: New "G0G1_Erode" = Morphological Erode([12: Binary Operations], Circle, Diameter=2)

16: New "S_Erode" = Morphological Erode([13: Binary Operations], Circle, Diameter=2)

17: New "G2_Erode" = Morphological Erode([14: Binary Operations], Circle, Diameter=2)

Subtract the created binary masks from the images of the modification-specific stained nuclei for each cell cycle stage.

18: New "G0G1_AND" = [15: Morphological Erode] AND "CY5"


19: New "S_AND" = [16: Morphological Erode] AND "CY5"


20: New "G2_AND" = [17: Morphological Erode] AND "CY5"


Figure 2.5: Algorithm III, part 1: Generating nuclei masks based on cell cycle phases and superimpose with images showing the histone modification-specific antibody signal.

Peripheral pixels were reduced to smooth signal edges and, in order to locate the histone H3 modification-specific antibody signal to be quantified, the generated binary mask is used as a template to be superimposed over the respective fluorescent signal of the image set (identical pixel-x/y-coordinates). In the following, the nuclear integrated signal intensity (total signal intensity of the nucleus) was quantified for every nucleus in every cell cycle phase and the results were exported to a spread sheet for further statistical analysis (figure 2.6, part2).


Quantify the integrated signal intensity of the modification-specific staining for G0/G1 cells.


 21: Auto Threshold for Light Objects(Legacy heuristic algorithm)

 22: Integrated Morphometry - Load State("IntegrIntensitySummary")


 23: Integrated Morphometry - Measure([18: Arithmetic])

Quantify the integrated signal intensity of the modification-specific staining for S cells.


 24: Auto Threshold for Light Objects(Legacy heuristic algorithm)


 25: Integrated Morphometry - Load State("IntegrIntensitySummary")


 26: Integrated Morphometry - Measure([19: Arithmetic])


 27: Integrated Morphometry - Log Data([19: Arithmetic], SUMMARY, CURRENTDATA, 27, 2)

Quantify the integrated signal intensity of the modification-specific staining for G2 cells.

 28: Auto Threshold for Light Objects(Legacy heuristic algorithm)


 29: Integrated Morphometry - Load State("IntegrIntensitySummary")


 30: Integrated Morphometry - Measure([20: Arithmetic])


 31: Integrated Morphometry - Log Data([20: Arithmetic], SUMMARY, CURRENTDATA, 27, 2)


Close all open images


 32: Close([4: Cell Cycle])


 33: Close([12: Binary Operations])


 34: Close([13: Binary Operations])


 35: Close([14: Binary Operations])


 36: Close([15: Morphological Erode])

 37: Close([16: Morphological Erode])

 38: Close([17: Morphological Erode])

 39: Close([18: Arithmetic])

 40: Close([19: Arithmetic])

 41: Close([20: Arithmetic])


 End of Journal

Figure 2.6: Algorithm III, part 2: Quantify the integrated signal intensities of every nucleus in distinctive cell cycle stage and export to a spread sheet.

2.2 Molecular biological methods

2.2.1 RNA isolation, concentration and quality determination

To isolate RNA from cells treated with inhibitors or siRNA, the cells were washed twice with DPBS and, for the cell lysis, incubated in cooled RNeasy Lysis Buffer (Qiagen) for 10 min gently shaking at RT. The buffer was used in a volume of 20 μ l/well and six wells per treatment condition were incubated and subsequently pooled. Centrifugation using a QIAshredder column (Qiagen) for every pooled lysate sample was applied to ensure complete homogenization of the cell lysates. The eluted lysates were transferred to a 2 ml reaction tube and the volume of the lysate was then increased up to 600 μ l with cooled RNeasy Lysis Buffer to enable the automated RNA isolation using the RNeasy Mini Kit (Qiagen) and the QIAcube (Qiagen), following the manufacturer's instructions. The RNA isolation included a DNase digestion step. The total RNA was eluted using RNase-free water

and the concentration and quality was determined at 260 nm using the Nanodrop 2000/2000c UV/VIS Spectrometer with a sample volume of 1.5 µl. To measure a possible DNA or protein contamination of the sample, the ratio 260nm/280nm was noted. A ratio of 260nm/280nm = 1.8-2.2 was considered as sufficient purity for further experimental steps.

2.2.2 Reverse Transcription (cDNA-Synthesis)

For the synthesis of cDNA (complementary DNA) from the isolated RNA, the High Capacity RNA-to-cDNA Master Mix (Applied Biosystems) was used. Following the manufacturer's instructions, 250-300 ng RNA per preparation of 20 µl were transcribed. The sample preparation is summarized in table 2.3. The reverse transcription was conducted using a 96-well plate (Micro Amp Optical well 96, Applied Biosystems). The samples were incubated for 5 min at 25°C, followed by 30 min at 42°C, 5 min at 85°C and cooled down in the end to 4°C, using a Thermocycler Mastercycler Personal (Eppendorf). If not directly used for further experiments, the cDNA samples were stored at -20°C.

Table 2.3: cDNA synthesis preparation:

Component	Reaction volume
Master Mix	4.0 µl
RNA template	up to 16 µl
Nuclease-free H ₂ O	ad to 20 µl
Total	20 µl

2.2.3 Semi-quantitative Real-Time PCR (qRT-PCR)

The obtained cDNA was amplified in 384-well MicroAmpTM reaction plates, using a TaqMan[®] Fast Advanced Master Mix and a 7900HT Fast Real-Time PCR System (Applied Biosystems), used to the manufacturer's recommendation for gene expression quantification. The used TaqMan[®]-assays are listed in table 6.2.3. The sample preparation is summarized in table 2.4. The prepared assay plate was sealed with an adhesive film and centrifuged at 10000 rpm prior to the measurement reaction. The determination of a relative gene expression was based on the $\Delta\Delta$ CT-method.

Table 2.4: qRT-PCR sample preparation:

Component	Reaction volume
TaqMan [®] Fast Advanced Master Mix	5.0 µl
TaqMan [®] -assay	0.5 µl
Nuclease-free H ₂ O	3.5 µl
Total	9.0 µl

2.3 Biochemical methods

2.3.1 BCA protein assay

To determine protein concentrations from the cell lysates after treatment with chemical inhibitors or siRNA nucleotides, the BCA-(Bicinchoninic acid) protein assay (ThermoScientific) was used. To generate a calibration curve, 2 mg/ml BSA (provided with the kit) were diluted in distilled H₂O to a concentration series ranging from 400-25 µg/ml in duplicates with a volume of 50 µl, transferred into a 96-well plate. 2.5 µl of each protein sample were diluted in 50 µl distilled H₂O and transferred into the 96-well plate. Distilled H₂O was used as blank value. Cell lysis buffer was added to each well of the calibration curve and to the blank value at a volume of 2.5 µl to make them more equal to the sample measurements. To initiate the calorimetric measurement, 200 µl/well BCA were added to the wells of the BSA calibration curve, the blank value and all sample wells. The assay plate was incubated for 30 min at 37°C followed by the measurement of the change in blue color to violet at 562 nm using the UV/VIS-spectrometer (Perkin Elmer). Protein concentrations were determined based on the BSA calibration curve.

2.3.2 SDS-Polyacrylamide-gel-electrophoresis

To detect protein levels from cell lysates using western blot analysis, a denaturing SDS-Polyacrylamide-gel-electrophoresis (SDS-Page) was conducted. For the sample buffer preparation, NuPAGE[®] LDS sample buffer (4X) was mixed with NuPAGE[®] Reducing Agent (10X) (Life Technologies). 100 µg protein were mixed with 35 µl prepared sample buffer and the volume was completed to 100 µl using H₂O. Protein denaturation was ensured by heating the

samples to 70°C for 10 min. After cooling the samples at 4°C, 20 µl of each sample were pipetted into the gel pockets, using a NuPAGE® Novex® 4-12% Bis-Tris [Bis (2-hydroxyethyl) imino-tris (hydroxymethyl) methane-HCl] protein gel (1.0 mm, 12 gel pockets) and a Bolt™ Mini Gel Tank (Life Technologies) as gel chamber together with optionally MES or MOPS running buffer. In addition to the samples, 10 µl protein marker were loaded into one pocket, applying Odyssey 10-250 kDa (LI-COR Biosciences) or Precision Plus Protein Standards (BIO-RAD) and the electrophoresis was conducted at 165 V for 35-45 min.

2.3.3 Cell lines and maintenance

The western blot analysis was conducted for the qualitative and semi-quantitative detection of protein levels after siRNA transfection using either nitrocellulose or PVDF (polyvinylidene difluoride) membranes. After SDS-Polyacrylamide-gel-electrophoresis, the gel was quickly drowned with H₂O and then transferred to the iBlot® Dry Blotting System together with an anode stack, a filter paper pre-soaked in H₂O and the cathode stack (ready to use, Invitrogen). The blotting was started, referring to the manual instructions with duration of 7 min. A Ponceau-S-stain (Sigma) was used to control a successful transfer of the proteins. The membrane was washed in TBS 0.1 % and incubated in Ponceau-S solution for 5 min. The membrane with the visible bands was now optionally cut to process different protein bands with different antibodies, and then washed three times with TBS 0.1 % for 5 min. The membrane was blocked in either Blocking Reagent (Roche) or in 5 % milk powder /TBS 0.1 % for 1 hour at RT, gently shaking.

2.3.4 Immune detection

Incubation with primary antibodies (listed in table 6.2.4) was conducted optionally in either Blocking Reagent (Roche) or in 5 % milk powder /TBS 0.1 % over night at 4°C. The membranes were washed three times with TBS 0.1 % for 10 min at RT, followed by incubation with the fluorescently labeled secondary antibodies (anti-rabbit- or anti-mouse-AlexaFluor680, Invitrogen) for 1 hour at RT in the dark. The membranes were then washed three times with TBS 0.1 % for 10 min at RT, and protein bands were detected using the Odyssey Infrared Imager (Li-Cor Biosciences) and optionally quantified in relation to GAPDH (Li-Cor Image Software).

2.3.5 Data analysis

Average results were fitted using a 4-parameter equation and the IC_{50} was determined using GraphPad Prism (Version 5.04 for Windows, San Diego California USA). Results per nuclei were processed into relative frequency distributions using GraphPad Prism. For the comparison of more than two mean values, the One-way-ANOVA was used. For a multiple comparison test, the Tukey test was applied, when comparing every mean to every other mean. The Dunnett test was applied when comparing every mean to a control mean.

3. Results

3.1 Development and validation of a histone methylation HCA assay

In order to provide a cellular mechanistic and HTS-compatible assay, which allows for cellular profiling of compounds that modulate protein methyltransferases (HMTs), I established an HCA approach. Therefore, I evaluated and validated the phenotypic assay in different cancer cell lines by histone methylation inhibition using siRNA (chapter 3.1.1) and small-molecule inhibitors (chapter 3.1.2). Throughout this work I used the human cancer cell lines HeLa S3, PC3, MDA-MB-231 and MCF7 for the different experiments. The cervix cancer cell line HeLa S3 was used for all preliminary experiments including the targeting of different HKMTs by the use of siRNA-mediated knockdown in 3.1.1. HeLa S3 cells are suitable for siRNA transfections and routinely used in HCA approaches. However, EZH2 is found overexpressed in a broad spectrum of cancers including myeloma, lymphoma, breast and prostate cancers [6, 7, 94, 120, 166]. Therefore, I expanded our cellular model systems towards the two human breast cancer cell lines MDA-MB-231 and MCF7 and the human prostate cancer cell line PC3, overexpressing EZH2 as well [6]. I analyzed individual cells using immunofluorescence detection of EZH2 and specific histone modifications in combination with Hoechst-stained chromatin. The cells were imaged using an automated confocal imaging platform, followed by an image analysis using a developed MetaXpress®-based routine.

3.1.1 Phenotypic evaluation of siRNA-mediated HKMT knockdown

For validation of the assay concept, I started this work by targeting different HKMTs using siRNA-mediated knockdown. The aim was to quantify a possible induced modulation of the respective histone methylation marks. Moreover, I intended to identify an appropriate histone modifying enzyme to target for the HCA assay development and the following research conducted in this work. To this end, I treated HeLa S3 cells with at least two siRNAs, targeting different regions of the transcript of every selected HKMT. I chose a set of six HKMTs based on their association with human cancers, as summarized in table 2.1 in chapter 1. Therefore, I silenced the enzymes EZH2, DOT1L, MLL2, MLL, SMYD2 and NSD1, respectively, allowing us to evaluate the different degrees in possible histone modification modulation.

To this end, I quantified different relative methylation levels of histone H3 at three days after siRNA-mediated HKMT knockdown. Figure 3.1 shows a schematic image analysis for a single cell quantification of the level of EZH2 and the respective trimethylation of lysine 27 of histone H3 (H3K27me3), after siRNA-mediated EZH2 knockdown. Briefly, by using the DNA stain, I was able to segment individual nuclei, followed by a determination of size and shape. The resultant images were used to generate binary object masks, to be subsequently superimposed over the EZH2- and H3K27me3-specific staining of the image set. In the following, the integrated signal intensity level was measured for each nucleus. A simultaneous antibody staining of EZH2 and H3K27me3 enabled the direct correlation of the level of EZH2 and H3K27me3 for every single nucleus.

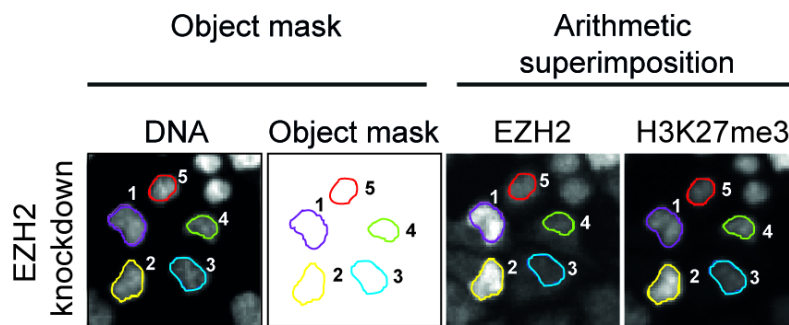


Figure 3.1: Schematic image analysis for phenotypically quantifying cellular EZH2 and H3K27me3 using HCA. Cells to be analyzed were immunostained, following image acquisition. Using the DNA stain, individual nuclei were segmented (DNA, nuclei 1-5), and binary object masks were generated. They were subsequently superimposed over the EZH2- and H3K27me3-specific staining of the image set, in order to accurately identify every nucleus to be measured. Fields appearing in the figure are smaller than a complete field of view.

The phenotypic quantification of the different, relative methylation levels of histone H3 after knockdown of each of the six HKMTs is shown in figure 3.2. Using the HCA approach, I quantified a reduction in lysine 79 of histone H3 (H3K79me2) after a knockdown of DOT1L, H3K27me3 after a knockdown of EZH2, a trimethylation of lysine 4 of histone H3 (H3K4me3) after a knockdown of MLL, MLL2 and SMYD2 and finally a dimethylation of lysine 36 of histone H3 (H3K36me2) after a knockdown of NSD1.

Clearly, the strongest and significant histone modification modulation was achieved with a knockdown of EZH2. The EZH2-specific histone H3 methylation mark H3K27me3 was reduced about 84% at a maximum, using two distinctive siRNAs. Less profound effects were observed

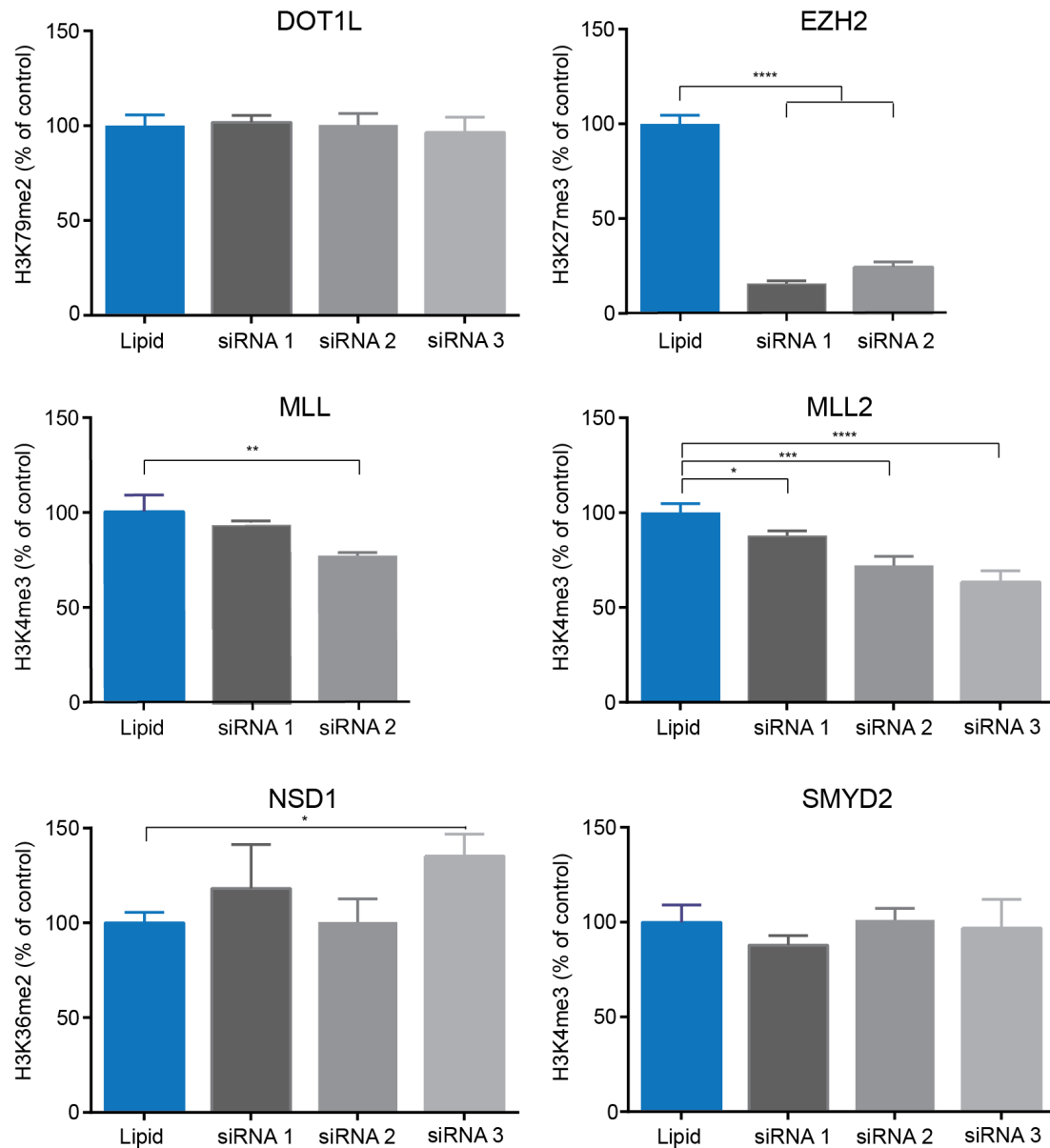


Figure 3.2: Phenotypic quantification revealed different effects on global levels of respective histone methylation marks after siRNA-mediated knockdown of six selected HKMTs. HeLa S3 cells were treated with siRNA targeting the different HKMTs. The graphs show the relative histone H3 methylation level at three days after siRNA-mediated HKMT knockdown. Responses are plotted as percentage of the lipid control. Mean values represent the average of approximately 1500 nuclei analyzed. Error bars show the standard deviation from three replicates. * $P \leq 0.05$; ** $P \leq 0.01$; *** $P \leq 0.001$; **** $P < 0.0001$.

for knockdowns of MLL2 and MLL. A knockdown of MLL2 reduced H3K4me3 significantly about 12% to 37%, induced by all three siRNAs. A knockdown of MLL reduced H3K4me3 significantly about 23% but induced only by one of the two siRNAs tested. On the contrary, for the three HKMTs DOT1L, NSD1 and SMYD2, I was not able to measure a modulation of H3K79me2, H3K36me2 or H3K4me3, respectively, at three days after knockdown. However, an increase in H3K36me2 of 35%, induced by one of three siRNAs targeting NSD1, was observed.

In order to confirm the efficiency of the conducted knockdown experiments, I determined the level of mRNA for the targeted HKMTs in a time course over four days, using real-time quantitative PCR (results are shown in figure 3.3). For all six enzymes, a significantly reduced mRNA level was observed to at least 40% at day two and three after knockdown.

Based on the described data, I picked the HKMT EZH2 as the target enzyme of choice for further HCA assay development and a subsequent investigation of the functionality of induced H3K27me3 suppression. Therefore, I analyzed a siRNA-mediated knockdown of EZH2 followed by a modulation of H3K27me3 in a time course experiment (as shown in figure 3.4 and 3.5). With both siRNAs, targeting distinct regions of the EZH2 transcript, I was able to induce a time-dependent decrease in the nuclear EZH2 level followed by a reduction in global H3K27me3. This becomes evident in the representative confocal immunofluorescence images of EZH2 protein and H3K27me3 at the original levels, day one- and day four after the knockdown, shown in figure 3.4. A quantification of nuclear EZH2 (green) and global H3K27me3 (red), displayed in figure 3.5, showed a concomitant decrease for both, the HKMT and the histone modification, to approximately 25% at a maximum at four days after the siRNA-mediated EZH2 knockdown. Figure 3.4 and 3.5 are displaying results observed after a knockdown of EZH2 using siRNA 1 (referring to the labeling in figure 3.2 and 3.3). Similar data was observed using both alternative siRNAs.

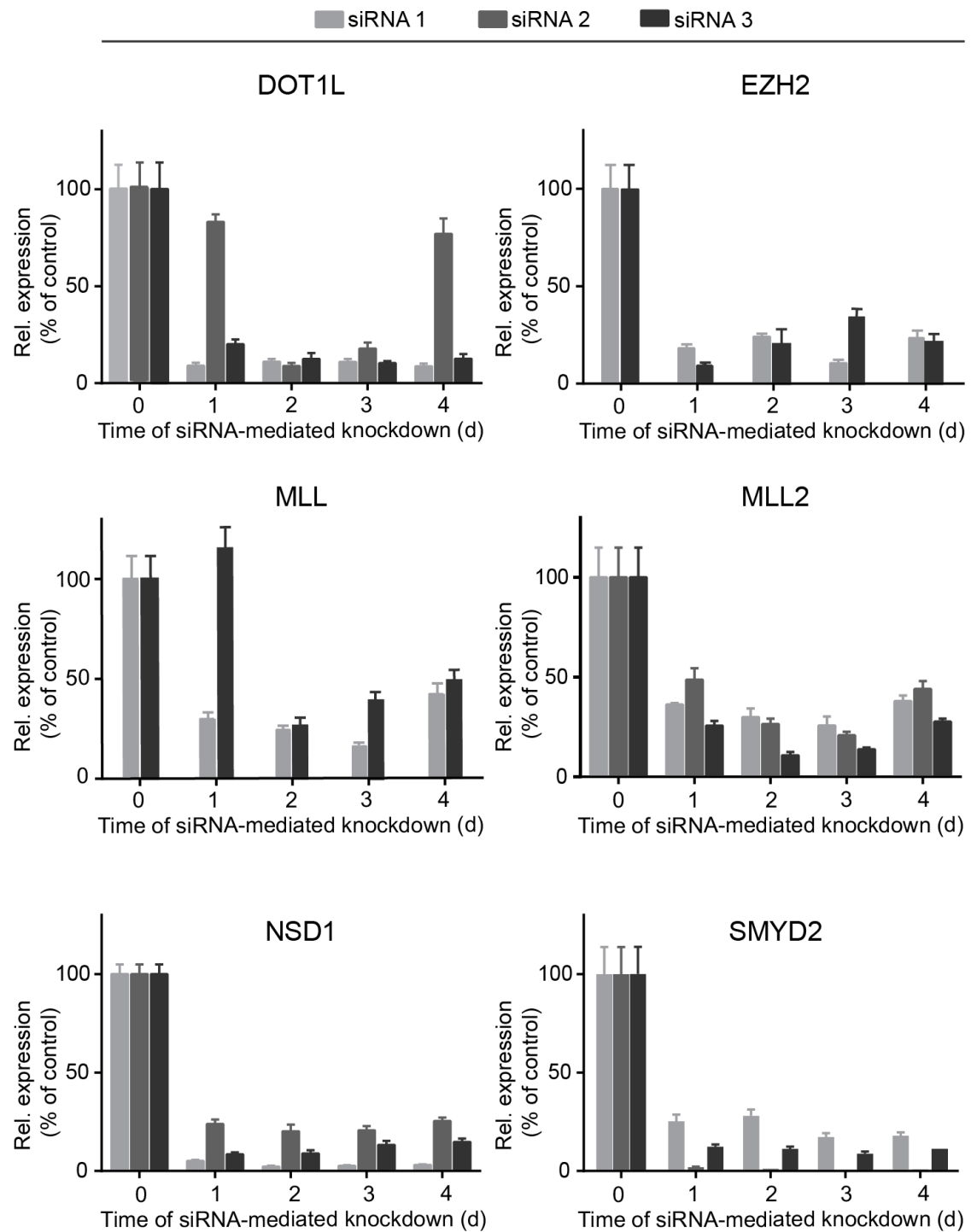


Figure 3.3: Reduced mRNA levels were observed for the six HKMTs, targeted in a time course using siRNA. The graphs show the mRNA levels of targeted HKMTs after siRNA-mediated knockdown using HeLa S3 cells in a time course, quantified using qRT-PCR analysis. The data displays the expression of DOT1L, EZH2, MLL, MLL2, NSD1 and SMYD2, relative to the reference gene 18S and normalized to the lipid control. Knockdown efficiencies were confirmed by reduced mRNA levels of all six enzymes at up to four days after siRNA treatment. Plotted values represent the mean and standard deviation from three replicates.

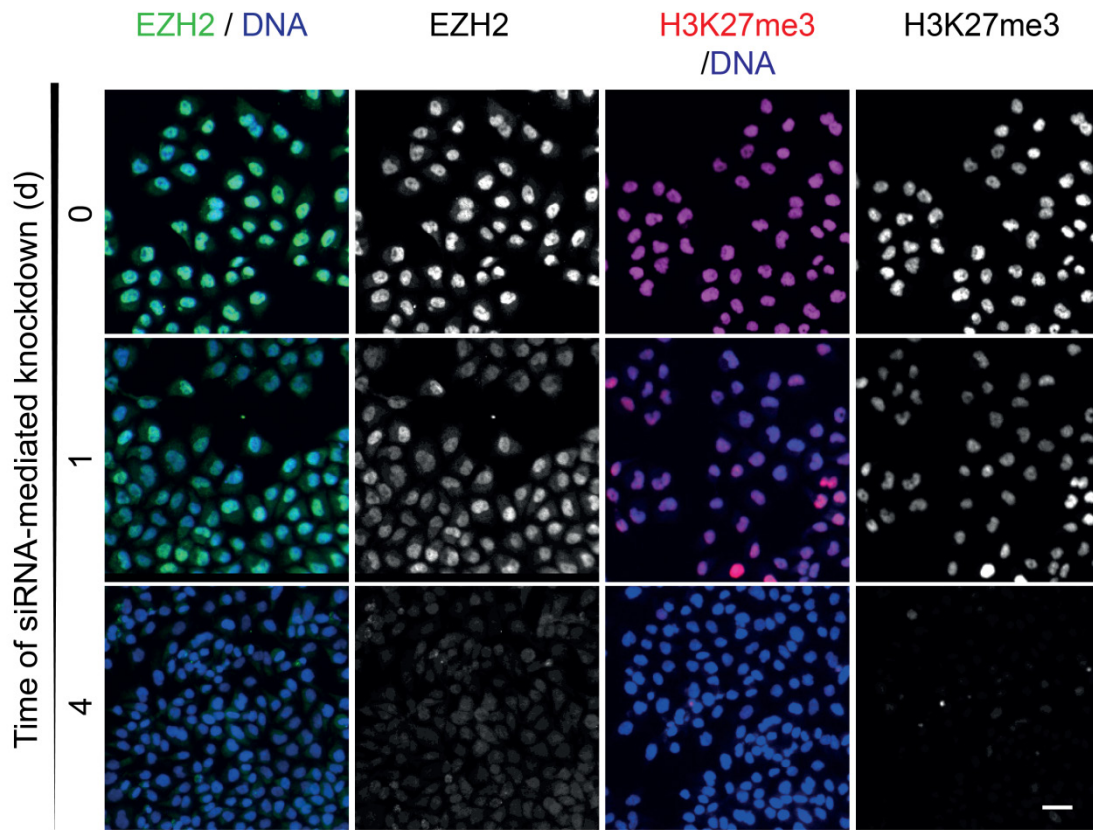


Figure 3.4: Representative confocal immunofluorescence images showing an increasing suppression of global H3K27me3 with time, induced by a knockdown of EZH2 using siRNA. HeLa S3 cells were treated with siRNA targeting EZH2. Representative confocal immunofluorescence images show the EZH2 protein and H3K27me3 at indicated days after knockdown. The first panel on the left hand side displays EZH2 (green) merged with a staining of the nuclei (blue) at the indicated days after the knockdown. The second panel displays EZH2 alone (monochrome), the third panel displays H3K27me3 (red) merged with a staining of the nuclei (blue), and the forth panel displays H3K27me3 alone (monochrome) at indicated days after siRNA knockdown. Scale bar = 10 μ M. Images display HeLa S3 cells treated with siRNA 1 (referring to the labeling in figure 3.2 and 3.3). Similar results were observed using siRNA 2.

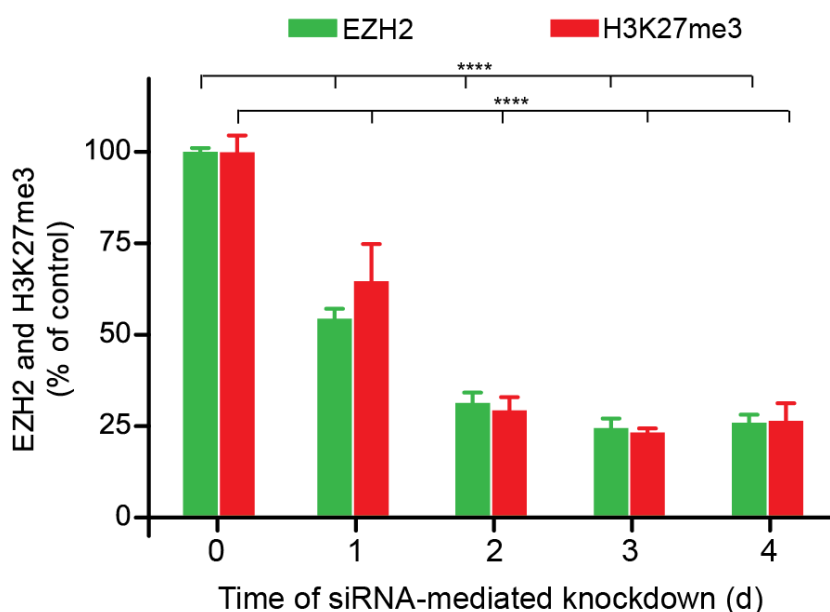


Figure 3.5: A quantification of EZH2 and global H3K27me3 shows that the methylation mark was directly suppressed in a time -dependent manner, induced by siRNA-mediated knockdown of EZH2. HeLa S3 cells were treated with siRNA targeting EZH2. The graph shows a quantification of the immunofluorescence images displayed in figure 3.4, displaying the relative nuclear EZH2 protein together with the global level of H3K27me3 quantified as time course after siRNA-mediated EZH2 knockdown. Responses are plotted as percentage of the lipid control. Mean values represent the average of approximately 1500 nuclei analyzed. Error bars show the standard deviation from three replicates. The data was generated treating HeLa S3 cells with siRNA 1 (referring to the labeling in figure 3.2 and 3.3). Similar results were observed using siRNA 2. **** P<0.0001.

3.1.2 Analysis of chromatin modulation induced by small-molecule inhibitors

I proved the assay concept by evaluating different degrees in possible histone modification modulation conducting a knockdown analysis of different HKMTs using siRNA. Aiming to provide a cellular mechanistic and HTS-compatible assay, which allows for cellular profiling of compounds modulating HKMTs, I proceeded with an analysis of chromatin modulation induced by small-molecule inhibitors.

Although I already picked the HKMT EZH2 as the target enzyme of choice for further HCA assay development, I first expanded the set of previously analyzed HKMTs by G9a and its interaction partner GLP 1 (figure 3.6). As I had two specific inhibitors available by the time of

the siRNA-knockdown experiments, I preferred the analysis of G9a and GLP 1 by small-molecule inhibition and spared them for the knockdown analysis using siRNA in chapter 3.1.1.

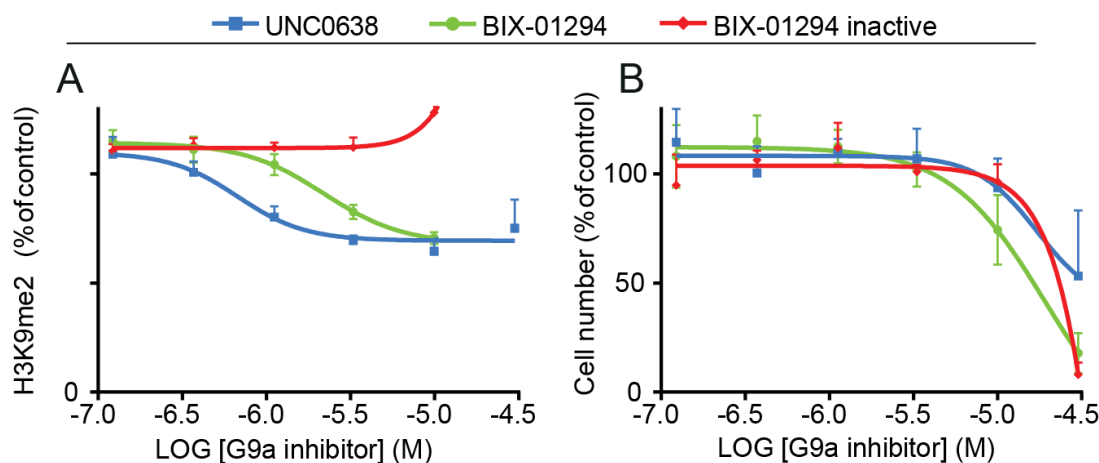


Figure 3.6: The G9a and GLP 1 inhibitors UNC0638 and BIX-01294 demonstrated distinguished cellular inhibitory activity on H3K9me2. HeLa S3 cells were treated with varying concentrations of BIX01294, UNC0638 (blue and green), plus one inactive BIX01294 derivate (red, used as a negative control) over three days. The graphs show the concentration response after inhibitor treatment as measured by the relative H3K9me2 levels and the relative numbers of analyzed nuclei. Evaluation of the cellular inhibitory activity of the two inhibitors on day three generated IC_{50} values of 1.8 μ M and 2.5 μ M for UNC0638 and BIX-01294, respectively. Responses are plotted as percentage of the DMSO control. Mean values represent the average of approximately 1500 nuclei analyzed. Error bars show the standard deviation from three replicates.

Using the HCA assay, I evaluated the cellular inhibitory activity of the small-molecule inhibitors BIX01294 [167] and UNC0638 [8], targeting G9a and GLP 1. BIX01294 and UNC0638 are described to inhibit G9a with biochemical IC_{50} values of 180 nM and <15 nM and GLP 1 with enzymatic potencies of 34 nM and 19 nM, respectively [8]. The chemical structures are displayed in figure 6.4. I treated HeLa S3 cells over three days with varying concentrations of BIX01294, UNC0638 and a BIX01294 derivate, inactive towards H3K9me2 suppression, which I used for a negative control. Among the analyzed inhibitors, both UNC0638 and BIX01294 induced a dose-dependent H3K9me2 suppression down to 65%, shown in figure 3.6 A. Evaluation of the cellular inhibitory activity of the two inhibitors on day three generated average IC_{50} values of 1.81 μ M and 2.50 μ M for UNC0638 and BIX01294, respectively. A distinct course of functional (H3K9me2 suppression) and proliferative effects after G9a and GLP 1 inhibition over three days was demonstrated (as shown in figure 3.6 B). At the highest inhibitor concentration of 10 μ M, a reduction in the cell number about 50%

was induced by the inhibitor UNC0638 and about almost 100% with BIX01294 and its derivate. The inactivated BIX01294 derivate caused no reduction of H3K9me2 at inhibitor concentrations up to 3 μ M, as shown in figure 3.6 A. Moreover, at 10 μ M inhibitor concentration, I quantified an increase in the signal intensity for H3K9me2. Overall, using the HCA assay, I accurately quantified a modulation of global H3K9me2 over a broad inhibitor concentration range, validating the functionality of the assay.

However, based on the data obtained from targeting different HKMTs by knockdown analysis and the inhibition of G9a and GLP 1, the HKMT EZH2 remained the target enzyme of choice for further HCA assay development and subsequent investigation of the mechanism of induced H3K27me3 suppression, described in chapter 3.2. Recent discoveries of inhibitors targeting EZH2 [92, 93, 168-175] enabled us to use a selective and cell-active indazole EZH2 inhibitor as a tool inhibitor for assay development. The solvent for the used small-molecule inhibitors in this study was DMSO.

For the assay development, it was important to determine the amount of DMSO which can be applied during the assay without compromising the readout (the level of global histone H3 modification). Therefore, I quantified global H3K27me3 while increasing the portions of DMSO under assay conditions within HeLa S3 cells, using a 384-well-plate format. The cells were treated with increasing concentrations of DMSO for three days. Figure 3.7 shows the global level of H3K27me3 together with the number of analyzed nuclei, at indicated DMSO portions normalized to non-treated cells. No dose-dependent H3K27me3 suppression was induced by DMSO at percentages up to 0.5%. However, applying concentrations of DMSO higher than 0.5% caused an impact on the level of H3K27me3 and proliferation. I observed a reduction of H3K27me3 about 20% caused by a treatment with 1.5% DMSO. In parallel, proliferative effects were observed causing a reduction in the cell number of 25%. Nevertheless, the portion of DMSO applied in the assay was kept equal throughout the entire assay plate and did not exceed 0.3% at any time for the cell line HeLa S3. Moreover, analyzing the cell lines MCF7 or MDA-MB-231, working portions of DMSO ranged between 0.03% - 0.1%. Thus, under these assay conditions DMSO was not expected to compromise the assays readout.

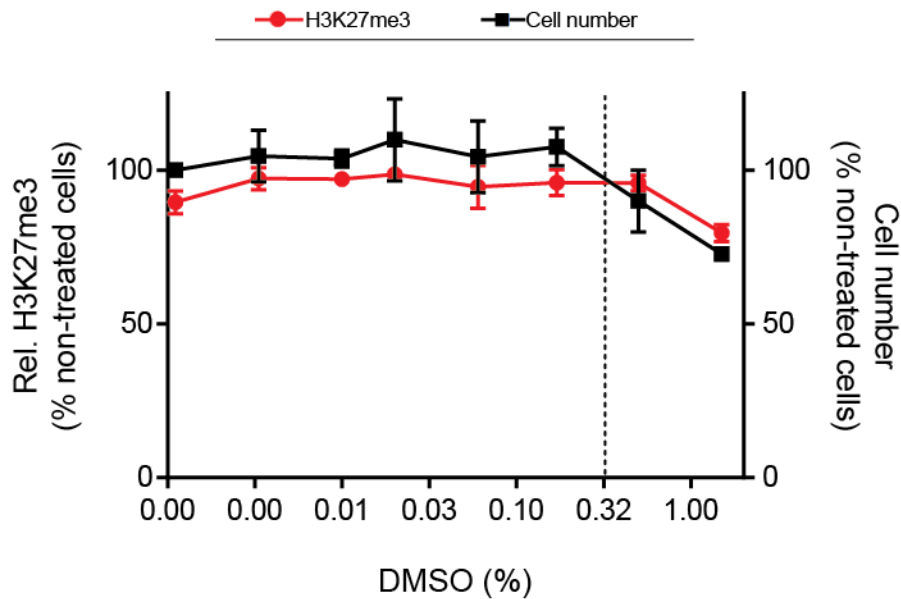


Figure 3.7: No dose-dependent H3K27me3 suppression or cell number reduction was observed with DMSO concentrations up to 0.5% under assay conditions, using a 384-well plate format. HeLa S3 cells were treated with increasing portions of DMSO over three days. The graph shows the concentration response of the increasing portions of DMSO in the relative H3K27me3 level and in the relative number of analyzed nuclei. Responses are plotted as percent signal relative to the original H3K27me3 level in non-treated cells, or as percent cell population relative to the original cell population of non-treated cells. Mean values represent the average of approximately 1500 nuclei analyzed. Error bars show the standard deviation from three replicates.

I used the EZH2 tool inhibitor mentioned above for the development of the HCA assay. For the tool inhibitor, an enzymatic inhibitory potency of about 4 nM is reported [173, 175]. The chemical structure is displayed in figure 6.5. Applying the inhibitor over three days at several concentrations, I observed in HeLa S3 and also in the cell lines MCF7 and MDA-MB-231, a profound maximal reduction of H3K27me3 to 9%, 13% and 6% of their original levels, as shown in figure 3.8 A,B and C. For a normalization of the assay readout (cellular inhibitory activities of H3K27me3), the cells were treated only with DMSO and immunostained for H3K27me3, representing a negative control (100% global level of H3K27me3). For determination of the base level of zero global H3K27me3 (0% global level of H3K27me3), DMSO treated cells were not immunostained as usual. Instead, the cells were incubated only with the fluorescently conjugated secondary antibody, without prior incubation with the H3K27me3-specific primary antibody. The signal from the secondary antibody was quantified

to represent the minimal possible signal (background signal), representing zero global H3K27me3. Thus, a profound H3K27me3 suppression, induced by an inhibition of EZH2, can be quantified, remaining 6% of the overall measurable global H3K27me3.

An evaluation of the inhibitors cellular inhibitory activity on day three generated IC₅₀ values of 5 μ M, 442 nM and 133 nM for HeLa S3-, MCF7- and MDA-MB-231 cells, respectively. The decreasing order indicated different degrees of sensitivity towards EZH2 inhibition with respect to a reduction in H3K27me3. Notably, a distinct separation of functional (H3K27me3 suppression) and proliferative effects after an inhibition of EZH2 over three days was demonstrated. Selective small-molecule EZH2 inhibition induced a reduction in the cell number only with the highest inhibitor concentration of 30 μ M and 10 μ M for the cell lines HeLa S3 and MDA-MB-231, respectively. A profound H3K27me3 suppression in MCF-7 cells, as shown in figure 3.8 B, occurred with no cytotoxic effect even at the highest inhibitor concentration (10 μ M).

I expanded the current assay set up towards a broad panel of other methylation marks, further testing the assays adaptability. Therefore, I probed the cell lines HeLa S3, MCF7 and MDA-MB-231 simultaneously on a set of other histone H3 methylation marks after an inhibition of EZH2 for three days, using both the EZH2 tool inhibitor and the nucleoside-analogue 3-deazaneplanocin A DZNep. DZNep modulates chromatin through indirect inhibition of HKMTs. It hinders S-adenosyl-methionine dependent reactions by inhibiting S-adenosyl-L-homocysteine (SAH) hydrolase [176, 177]. It has recently been used to probe the cellular function of EZH2 and H3K27me3 before the discovery of potent and selective small-molecule EZH2 inhibitors.

While preventing H3K27me3, the inhibition of EZH2 with the tool inhibitor did not alter global levels of H3K9me2, H3K4me3, H3K36me2, H3K79me2 or total histone H3 in all three cell lines, as shown in figure 3.9 A-C. In contrast, DZNep induced a simultaneous dose-dependent reduction in H3K27me3 and H3K4me3 to approximately 50% (figure 3.9 D-F).

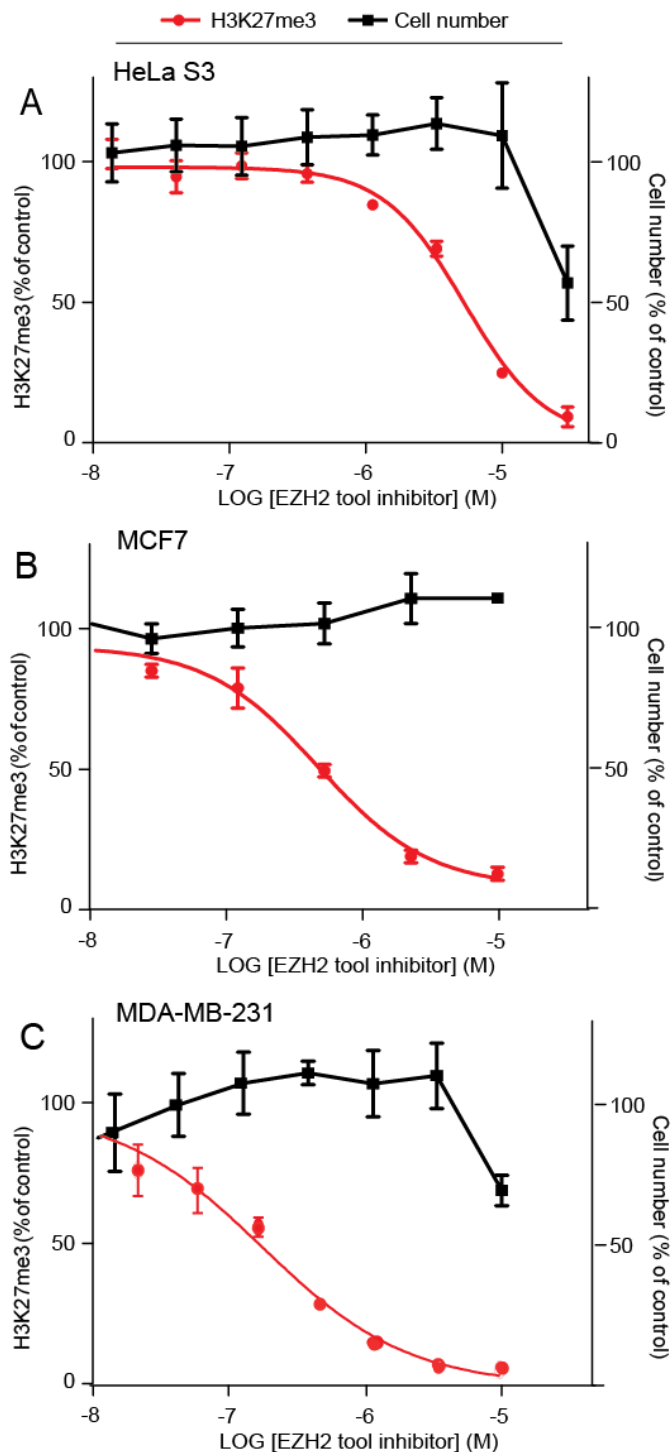


Figure 3.8: EZH2 inhibition using the selective tool inhibitor induced a profound demethylation of H3K27-me3, distinctively separated from cytotoxicity in the cell lines HeLa S3, MDA-MB-231 and MCF7. (A) HeLa S3-, (B) MCF7- and (C) MDA-MB-231 cells were treated with the EZH2 tool inhibitor for three days at several inhibitor concentrations. The graphs show the relative H3K27me3 level and the relative number of analyzed nuclei at the inhibitor concentrations indicated. Evaluation of the cellular inhibitory activity of the EZH2 tool inhibitor on day three generated IC₅₀ values of 5 μ M, 442 nM and 133 nM for HeLa S3-, MCF7- and MDA-MB-231 cells, respectively. Responses are plotted as percentage of the DMSO control. Mean values represent the average of 2000 nuclei analyzed. Error bars show the standard deviation from three replicates.

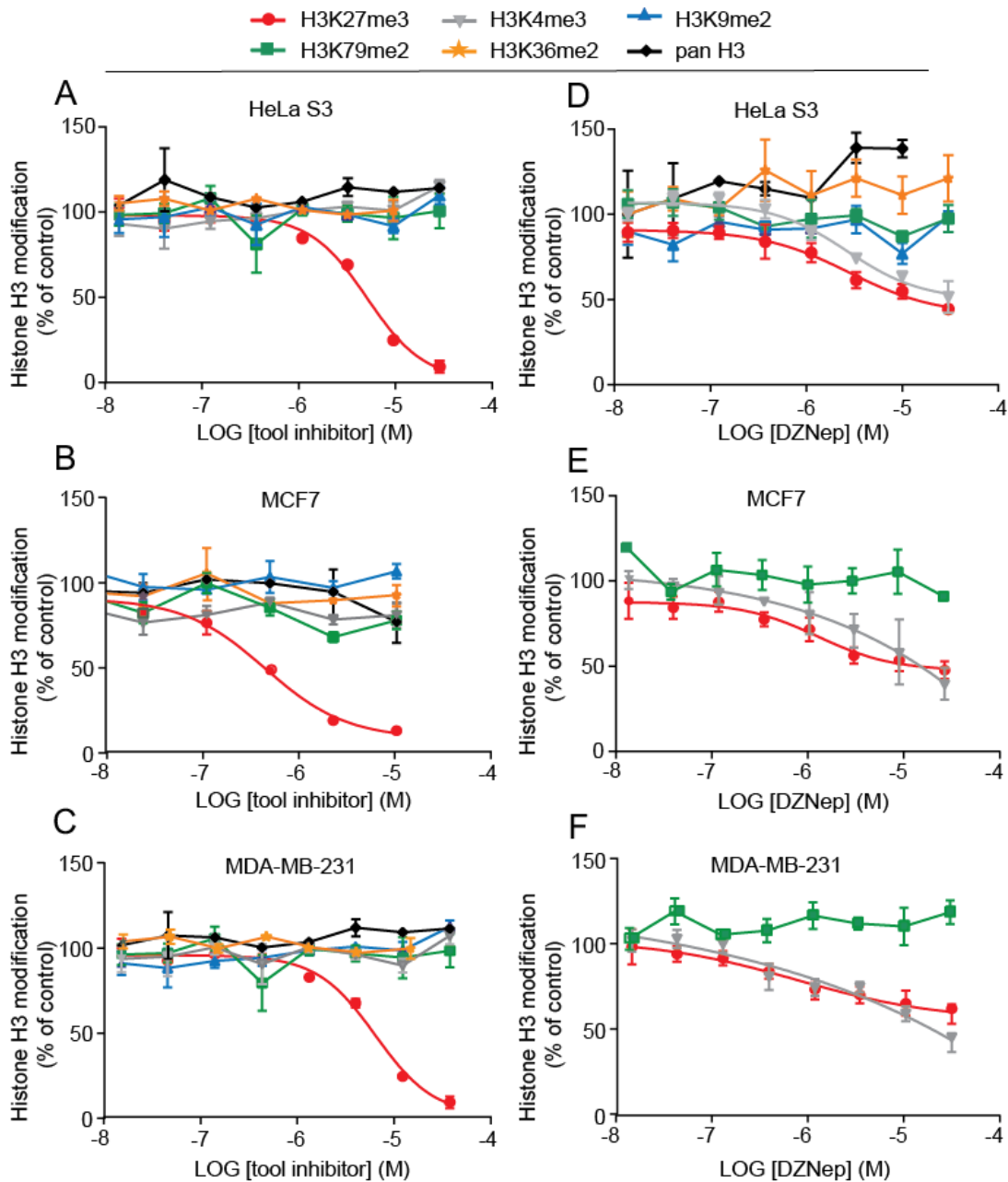


Figure 3.9: Selective EZH2 inhibition using the tool inhibitor did not alter several histone methylation marks except H3K27me3 while the non-selective inhibitor DZNep induced a dose-dependent reduction in H3K27me3 and H3K4me3. (A and D) HeLa S3-, (B and E) MCF7- and (C and F) MDA-MB-231 cells were treated with (A-C) the EZH2 tool inhibitor or (D-F) DZNep for three days at several inhibitor concentrations. The graphs show the relative histone H3 modification levels at inhibitor concentrations indicated. Evaluation of the cellular inhibitory activity of the tool inhibitor on day three generated an IC_{50} value of 133 nM. In contrast, non-selective inhibition by DZNep induced a less potent dose-dependent reduction in global H3K27me3 and H3K4me3 in parallel. Responses are plotted as percentage of the DMSO control. Mean values represent the average of 2000 nuclei analyzed. Error bars show the standard deviation from 3 replicates.

Notably, global levels in the tested histone H3 modifications other than H3K27me3 and H3K4me3 demonstrated more variability after a treatment with the non-selective inhibitor DZNep compared to the tool inhibitor, as shown for HeLa S3 cells in figure 3.9 D. For H3K36me2 and total histone H3, I quantified an increase about 20% and 30%, respectively. Altogether, I assessed quantitatively and mechanistically distinct effects on histone modifications induced by the tool inhibitor and DZNep.

In order to evaluate the quality of the assay, to determine its qualification enabling a cellular mechanistic and HTS-capable assay, I determined the Z'-factor in a 384-well-plate format for modulating H3K27me3 by EZH2 inhibition using the selective tool inhibitor, as shown in figure 3.10. The Z'-factor is a dimensionless parameter for use in comparison and evaluating the quality of HTS assays [18]. To this end, I treated MDA-MB-231 cells with DMSO or with the tool inhibitor at 3 μ M up to three days. For MDA-MB-231 cells, a concentration of 3 μ M induced the maximum effect on H3K27me3 but no effect on proliferation, as shown primarily in figure 3.6 C. Thus, for a Z'-factor determination during the assay development, the cells were treated with DMSO followed by a detection of H3K27me3, representing a maximal global level of H3K27me3. For a most suppressed level of H3K27me3, the cells were treated with the tool inhibitor at 3 μ M. In figure 3.10, normalized mean values of the two generated data sets, each comprising 30 wells, are plotted as percentage of a mean value generated from three replicates of distinct DMSO control wells. The two data sets generated a Z'-factor of 0.7, describing an assay quality sufficient for screening large compound libraries [18].

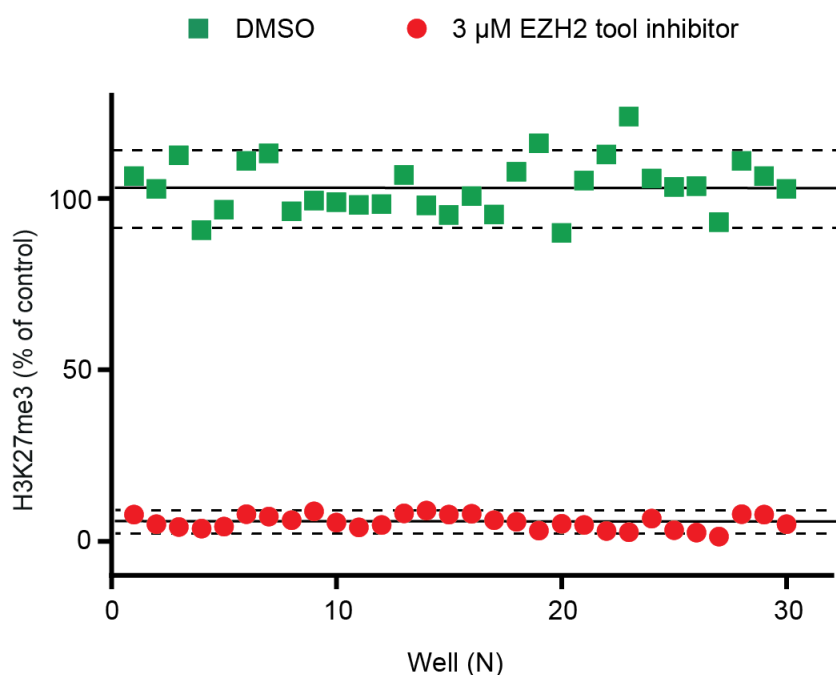


Figure 3.10: Z'-factor determination, in order to evaluate the assay quality, generated a value of 0.7 (qualified for screening [18]) for modulating H3K27me3 by EZH2 inhibition in a 384-well-plate format. MDA-MB-231 cells were treated with the EZH2 tool inhibitor at 3 μ M (red squares) or DMSO (green squares) up to three days. The graph shows the relative H3K27me3 level for a total of 60 wells holding approximately 650 cells per well. All responses are plotted as percentage of a mean value generated from three replicates of distinct DMSO control wells. Solid horizontal lines show the means generated of all single wells for EZH2 inhibitor treatment and DMSO control, respectively. The broken lines display three standard deviations (SD) from the means of each data set.

Moreover, to assess assay reproducibility and signal variation across assay plates over longer time periods, a determination of the Z'-factor and signal-to-background ratios (S/B) for six discrete assay plates is displayed in table 3.1. The processing chronology of all analyzed assay plates was separated by at least two weeks between single plates. Those independent data sets generated Z'-factors between 0.66 and 0.86 (n=6). S/B values were generated between 5.2 and 11.1, indicating a robust and reproducible assay.

Table 3.1: Determination of Z'-factors and S/B values for a set of six discrete 384-well-plates.

Plate no.	Mean S (grey levels)	SD S (grey levels)	Mean I (grey levels)	SD I (grey levels)	Z' factor	S/B
1	31192	897	3241	400	0.86	9.6
2	37425	2853	3360	137	0.74	11.1
3	33234	2264	4002	724	0.69	8.3
4	71626	3844	13853	41	0.80	5.2
5	37015	3097	5294	490	0.66	7.0
6	186848	10248	19399	1637	0.79	9.6

S, signal (DMSO control; maximal H3K27me3 level); I, inhibition (3 μ M Inhibitor; suppressed H3K27me3 level); SD, standard deviation; S/B, signal-to-background ratio. MDA-MB-231 cells were treated with the EZH2 tool inhibitor at 3 μ M or DMSO up to three days, processing a set of six discrete 384-well plates. All assay plates were processed, separated by time intervals of at least two weeks. Mean values represent the average of approximately 1500 nuclei analyzed. Standard deviations were generated from three replicates.

To explore the effects of two additional compounds together with the tool inhibitor and DZNep as cellular-active inhibitors of EZH2, I applied the assay set up to quantitatively characterize and benchmark the different inhibitors on their cellular activity for reducing global H3K27me3 levels and proliferative effects (fig. 3.11). To this end, I treated the cell lines HeLa S3 and MDA-MB-231 over three days with varying concentrations of: the tool inhibitor; EPI-0023 and EPI-0009 (two compounds reported early in 2009 to inhibit histone methyltransferases [178]) and DZNep (chemical structures are displayed in figure 6.5). EPI-0023 and EPI-0009 inhibit EZH2 with an enzymatic potency of 3 μ M and 25 μ M, respectively (targeted histone methyltransferases also include the HKMT PRSET7)[179].

Figure 3.11 A and C demonstrates that among the analyzed compounds, the tool inhibitor induced a strong, dose-dependent H3K27me3 suppression of at least 94% at a maximum for both cell lines as preliminary shown in figure 3.8. A reduction in the cell number of 50% and 40% occurred with the highest inhibitor concentrations of 30 μ M and 10 μ M for HeLa S3 and MDA-MB-231 (shown in figure 3.11 B and D and preliminary in fig. 3.8 A and C). Differently from this, DZNep induced in both cell lines a dose-dependent reduction in global H3K27me3 to approximately 65% at a maximum (figure 3.11 A and C) with a dose-dependent proliferative response, diminishing cell numbers to 60% and 40% at a maximum, respectively (figure 3.11 B and D). The two compounds, EPI-0023 and EPI-0009, did not alter the level of H3K27me3 globally with nearly no proliferative effect at the tested inhibitor concentrations

in both cell lines. Altogether, I conducted a cellular characterization of the different compounds, distinguishing selective and cellular active EZH2 inhibition from indirect EZH2 inhibition with concomitant proliferative effect or inhibition with non-effectual cellular potency.

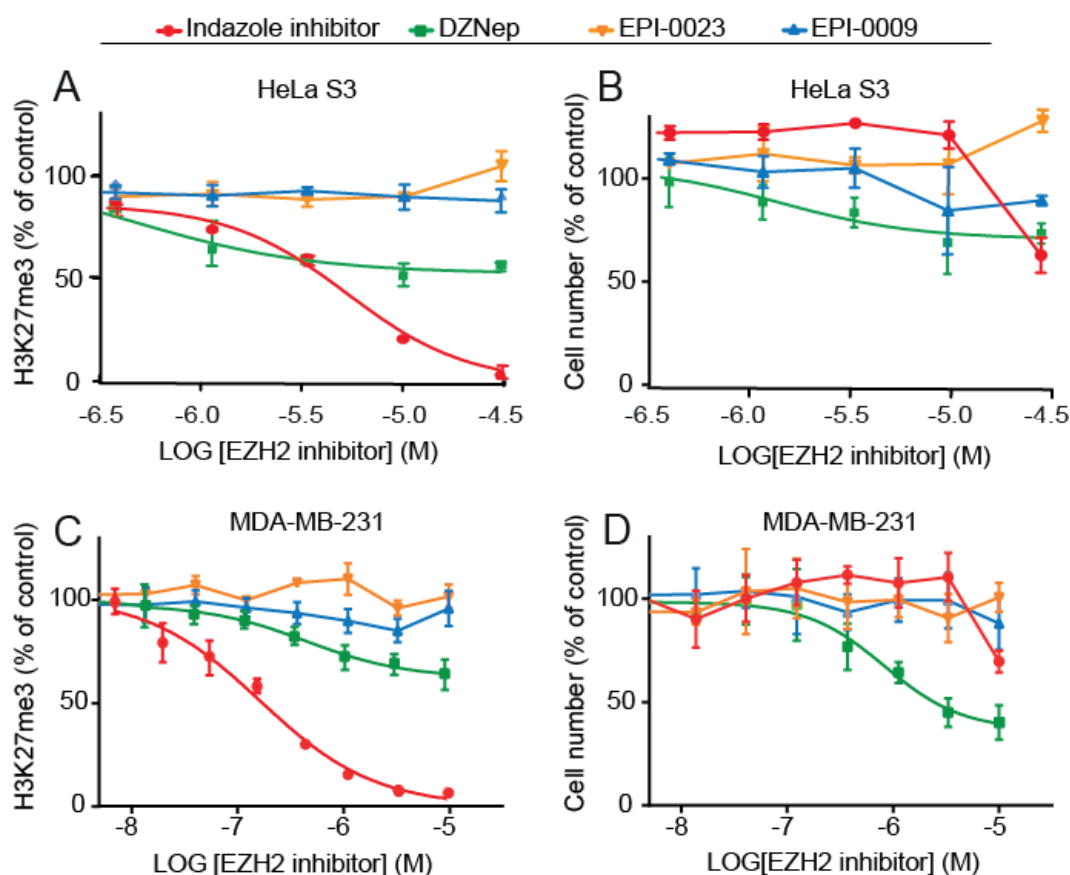


Figure 3.11: EZH2 inhibitors demonstrated distinct cellular inhibitory activity on H3K27me3 and proliferative effects. HeLa S3- (A and B) and MDA-MB-231 cells (C and D) were treated with varying concentrations of different inhibitors over three days. The graphs show the concentration response of the different EZH2 inhibitors in the relative H3K27me3 level (A and C) and in the relative number of analyzed nuclei (B and D). Evaluation of the cellular inhibitory activity of the EZH2 tool inhibitor on day three generated IC₅₀ values of 5 μ M and 133 nM in HeLa S3 and MD-MB-231 cells, respectively. DZNep induced a less potent, dose-dependent reduction in global H3K27me3 in both cell lines. Responses are plotted as percentage of the DMSO control. Mean values represent the average of approximately 1500 nuclei analyzed. Error bars show the standard deviation from three replicates.

3.2 Functional investigation of induced H3K27me3 suppression

In the first part of this work I describe the development and validation of a cellular mechanistic HTS-capable assay monitoring induced modulation of histone methylation by small-molecule HKMT inhibitors. In the following, the second part, I aimed to apply the method to functionally investigate a small-molecule induced suppression of H3K27me3 and to possibly contribute to the understanding of the mechanisms involved. For that reason, I used the new HCA platform to investigate induced H3K27me3 suppression and recovery, using the EZH2 tool inhibitor introduced in chapter 3.1.2.

3.2.1 Characterization of induced H3K27me3 suppression

To particularly examine a time dependency of an H3K27me3 reduction, induced by small-molecule EZH2 inhibition, I treated MDA-MB-231 cells with the tool inhibitor at various treatment times with a fixed concentration of 3 μ M and for a maximum of three days (3 μ M was the inhibitor concentration which induced the maximum effect on H3K27me3 but no effect on proliferation, as shown in figure 3.8 C). Figure 3.12 A demonstrates that H3K27me3 was reduced in a time-dependent manner to a maximum inhibition of 92% at day three. Notably, a treatment for six hours revealed an H3K27me3 reduction of already 25%. I investigated this observation in terms of the functionality of H3K27me3 suppression within chapter 3.2.2. Various inhibition times up to three days generated increased percent of H3K27me3 suppression with 75% for a two day- and 92% for a three day treatment. In addition, the data displays a genome-wide modification switch from H3K27me3 to acetylation of lysine 27 of histone 3 (H3K27ac). An H3K27me3 reduction of 25%, caused by an inhibition of EZH2 for six hours was accompanied by an increase in H3K27ac about 43% of the original level. In the following, H3K27ac increased about 53% at a two day- and 71% at a three day treatment, as shown in fig. 3.14 A.

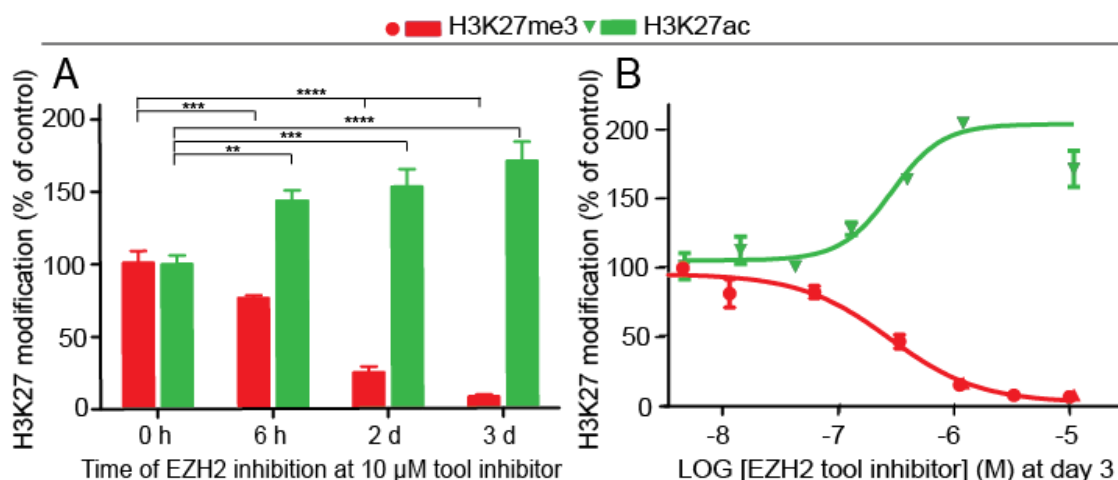


Figure 3.12: Small-molecule EZH2 inhibition induced a progressive H3K27me3 suppression over three days accompanied by a genome-wide modification switch from H3K27me3 to H3K27ac in MDA-MB-231 cells. The cells were treated with the EZH2 tool inhibitor for a maximum of three days. The graphs show the relative nuclear H3K27 modification levels at (A) after various treatment times using 3 μ M inhibitor and (B) after three days of treatment at inhibitor concentrations indicated. (B) Evaluation of the cellular inhibitory activity on H3K27me3 of the EZH2 tool inhibitor on day three generated an IC_{50} of 133 nM (average based on at least three independent experiments). A cellular activation of H3K27ac of the EZH2 tool inhibitor on day three generated an EC_{50} of 280 nM. Responses are plotted as percentage of the DMSO control. Mean values represent the average of 2000 nuclei analyzed. Error bars show the standard deviation from three replicates. By multiple comparisons, every mean was compared to the mean representing zero hours of EZH2 inhibition (0 h). ** $P \leq 0.01$; *** $P \leq 0.001$; **** $P < 0.0001$.

A three day inhibitor treatment, yielding the largest H3K27me3 inhibition of 92%, demonstrated a dose-dependent increase in H3K27ac almost symmetrical to an observed dose-dependent decrease in H3K27me3, up to 170% to 200% of the original level (figure 3.12 B). Evaluation of the cellular inhibitory activity on H3K27me3 of the EZH2 tool inhibitor on day three generated an IC_{50} of 133 nM (average based on at least three independent experiments), while a cellular activation of H3K27ac generated an EC_{50} of 280 nM. Representative confocal immunofluorescence images of EZH2 inhibitor treated MDA-MB-231 cells, probed for H3K27me3 and H3K27ac, are displayed in figure 3.13. The upper panel displays a staining of H3K27me3 (red) merged with a staining of the nuclei (blue) with increasing EZH2 tool inhibitor concentrations. The lower panel displays a staining of H3K27ac (green) merged with a staining of the nuclei (blue) at similar EZH2 tool inhibitor concentrations. The images display the genome-wide modification switch from H3K27me3 to H3K27ac at increasing EZH2 tool inhibitor concentrations, quantified in figure 3.12 B.

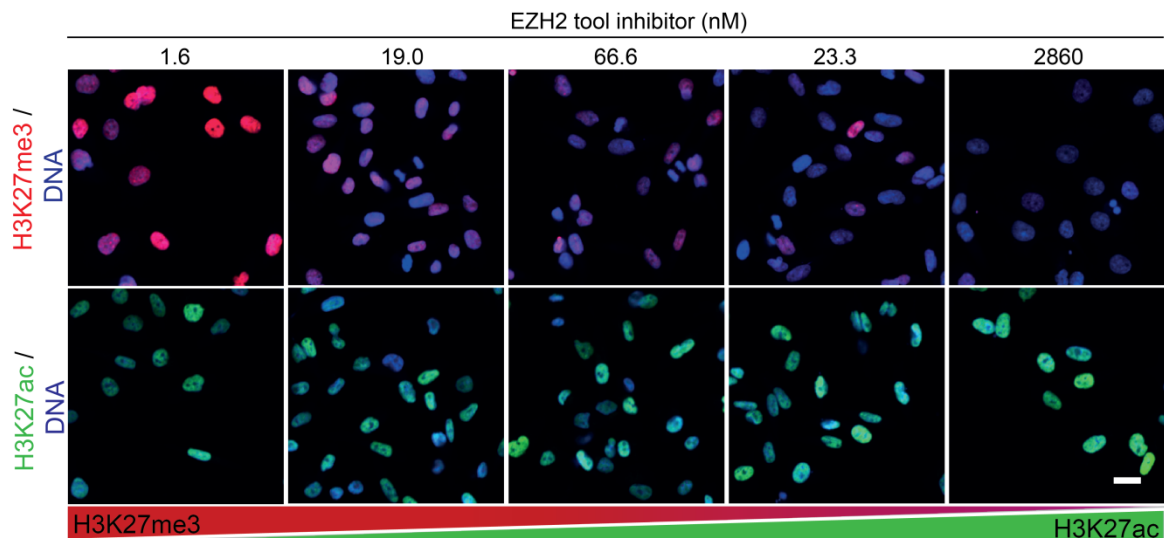


Figure 3.13: Representative confocal immunofluorescence images display a genome-wide modification switch from H3K27me3 to H3K27ac induced by small-molecule EZH2 inhibition in MDA-MB-231 cells. The cells were treated with the EZH2 tool inhibitor at various concentrations for three days. The upper panel displays a staining of H3K27me3 (red) merged with a staining of the nuclei (blue) with increasing EZH2 tool inhibitor concentrations, as indicated. The lower panel displays a staining of H3K27ac (green) merged with a staining of the nuclei (blue) at similar EZH2 tool inhibitor concentrations. The confocal images show a symmetrical antagonistic course of H3K27me3 and H3K27ac. Scale bar = 5 μ M. A quantification of the H3K27me3 and H3K27ac staining is shown in Figure 3.14.

The antagonistic course for H3K27ac induced by EZH2 inhibition has been confirmed with the cell lines HeLa S3 and MCF7, as shown in fig. 3.14 A and B. As shown primarily in figure 3.8, an evaluation of the cellular inhibitory activity of the EZH2 tool inhibitor on day three generated IC₅₀ values of 5 μ M and 442 nM for HeLa S3- and MCF7 cells, respectively. EC₅₀ values for a cellular activation of H3K27ac could not be determined because, for both cell lines, the courses of H3K27ac did not reach a plateau with the tested inhibitor concentrations. Altogether, I observed a time- and concentration dependency of inhibitor induced H3K27me3 suppression. Moreover, a loss of histone H3K27me3 loci seems to trigger a significant two-fold increase of H3K27 acetylation mark.

Though comparable overall changes in H3K27me3 can be observed, induced by small-molecule inhibition, I observed differences in the sensitivity towards an EZH2 inhibition with respect to a reduction in H3K27me3. As mentioned in the paragraph above and shown primarily in figure 3.8, generated IC₅₀ values of the EZH2 tool inhibitor on day three were 133 nM, 442 nM and 5 μ M, for MDA-MB-231-, MCF7- and HeLa S3 cells, respectively. Those

IC₅₀ values were confirmed in at least three independent experiments. Thus, the tool inhibitor was 38-fold more potent in MDA-MB-231 cells and 11-fold more potent in MCF7 cells compared to HeLa S3 cells.

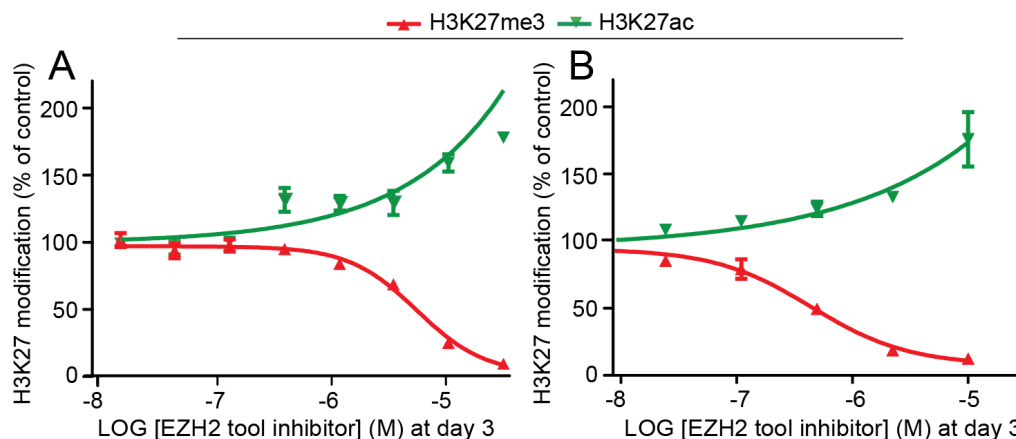


Figure 3.14: EZH2 inhibition induces a genome-wide modification switch from H3K27me3 to H3K27ac in HeLa S3- and MCF7 cells. HeLa S3- (A) and MCF7 cells (B) were treated with the EZH2 tool inhibitor for three days at various concentrations. The graphs show the relative H3 modification levels at inhibitor concentrations indicated. Both cell lines displayed a genome-wide modification switch from H3K27me3 to H3K27ac after EZH2 inhibition. Evaluation of the cellular inhibitory activity of the EZH2 tool inhibitor on day three generated IC₅₀ values of 5 μ M and 442 nM for HeLa S3- and MCF7 cells, respectively. EC₅₀ values for a cellular activation of H3K27ac were not determined because, for both cell lines, the courses did not reach a plateau at higher inhibitor concentrations. Responses are plotted as percentage of the DMSO control. Mean values represent the average of 2000 nuclei analyzed. Error bars show the standard deviation from 3 replicates.

A western blot detection of the original EZH2 protein level showed that non-treated HeLa S3 cells, demonstrating the lowest sensitivity towards H3K27me3 suppression, appeared to hold the highest level of EZH2 protein (as can be seen in figure 3.15). However, normalized to corresponding total H3 and relative to HeLa S3, I determined an EZH2 protein level of 82% in non-treated MDA-MB-231 cells whereas in non-treated MCF7 cells, only 36% was detected. Doubling times for the three cell lines were determined to be fairly similar for HeLa S3- and MDA-MB-231 cells, with 25 hours and 24 hours, respectively. A slower proliferation was determined for MCF-7 cells with a doubling time of 34 hours. The relevant proliferation curves are shown in the appendix, figure 6.1. Thus, no correlations could be observed between sensitivity towards EZH2 inhibition (with respect to a reduction of H3K27me3), EZH2 protein levels and the cell lines proliferation.

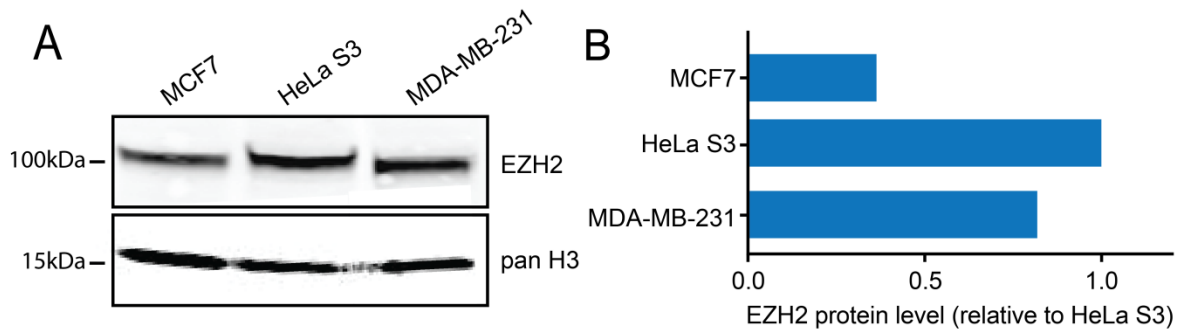


Figure 3.15: EZH2 protein levels vary between non-treated MCF7-, HeLa S3- and MDA-MB-231 cells, as determined in western blot analysis. (A) EZH2 protein level was detected by western blot analysis in non-treated MCF7-, HeLa S3- and MDA-MB-231 cells. (B) The graph shows the EZH2 protein level of each panel normalized to corresponding total H3 and relative to HeLa S3. Antibody signal intensities for EZH2 and corresponding total H3 were quantified using Li-Cor Odyssey® software.

In the following experiment, I aimed to determine the treatment time necessary to achieve a maximal H3K27me3 reduction. I showed earlier that an EZH2 inhibition at 3 μ M in MDA-MB-231 cells for six hours lead to an H3K27me3 reduction of already 25% (as shown in figure 3.12 A). Additionally to the observed early effect on H3K27me3, the subsequent experiment revealed an ongoing H3K27me3 reduction, induced by a small-molecule EZH2 inhibition of already six hours (shown in figure 3.16). Therefore, I treated MDA-MB-231 cells with the tool inhibitor at several concentrations and for the durations of six hours, one day, two days and three days at a maximum. After all treatment periods, the inhibitor was removed; the cells were suspended in media free of inhibitor and maintained until a maximum of three days. After an incubation period until day three, all tested durations of small-molecule EZH2 inhibition lead a comparable maximal H3K27me3 reduction. Here, an H3K27me3 reduction, induced by an inhibition over six hours and followed by incubation free of inhibitor, reached a maximal inhibition of 91% at day three. The maximal effect on H3K27me3, after an EZH2 inhibition for six hours, is comparable to the effect of a continuous inhibition of EZH2 over three days at similar inhibitor concentration. An evaluation of the cellular inhibitory activity of the EZH2 tool inhibitor for the different inhibitor treatment times, however, demonstrated to some extent varied IC₅₀ values, of 678 nM, 241 nM, 42 nM and 66 nM for the treatment times of six hours, one day, two days and three days, respectively.

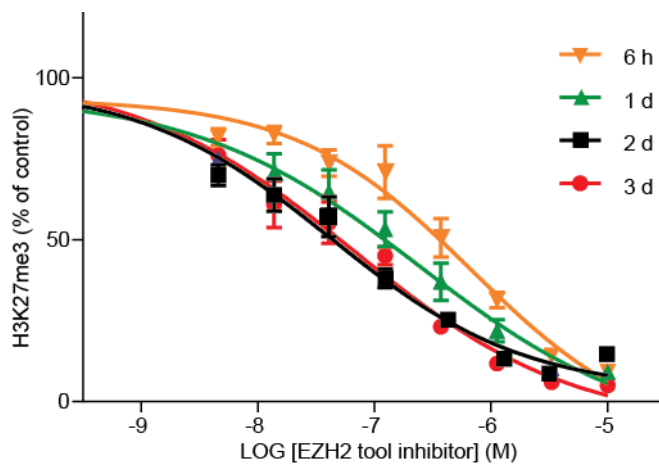


Figure 3.16: An EZH2 inhibition of six hours is sufficient to induce a reduction of H3K27me3, reaching a maximal measurable H3K27me3 suppression at day three. MDA-MB-231 cells were treated with the tool inhibitor at several concentrations and for the durations indicated. After treatment, the inhibitor was removed; the cells were suspended in media free of inhibitor and maintained until a maximum of three days. The graph shows the relative H3K27me3 level. Responses are plotted as percentage of the DMSO control. Evaluation of the cellular inhibitory activity of the EZH2 tool inhibitor

generated IC_{50} values of 678 nM, 241 nM, 42 nM and 66 nM for treatment times of six hours, one day, two days and three days, respectively. Mean values represent the average of 2000 nuclei analyzed. Error bars show the standard deviation from three replicates.

3.2.2 Search of mechanisms involved in induced H3K27me3 reduction

Histone methylation is generally viewed as a less transient mark [47-49], thus I found the observation that a six hour treatment with the EZH2 tool inhibitor induced an H3K27me3 reduction of already 25% (as shown in figure 3.12 A) very intriguing. In order to answer the question, if an induced early H3K27me3 suppression may basically depend on dilution of the mark through DNA replication or rather active removal (described in chapter 1.4), I applied the assay to investigate treated MDA-MB-231 cells after six hours of EZH2 inhibition at a tool inhibitor concentration of 3 μ M. All experiments were conducted using non-synchronized cells. An image analysis based discrimination of the cells into the different cell cycle phases, with subsequent quantification of global H3K27me3, revealed that cells in G1-, S- and G2-phase all underwent a comparable decrease in H3K27me3 after six hours of EZH2 inhibition, as shown in figure 3.17 A. Cells in G1 phase showed a reduction in H3K27me3 of 19%. A reduction in H3K27me3 of 11% was shown for cells in S- and a reduction of 27% for cells in G2 phase. No statistically significant difference in H3K27me3 reduction was determined between those three populations after six hours of EZH2 inhibition, as tested by multiple comparisons. Consequently, an induced early H3K27me3 suppression did not seem to depend on the cells passing the S-phase and thus, on a dilution of the mark through DNA replication.

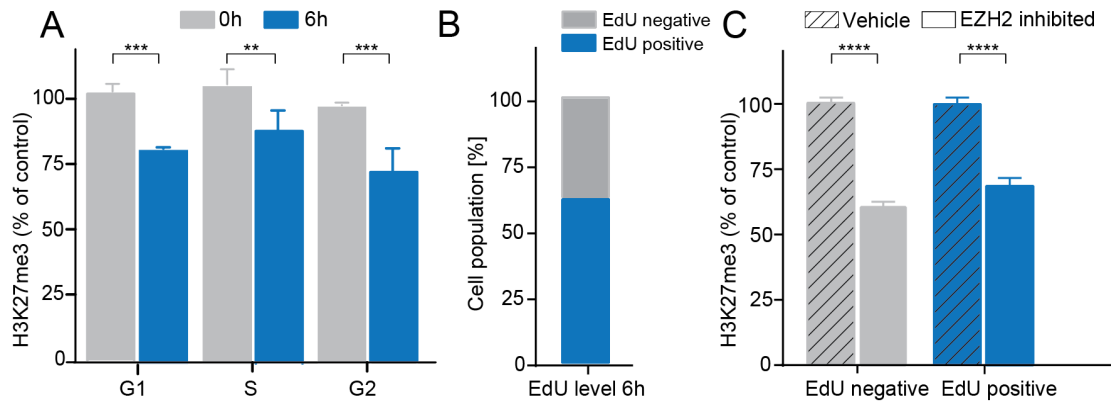


Figure 3.17: Small-molecule EZH2 inhibition reveals a dynamic, cell cycle independent H3K27me3 fraction.

(A, B, C) MDA-MB-231 cells were treated with 3 μ M tool inhibitor and (B and C) fluorescently labeled thymidine analogue EdU (10 μ M) for six hours. (A) The graph shows the relative H3K27me3 level in different cell cycle phases before and after six hours of EZH2 inhibition. All nuclei showed a comparable and significant degree of H3K27me3-demethylation, regardless of which cell cycle phase they were in. (B) The graph shows the percentage of cells with (blue) and without (grey) incorporated EdU after six hours of EZH2 inhibition, separating the cells into two populations. (C) The graph shows the relative H3K27me3 level of cells with and without incorporated EdU after six hours of EZH2 inhibition. Notably, cells showing incorporated EdU (blue, containing newly synthesized DNA) and cells showing no EdU incorporation (grey, containing no newly synthesized DNA) showed an H3K27me3 reduction after an inhibition of EZH2 for six hours. Mean values represent the average of 500 - 1500 nuclei analyzed. Responses are plotted as percentage of the DMSO control. Error bars show the standard deviation from three replicates. ** $P \leq 0.01$; *** $P \leq 0.001$; **** $P < 0.0001$.

To confirm this result, I aimed to accurately distinguish cells which newly synthesized DNA from cells which did not, following EZH2 inhibition, using an approach different from the one used above. For this purpose, I used a fluorescently labeled nucleoside 5-ethynyl-2'-deoxyuridine (EdU), which is incorporated into the DNA during its synthesis. I incubated MDA-MB-231 cells for six hours with the tool inhibitor at 3 μ M together with the modified thymidine analogue EdU. Via image analysis I discriminated the cells based on EdU incorporation. Figure 3.17 B shows that $62 \pm 0.08\%$ of the analyzed cells incorporated EdU after six hours of EZH2 inhibition whereas $38 \pm 0.08\%$ did not. The cells which demonstrated incorporated EdU, displayed an H3K27me3 decrease of 31%, as shown in figure 3.17 C. Notably, the analysis revealed an H3K27me3 reduction of 40% within cells which did not display incorporated EdU during the six hours of EZH2 inhibition and thus did not pass DNA replication yet. The results strengthens the former view of an induced early H3K27me3 suppression independent from a passage through the S-phase and therefore on a dilution of the mark through DNA replication.

For that reason, I intended to monitor a possible contribution of the two known H3K27-demethylases, UTX and JMJD3, on the turnover of H3K27me₃, as shown in figure 3.18. To this end, I used siRNA to knockdown EZH2 in comparison to EZH2 combined with UTX (siEZH2/siUTX), or with JMJD3 (siEZH2/siJMJD3). For a pure EZH2 knockdown, I applied either single siRNA targeting EZH2 (siEZH2) or siRNA targeting EZH2 combined with non-targeting siRNA in equal parts (siEZH2/siCon). All combined knockdown conditions, targeting demethylases, were conducted using two alternative siRNAs per demethylating enzyme. Moreover, every combined knockdown was conducted using the same amount of total siRNA (20 nM). Hence, 10 nM siRNA per enzyme were applied for all double knockdowns (siEZH2/siCon, siEZH2/siUTX and siEZH2/siJMJD3). A knockdown using a single siRNA targeting EZH2 (siEZH2) was conducted applying 10 nM siRNA. I used the human prostate cancer cell line PC3 for this experiment because similarly to HeLa S3 cells they are suitable for siRNA transfections and, at the same time, represent disease relevance and have been used previously as a model of advanced prostate cancer with EZH2 being a prerequisite for metastasis formation in vivo [180] and increased cell growth, invasiveness, and morphology changes in vitro [6, 181-183].

Figure 3.18 shows a quantification of global H3K27me₃, two days (A) and three days (B) after the conducted siRNA-mediated knockdowns normalized to cells treated only with transfection lipid. At day two after the knockdowns, I can see that all siRNA treatment conditions lead to a significant reduction on global H3K27me₃ of 19% to 36% (figure 3.18 A). I found no significant difference in global H3K27me₃ between the different siRNA treatment conditions themselves tested by multiple comparisons. After three days, a pure depletion of EZH2 (induced using both conditions; siEZH2 and siEZH2/siCon) lead to an H3K27me₃ reduction of 73% (fig. 3.18, B, grey columns). Notably, all double knockdowns implying the demethylases, UTX or JMJD3 (siEZH2/siUTX and siEZH2/siJMJD3) lead to a significant smaller reduction in H3K27me₃, decreasing global H3K27me₃ about 57% to 64% (fig. 3.18, B). Thus, a siRNA-mediated depletion of UTX and JMJD3, respectively, seemed to preserve 9% to 16% of global H3K27me₃ at day three of siRNA-mediated H3K27me₃ reduction, implicating a measureable contribution of the two known H3K27-demethylases on the turnover of H3K27me₃.

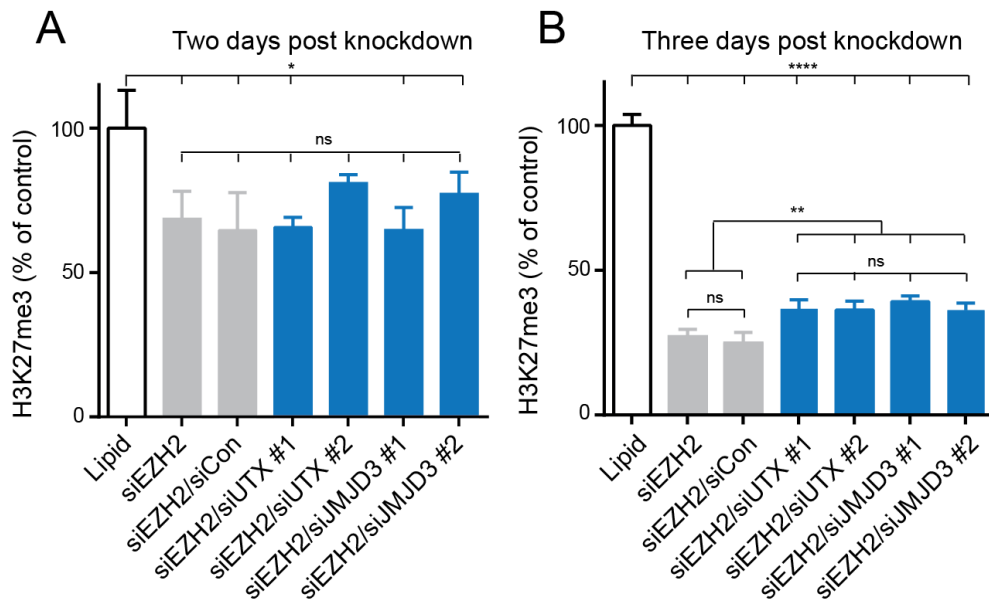


Figure 3.18: A knockdown of the demethylases UTX and JMJD3 significantly reduced EZH2 knockdown effects on methylation. (A, B) PC3 cells were treated with siRNA to knockdown EZH2 alone; EZH2 combined with a siRNA negative control (siCon); EZH2 combined with UTX or with JMJD3. The graphs show the relative H3K27me3 level at two and three days after knockdown. (A) All siRNA treatment conditions showed comparable and significant effects on global H3K27me3 at two days after knockdown. (B) A knockdown of UTX and JMJD3 significantly diminished EZH2 depletion effects on the global H3K27me3 level after three days. Similar results were observed in three independent experiments. Responses are plotted as percentage of the lipid control. Mean values represent the average of 1500 - 2000 nuclei analyzed. Error bars show the standard deviation from three replicates. ns = not significant; * $P \leq 0.05$; ** $P \leq 0.01$; *** $P \leq 0.001$

Representative confocal immunofluorescence images referring to the quantification of global H3K27me3 in figure 3.18 are displayed in figure 3.19. It can be observed that a knockdown of UTX (siEZH2/siUTX #1) and JMJD3 (siEZH2/siJMJD3 #1) diminished EZH2 depletion effects on the global H3K27me3 level, as shown by retaining H3K27me3 compared to a knockdown of EZH2 alone (siEZH2/siCon).

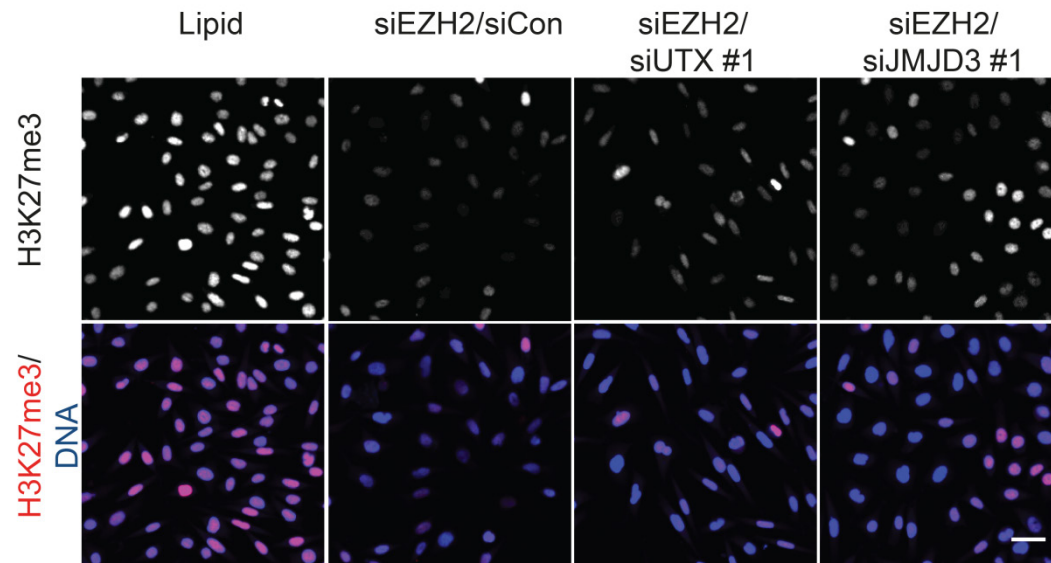


Figure 3.19: Representative confocal immunofluorescence images presenting a reduced EZH2 knockdown effect on methylation due to a parallel knockdown of the demethylases UTX or JMJD3, respectively. PC3 cells were treated with siRNA targeting EZH2 alone or in combination with UTX, JMJD3. The cells were immunostained at day three after knockdown. The upper panel displays H3K27me3 alone- (monochrome), the lower panel displays H3K27me3 (red) merged with a staining of the nuclei (blue) at the different knockdown conditions. A quantification of global H3K27me3 at the different knockdown conditions is shown in figure 3.18. Scale bar = 10 μ M. Images display PC3 cells treated with siRNA 1 targeting each demethylase, respectively (referring to the labeling in figure 3.18, 3.20 and 3.21). Similar results were observed using a second siRNA for each demethylase.

In order to confirm the validity of the results observed in figure 3.18 and 3.19, I aimed to determine the knockdown efficiencies for EZH2, UTX and JMJD3. Moreover, I aimed to test if each of the siRNA-mediated EZH2 knockdown conditions were equally successful in regard to depletion of EZH2. This needed to be given, in order to draw conclusions from different H3K27me3 levels, induced by the paralleled knockdown conditions. To this end, I tested the knockdown efficiencies for EZH2, UTX and JMJD3 for the conditions: siEZH2/siCon, siEZH2/siUTX (n=2 for both alternative siRNAs per demethylase) and siEZH2/siJMJD3 (n=2) by measuring the mRNA level using real-time quantitative PCR.

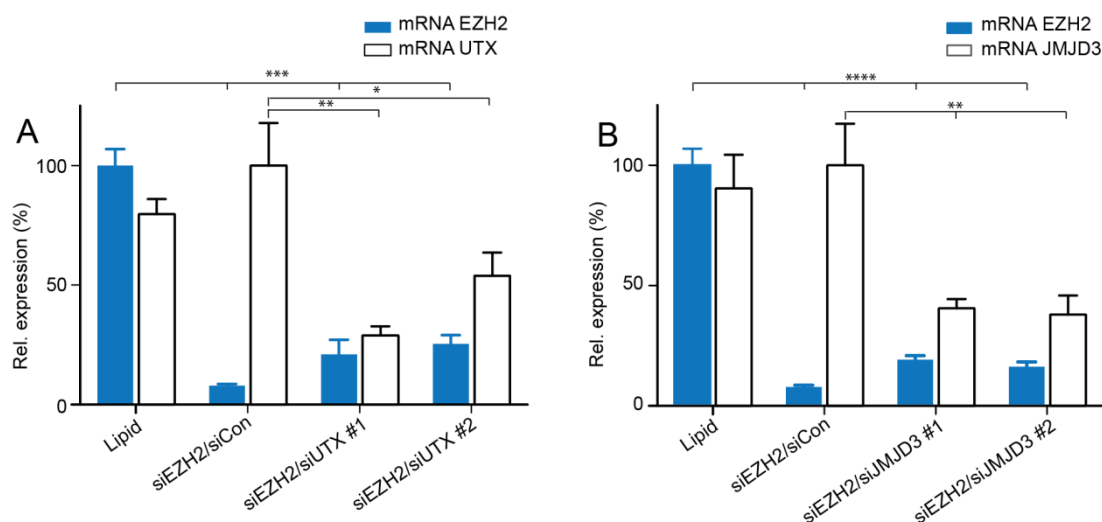


Figure 3.20: Reduced mRNA levels were observed at two days after combinational siRNA knockdown comprising EZH2 with UTX or EZH2 with JMJD3. The graphs show the mRNA levels of (A) EZH2 and UTX and (B) EZH2 and JMJD3, in different combinational knockdown conditions at two days after siRNA treatment, detected using qRT-PCR analysis. Gene expression is plotted as relative expression of the reference gene 18S, normalized to cells treated with transfection reagent (lipid) for EZH2 (A and B) or normalized to cells treated with EZH2-targeting and non-targeting control siRNA in equal parts (siEZH2/siCon) for UTX (A) or JMJD3 (B). For UTX and JMJD3, two alternative siRNAs were used, respectively. Plotted values represent the mean and standard deviation from three replicates. * $P \leq 0.05$; ** $P \leq 0.01$; **** $P < 0.0001$

For all three enzymes, a reduced mRNA level at day two after siRNA-treatment could be observed, as shown in figure 3.20 A and B. The mRNA level for UTX was reduced to 29% and 54%, induced by the two alternative siRNAs (figure 3.20 A). For JMJD3, the mRNA level was reduced to 38% and 41%, induced by the two alternative siRNAs (figure 3.20 B). The mRNA level for EZH2 was reduced to 8% using one siRNA targeting EZH2 in combination with a non-targeting control siRNA in equal parts (siEZH2/siCon). The double knockdowns of EZH2 and UTX (siEZH2/siUTX), using two alternative siRNAs for UTX, reduced the EZH2 mRNA level to 21% and 25% (figure 3.20 A). The double knockdowns of EZH2 and JMJD3 (siEZH2/siJMJD3) using two alternative siRNAs for JMJD3, lead to a reduced EZH2 mRNA level of 19% and 16% (figure 3.20 B). The differences in the EZH2 mRNA levels for the knockdown (siEZH2/siCon) in comparison to the double knockdowns comprising UTX (siEZH2/siUTX) and JMJD3 (siEZH2/siJMJD3) were significant, as tested by multiple comparisons (p-value ≤ 0.001 at a minimum). Altogether, the reduced mRNA levels for all three enzymes at day two after siRNA-treatment showed that the knockdowns were generally effective. However, the differences in the EZH2 mRNA levels for the different knockdown conditions (siEZH2/siCon),

(siEZH2/siUTX) and (siEZH2/siJMJD3) might indicate that each of the siRNA-mediated EZH2 knockdown conditions were not equally successful in regard to a depletion of EZH2 and, thus, might lead to different H3K27me3 levels.

To confirm these observations at the EZH2 protein level, I used a western blot analysis to detect EZH2 protein levels for all paralleled conditions at day three after knockdown. The data is shown in figure 3.21. The western blot analysis demonstrated comparable reduced EZH2 protein levels for the knockdown conditions using siRNA targeting: EZH2 and a non-targeting control siRNA in combination (siEZH2/siCon); EZH2 and UTX (siEZH2/siUTX), EZH2 and JMJD3 (siEZH2/siJMJD3) in combination and EZH2 alone (siEZH2). For UTX and JMJD3, the results for both used alternative siRNAs were shown, respectively. Consequently, with regard to the EZH2 protein levels after knockdown, a measurable contribution of the two known H3K27-demethylases on the turnover of H3K27me3 can be expected.



Figure 3.21: A western blot analysis demonstrates reduced EZH2 protein to comparable levels for all paralleled knockdown conditions quantified in figure 3.18. Western blot panels probed for EZH2 and corresponding total histone H3. The EZH2 protein level was evenly reduced at three days after knockdown using siRNA targeting: EZH2 and a non-targeting control siRNA in combination (siEZH2/siCon); EZH2 and UTX (siEZH2/siUTX), EZH2 and JMJD3 (siEZH2/siJMJD3) and EZH2 alone (siEZH2). For UTX and JMJD3, two alternative siRNAs were used, respectively.

3.2.3 Investigation of H3K27me3 recovery

Up to now, I turned the attention to the H3K27me3 reduction induced by the inhibition or depletion of EZH2. However, to potentially contribute to the understanding of a modulation of H3K27me3, I aimed to investigate a possible H3K27me3 recovery. To this end, I treated MDA-MB-231 cells for three days with the EZH2 tool inhibitor at 3 μ M. As noted before, for MDA-MB-231 cells, a concentration of 3 μ M induced the maximum effect on H3K27me3 but had no effect on proliferation (shown primarily in figure 3.8 C). I removed the inhibitor after the treatment and the cells were suspended and maintained in media free of inhibitor. During the experiment, I quantified the global level of H3K27me3 daily over 16 days. As expected, an inhibition of EZH2 over three days lead to a gradual, concentration-dependent reduction of H3K27me3 to 8%, reached at day three (as shown in figure 3.22). Notably, the experiment revealed that in MDA-MB-231 cells, global H3K27me3, profoundly reduced to an almost non-detectable level, was rebuilt to the original level in a time-depending manner.

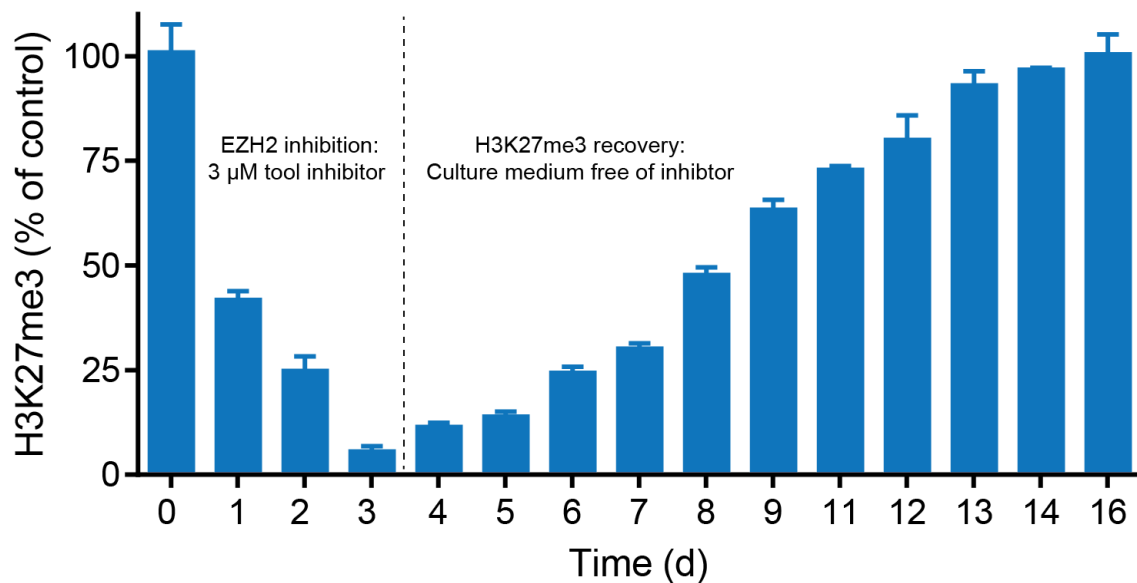


Figure 3.22: H3K27me3 restores after EZH2 inhibitor induced, profound suppression. MDA-MB-231 cells were treated with the EZH2 tool inhibitor at 3 μ M over three days. At day three, the inhibitor was removed and the cells were maintained in media, free of inhibitor. The graph shows the relative H3K27me3 levels at days indicated. Responses are plotted as percentage of the DMSO control. Mean values represent the average of 1000 nuclei analyzed. Error bars show the standard deviation from 3 replicates.

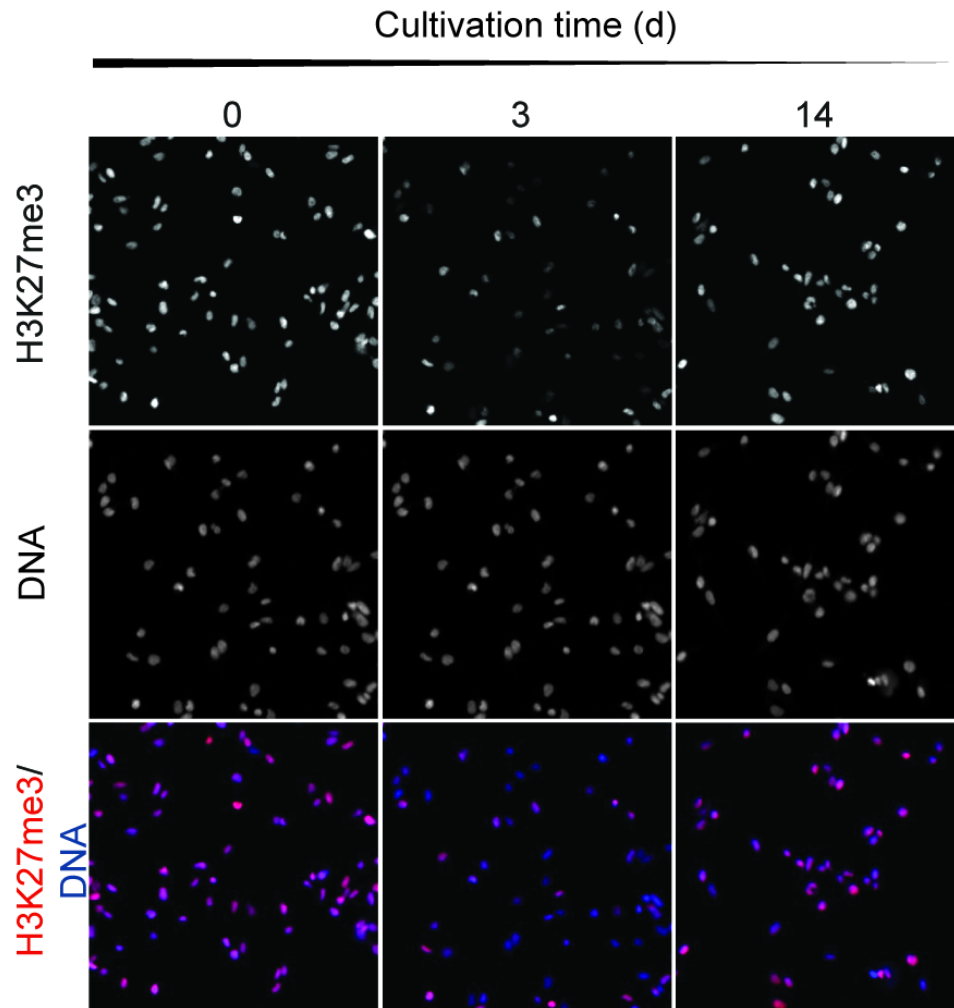


Figure 3.23: Representative confocal immunofluorescence images of H3K27me3 being restored after strong reduction induced by EZH2 inhibition. MDA-MB-231 cells were treated with the tool inhibitor at 3 μ M over three days. At day three, the inhibitor was removed and the cells were maintained in media, free of inhibitor. The upper panel displays H3K27me3 alone- (monochrome), the middle panel the Hoechst staining of the nuclei (monochrome) and the lower panel displays H3K27me3 (red) merged with the Hoechst staining of the nuclei (blue) at days indicated. A quantification of global H3K27me3 is shown in Figure 3.22. Scale bar = 10 μ M.

A complete recovery of global H3K27me3 occurred at day 14. Representative confocal immunofluorescence images of the quantification of global H3K27me3 reduction, followed by a complete recovery, are shown in figure 3.23. Nuclei before treatment with the EZH2 tool inhibitor are shown at day zero. At day three, the global H3K27me3 level decreased, induced by the inhibition of EZH2, reaching an almost not visible level of H3K27me3. After inhibitor removal at the same day, followed by a recovery period under normal culture conditions, the cells did not show sensitivity towards EZH2 inhibitor treatment. H3K27me3 restored to full

extent, reaching original H3K27me3 levels at day 14. Nuclei which showed a full recovery of H3K27me3 appear similar to nuclei of non-treated MDA-MB-231 cells, displaying their original H3K27me3 level. Thus, I discovered full reversibility of the inhibitor treatment on the global level of H3K27me3.

Besides looking at average treatment effects, the analysis of single nuclei allows for the detection of possible heterogenic effects upon inhibitor application. Figure 3.24 A displays the frequency distributions of H3K27me3 signal intensities of the same cell population, at the three different sampling days; before a treatment with the EZH2 tool inhibitor, after a treatment with the EZH2 tool inhibitor at day three, demonstrating profound H3K27me3 demethylation, and after completed H3K27me3 recovery. Note that the cells were not synchronized and therefore within different cell cycle phases. According to their DNA content, cells in G2 phase can hold higher global levels of H3K27me3 compared to cells in G1 phase of the cell cycle, altogether generating a certain band width of H3K27me3 signal intensities within the cell population. Moreover, the proliferation of the cells was not effected by an inhibition of EZH2 over three days with inhibitor concentrations not exceeding 3 μ M (this was shown in figure 3.8).

The fractions of at least 2000 nuclei from non-treated MDA-MB-231 cells formed a frequency distribution of their H3K27me3 signal intensities with a slight right tail and its peak representing a fraction of 30% of the total nuclei comprising an H3K27me3-specific antibody signal intensity of approximately 50000 (as shown in figure 3.24 A). After an inhibition of EZH2 for three days, a homogenous reduction in global H3K27me3 for the entire cell population was detected. The fractions of at least 2000 nuclei of EZH2 inhibitor-treated MDA-MB-231 cells formed a completely narrowed frequency distribution of their H3K27me3 signal intensities. Its peak represents a fraction of 59% of the total nuclei comprising an H3K27me3-specific antibody signal intensity of approximately 15000. Finally, after completed recovery of H3K27me3 at day 14, the fractions of at least 2000 nuclei form a frequency distribution of their H3K27me3 signal intensities nearly identical to non-treated cells.

An image analysis based discrimination of these cells into the different cell cycle phases is shown in figure 3.24 B. In a non-treated cell population, 61% of the total cells belonged to G1, 16% belonged to S phase and 21% belonged to G2 phase. An inhibition of EZH2 until day

three did not induce any changes in the cell cycle populations. However, when the level of H3K27me3 was fully recovered at day 14, the cells displayed negligible changes on the cell cycle, demonstrating an increase in G2 and M-phase of 7% (Significant,* $P \leq 0.05$) and a decrease of 5% in G1 phase, compared to non-treated cells at day zero.

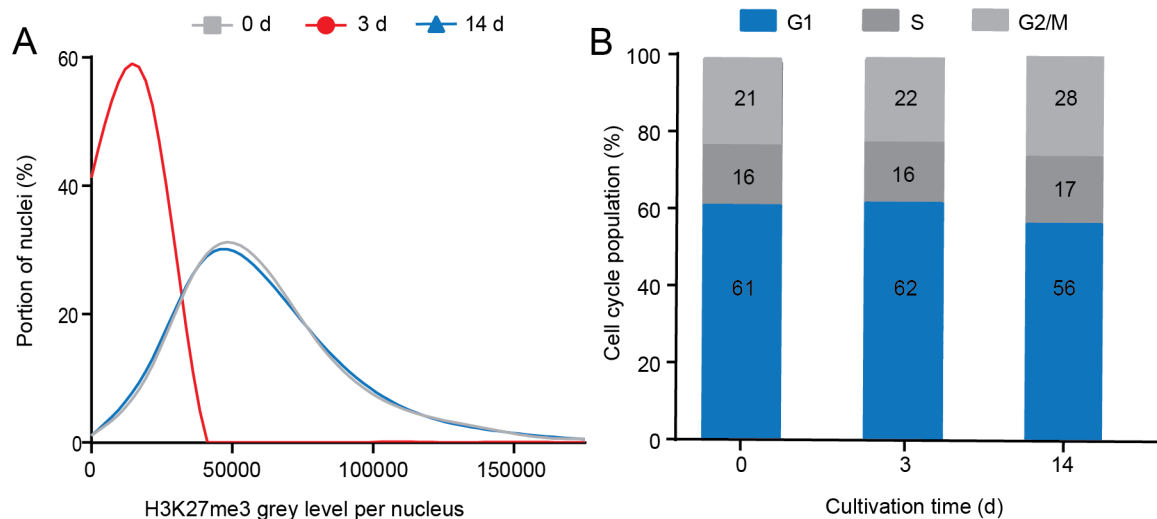


Figure 3.24: H3K27me3 reduction and recovery occurred homogeneously for every cell of the inhibitor treated population, with marginal effects on the cell cycle. (A and B) MDA-MB-231 cells were treated with the tool inhibitor at 3 μ M for three days. At day three, the inhibitor was removed and the cells were maintained in media, free of inhibitor. At least 2000 nuclei per sampling day were analyzed. (A) The curves show the frequency distributions for global H3K27me3 across the entire cell population at the original level (day zero, grey), after H3K27me3 reduction (day three, red) and after H3K27me3 restoration (day 14, blue), presented primarily as average relative H3K27me3 level for the cell population at each day in figure 3.22. Each value represents the fraction of total nuclei belonging to each of the non-overlapping intervals of signal intensity. (B) The graphs show the cell populations within the cell cycle phases G1, S and G2 together with M, at days indicated. Cell cycle populations were normalized to a DMSO control.

Altogether, the data shows that modulation and full reversibility of the inhibitor treatment on the global level of H3K27me3 occurred homogeneously for every cell of the population. A profound suppression of the average relative H3K27me3 level for a cell population (as shown in figure 3.22) was not generated by just a fraction of the population undergoing strong H3K27me3 reduction while another, smaller fraction was left being unchanged in their global level of H3K27me3. Except for negligible changes in the G1 and G2 phase populations of the cells showing accomplished H3K27me3 recovery at day 14, no changes in the cell cycle

populations occurred throughout H3K27me3 reduction and recovery. Thus, no changes in the cell cycle populations contributed to an overall decrease in global H3K27me3 and the observed changes in global H3K27me3 appeared to be caused by H3K27me3 suppression only.

As a final experiment, I aimed to investigate if an H3K27me3 recovery observed at the global level could be confirmed locally on the level of single EZH2 target genes as well. To this end, I investigated the effect of a profound H3K27me3 reduction with subsequent full H3K27me3 recovery on the expression of a selection of 10 polycomb regulated genes (figure 3.25).

I determined the mRNA level of the genes: ADRB2; APOL3; CDH1; DAB2IP/AIP1; HOXC8; IFI27; POU5F1 (Oct-4); SLIT; SOX2 and TNFRSF21 in non-treated cells, in the same cells after displaying profound H3K27me3 demethylation due to EZH2 inhibition over three days, and after showing full H3K27me3 recovery (at day 14). Figure 3.23 displays the relative gene expression of the tested genes based on their mRNA level for the mentioned sampling time points, determined using real-time quantitative PCR.

Here, I can see that the genes HOXC8, IFI27, POU5F1 (Oct-4), SLIT, SOX2 and TNFRSF21 were all significantly upregulated to different degrees after EZH2 inhibition over three days (maximal $P \leq 0.01$). A particular profound upregulation was observed for the two transcription factors, POU5F1 and SOX2, showing a 15-fold and 12-fold higher expression compared to the DMSO control. Notably, except for IFI27 and SLIT, all upregulated genes, including POU5F1 and SOX2, returned to their original expression levels at day 14, when H3K27me3 was fully restored. The same trend was observed for IFI27 and SLIT. However, their expression level did not decrease to their original level yet, at day 14. Despite intense inhibitor induced H3K27me3 reduction with subsequent H3K27me3 recovery, the genes ADRB2, APOL3, CDH1 and DAB2IP/AIP1 did not show an effect on their mRNA levels at the three sampling time points. Overall, with the genes HOXC8, IFI27, POU5F1 (Oct-4), SLIT, SOX2 and TNFRSF21, I was able to demonstrate full reversibility of the inhibitor treatment at the level of EZH2 target gene expression. This is an important finding for the potential clinical use of EZH2 inhibitors for cancer therapy and, moreover, it poses so far unresolved questions regarding the mechanisms involved in an H3K27me3 reestablishment after profound H3K27me3 reduction to an almost undetectable level.

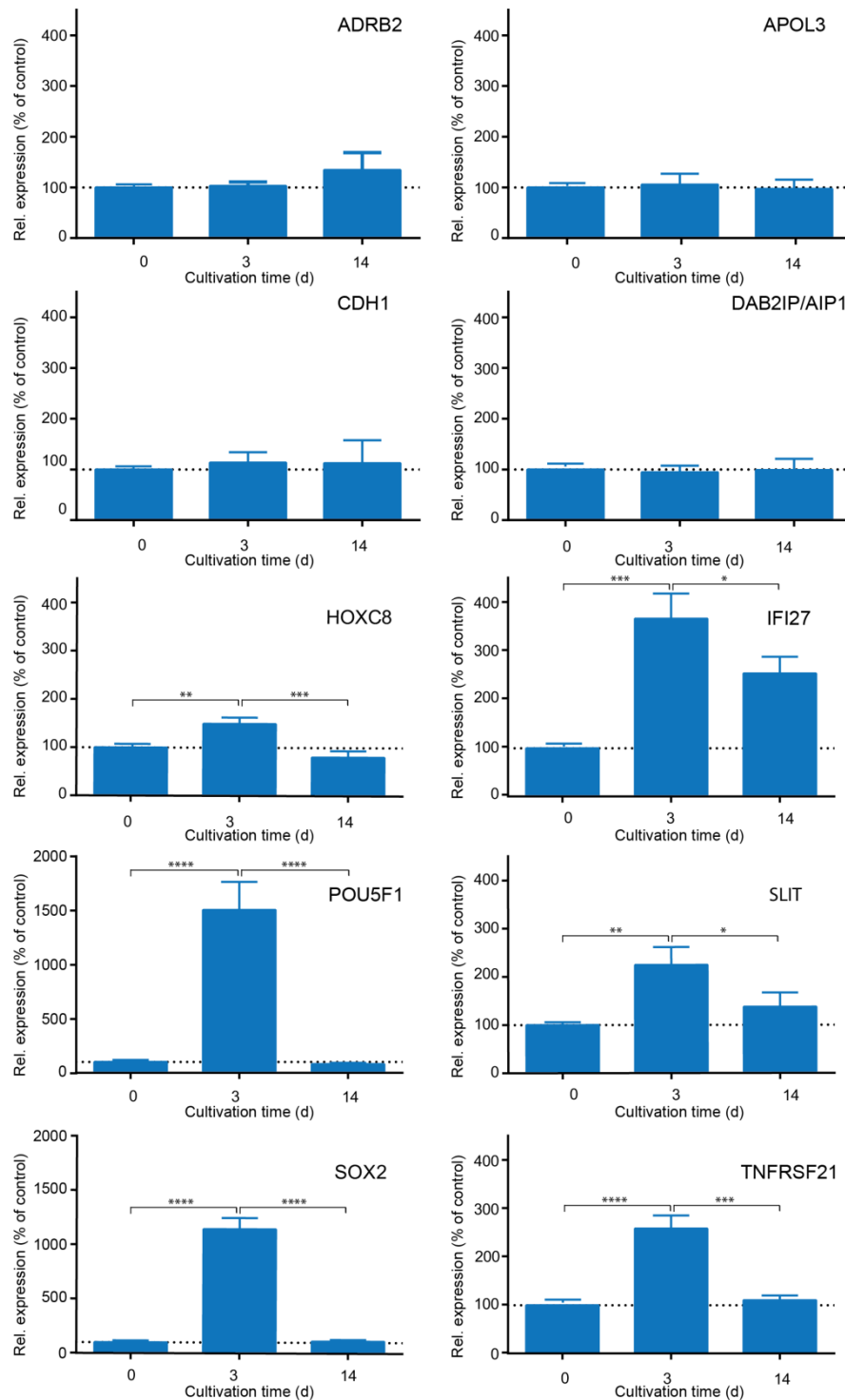


Figure 3.25: H3K27me3 reduction was paralleled with an upregulation of the expression of the polycomb regulated genes HOXC8, IFI27, POU5F1 (Oct-4), SLIT, SOX2 and TNFRSF21, while a subsequent H3K27me3 recovery occurred together with repression of these genes. MDA-MB-231 cells were treated with the tool inhibitor at 3 μ M for three days. At day three, the inhibitor was removed and the cells were maintained in media, free of inhibitor. At days indicated, the cells were harvested and gene expression was analyzed using qRT-PCR analysis. Gene expression is plotted as relative expression of the reference gene 18S, normalized to cells treated with DMSO. Plotted values represent the average and standard deviation from three replicates. The results were confirmed in at least two independent experiments. * $P \leq 0.05$; ** $P \leq 0.01$; *** $P \leq 0.001$, **** $P < 0.0001$

4. Discussion

4.1 HKMT HCA assay

Current efforts are focused on the identification of probe molecules for epigenetic modifying enzymes like EZH2, to investigate the role of these enzymes in normal physiology and pathology and to eventually evaluate drug candidates for a clinical use. However, in drug discovery, it has been challenging to develop cell-based assays for the monitoring of small-molecule inhibition of EZH2 or other chromatin-modifying enzymes, which are amenable for screening and compound profiling. A cellular assay is usually more physiologically relevant and less artificial than a biochemical assay because intact cells and native cellular environment are used. An identification of inhibitors with biochemical approaches does not necessarily guarantee that the identified candidates will have cellular activity. Because of the biological complexity associated with the regulation of EZH2 and H3K27me3, a phenotypic cellular mechanistic assay simultaneously encompassing relevant cellular processes was desirable.

4.1.1 Global versus local histone modification levels

By targeting the selected HKMTs EZH2, DOT1L, MLL2, MLL, SMYD2 and NSD1 with siRNA, using the cervix cancer cell line HeLa S3, I aimed to quantify a possible induced modulation of different respective histone methylation marks. Testing the HCA assay concept, this was accomplished through a parallel analysis of nuclear morphology together with the measurement of the signal intensity of the site-specific histone modification antibody (figure 3.1 shows a scheme of the image analysis). Using siRNA-mediated knockdown, I was able to quantify a strong and significant reduction in H3K27me3 of about 84% at three days after knockdown, using the HCA approach as shown in figure 3.2. Overall, reduced mRNA levels confirmed that the siRNA-mediated knockdown for all six HKMTs was successful (figure 3.3). Less profound effects could be observed for the knockdowns of MLL and MLL2. A knockdown of MLL2 reduced H3K4me3 significantly about 12% to 37%, induced by all three siRNAs. A knockdown of MLL reduced H3K4me3 significantly about 23%, but induced by only one of the two siRNAs tested. Here, additional siRNAs targeting MLL need to be tested in order to confirm the observed effect on H3K4me3. On the contrary, for the three HKMTs DOT1L,

NSD1 and SMYD2, I was not able to measure a modulation of H3K79me2, H3K36me2 or H3K4me3, respectively, at three days after knockdown, using a minimum of two siRNAs targeting distinct regions of the enzymes transcript.

The HKMT HCA assay quantifies different histone lysine modifications at the global level. HKMTs differ in the lysines they are targeting and also in the insertion of mono-, di- or trimethylation [184]. Some site-specific histone methylation marks are known to be catalyzed by more than one HKMT while others are known to be catalyzed by mainly a single HKMT. This presumably explains why I was able to quantify a strong and significant reduction in H3K27me3 of about 84% at three days after EZH2 knockdown but only less profound or no effects after a knockdown of other HKMTs. A methylation of H3K27 is mainly achieved by EZH2 [185, 186]. The mammalian EZH2-homolog EZH1 forms similar PRC2 complexes but it is suggested that H3K27 methylation is performed only weakly by EZH1. Global H3K27me3 levels were reported to be affected by a knockdown or inhibition of EZH2 while a knockdown of EZH1 was ineffectual on global H3K27me3 [187]. However, a small contribution to H3K27me1 and H3K27me2 was suggested by the HKMT G9a and possibly GLP 1 [188, 189]. Different from this, a methylation of H3K4 or H3K36 is conducted by a number of different HKMTs. A knockdown of one single HKMT, like MLL, MLL2, SMYD2 or NSD1, may therefore affect these modifications locally on different genes but may not or not measurably affect the global level of H3K4 or H3K36. However, I was still able to quantify a global effect on H3K4me3, although less profound than on H3K27me3, induced by a knockdown of at least MLL2.

4.1.2 Mechanistic assay validation

With the aim to eventually profile compounds modulating different HKMTs in the cell, I targeted the HKMTs G9a and GLP1 in HeLa S3 cells using the small-molecule inhibitors BIX01294 [167] and UNC0638 [8]. I evaluated their cellular inhibitory activity by quantifying a dose-dependent H3K9me2 reduction down to 65%, with UNC0638 being more potent (shown in figure 3.6 A). Different from EZH2 with H3K27me3, there are at least five mammalian H3K9 HKMTs: SUV39H1, SUV39H2, G9a, GLP1 and SETDB1 [122, 190, 191]. Nevertheless, selective inhibition of G9a and GLP1 leads to a reduction in H3K9me2 to 65%. The generated data are in line with previously reported observations of a decrease of

H3K9me2, induced by selective small-molecule induced inhibition of G9a and GLP 1 using both selective inhibitors [8, 167].

Furthermore, I quantified a strong reduction of H3K27me3 (to barely detectable amounts) induced by small-molecule inhibition of EZH2 using the tool inhibitor in the cell lines MDA-MB-231-, MCF7- and HeLa S3 cells. In contrast, DZNep induced an effect on H3K27me3 with considerably less potency than the tool inhibitor, but with concomitant effect on proliferation in the same cell lines. It has been shown in previous reports that EZH2 depletion and inhibition induces a decrease in global H3K27me3 levels [92, 93, 168-174]. A decrease in H3K27me3 induced by DZNep was reported by others using western blot data [192]. Indirectly inhibiting histone methyltransferases, DZNep has been shown to disrupt PRC2, to reduce H3K27me3 and to preferentially induce apoptosis in cancer cells, resulting presumably in the dose-dependent, concomitant proliferative effect [177, 192-195]. As an overall result, the data validate the assay procedure and functionality by confirming previous observations of a global decrease in H3K9me2 or H3K27me3. Moreover, the data demonstrate the universality of the assays and their easy adaption with regard to a variety of different histone modifications.

4.1.2.1 A symmetrical antagonistic course for H3K27ac

A modulation of H3K27me3 potentially influences other post-translational modifications on the same or other histone molecules such as lysine 36 of histone H3 or the methylation of DNA itself [196, 197]. I was able to show a symmetrical antagonistic course for H3K27ac in MDA-MB-231-, HeLa S3- and MCF7 cells induced by an inhibition of EZH2 (figure 3.12, 3.13 and 3.14). Thus, a loss of histone H3K27me3 marks seems to trigger a significant and almost two-fold increase of the H3K27 acetylation mark. No alterations for a broad panel of other histone methylation marks except for H3K27me3 and H3K27ac were induced in the three cell lines by the inhibition of EZH2, as expected based on the biochemical selectivity of the EZH2 tool inhibitor (Figure 3.9 A, B and C) [175]. This was previously demonstrated for lymphoma cells using western blot analysis [93]. Here, a modest increase in H3K27ac was likewise reported for the lymphoma cell line OCI-LY19. Acetylated H3K27 is postulated to be antagonistic to Polycomb mediated silencing and is enriched in the absence of PRC2 and the repressive modification mark H3K27me3 [83, 198]. Further, a genome-wide switch from

methylation to acetylation is reported to correlate with transcriptional activation of polycomb repressed genes in embryonic stem cells [198]. The same report suggested that Polycomb-mediated repression is partly conducted by preventing the binding of acetyltransferases to Polycomb repressed target genes [198].

Following treatment with the non-specific inhibitor DZNep, I quantified a parallel, concentration-dependent decrease of H3K27me3 and H3K4me3, in contrast to a concentration-dependent profound reduction specifically of H3K27me3, induced by the EZH2 tool inhibitor (as presented in figure 3.9 D, E and F). As mentioned earlier, DZNep has been recently used to probing the cellular function of EZH2 and H3K27me3, before the discovery of potent and selective small-molecule EZH2 inhibitors. However, probing cellular functions of EZH2 using DZNep is complicated by DZNep's ability to inhibit different methylation marks targeted by HKMTs other than EZH2 [192]. This further emphasizes the need for selective small-molecule inhibitors and thus on a cell-based assay amenable for a comprehensive screening of selective and cellular active inhibitors targeting EZH2 or other HKMTs.

For the first time the data present quantitatively a genome-wide and dose-dependent increase in H3K27ac, almost symmetrical to a decrease in H3K27me3 induced by the inhibition of EZH2. In contrast to my data, a slight interplay between H3K27me3 and H3K36me2 was observed for the lymphoma cell line OCI-LY19, suggesting that the degree of this interplay might be dependent on the cellular context [93]. Altogether, the results validate the assay by confirming previous observations of a modification switch of global H3K27me3 to H3K27ac with no alteration for a broad panel of other histone methylation marks, induced by the inhibition of EZH2 [83, 93].

4.1.3 Technical assay quality

DMSO ($(\text{CH}_3)_2\text{SO}$) is a water miscible solvent that has, among other areas, wide applications in cell biology. It is used as a solvent for drugs [199], as a cryoprotectant [200, 201], chemical penetration enhancer to deliver active molecules through the skin and into the cells [202] cell fusogen [203], and inducer of cell differentiation [204]. The amphiphilic property, wide temperature range of the liquid state, and high polarity of DMSO make it a particularly efficient solvent for many types of substances, including both organic and inorganic

compounds [205]. DMSO was used as a solvent for the small-molecule inhibitors in this study.

The data showed that by using DMSO as a solvent at percentages up to 0.5%, no dose-dependent H3K27me3 reduction was induced in HeLa S3 cells (see figure 3.7). With increasing DMSO concentrations above 0.5%, a reduction of H3K27me3 correlated with proliferative effects. However, throughout this work, the portion of DMSO applied in the assay did not exceed 0.3% at any time for the cell line HeLa S3 or 0.1% for the cell lines MCF7 or MDA-MB-231. In all tested cell lines a profound decrease of global H3K27me3 was not concomitant with proliferative effects, when induced through selective inhibition (as can be seen in figure 3.8). Thus, DMSO was not supposed to compromise the assays readout under assay conditions. Nevertheless, I partly used a parallel quantification of total histone H3 for control, ensuring that a reduction of H3K27me3 was not caused by a total loss of histone H3 (see figure 3.9).

To ensure that the automated HCA assay fulfills all performance criteria for screening, high value on all assay material and reagents was set to meet adequate quality and maintained consistency. For instance, the use of good quality primary and secondary antibodies, providing a clear staining with very little background, in combination with a robust image analysis algorithm strengthened the reliability and reproducibility. Further, an implementation of automated liquid-handling devices ensured reliable sample processing. As a result, the data showed an assay reproducibility and assay quality throughout, enabling screening of large compound libraries in 384 -well plate format, as demonstrated by the calculated Z'-factors between 0.66 - 0.86 (n=6) and S/B values between 3.2 - 11.1 for MDA-MB-231 cells (figure 3.10 and table 3.1). Generally, an assay generating Z'-factors between $1 > Z' \geq 0.5$ is categorized as excellent with a large separation band [18]. Based on this evaluation, the HCA approach was considered fit for screening of large compound libraries, using a 384-well plateformat for the moment.

However, there were examples showing technical artifacts in the quantification of histone modifications. While the inactivated BIX01294 derivate was not expected to inhibit G9a and GLP1, a putative increase in the H3K9me2 signal intensity at higher inhibitor concentration was observed (as shown in figure 3.6 A). Similar to this, an increase in H3K36me2 and total

histone H3 was observed, induced by DZNep at higher concentrations (shown for HeLa S3 cells in figure 3.9 D). However, these examples represent technical artifacts due to a decrease in nuclei size, leading to compaction followed by a brightening of the antibody signal intensity. This was possibly caused by initiated cytotoxicity at higher inhibitor concentration, as demonstrated in figure 3.6 B and 3.11 B and D. In all three examples, a parallel effect on proliferation was shown. Using the image analysis algorithms, segmented nuclei were filtered for size, shape and highly elevated signal intensity to exclude possible non-viable cells along with metaphase nuclei (metaphase nuclei were excluded from the analysis because of their likewise strong compaction resulting in a heavy increase in antibody signal intensity). For all that, depending on the used settings, technical artifacts as described above can still occur when nuclei, affected by an initiated decrease in size, were not spared of the analysis successfully through filtering based on their size and shape.

4.1.4 Evaluation of the EZH2 HCA assay

Two HCA platforms were previously reported by others to be configured to monitor modulations of histone modifications. A quantification of total histone H3 acetylation within cell populations and tissues was described. Here, the effect of valproic acid (VPA) as a histone deacetylase inhibitor (HDACi) on histone H3 acetylation levels was quantified in human neuroblastomal cells (SK-N-SH) using wide-field fluorescence microscopy [206]. Nuclei segmentation was based on the histone H3 acetylation antibody staining itself and no parallel chromatin staining was applied, allowed by the fact that an increase instead of a decrease in H3 acetylation was quantified. Thus, H3 acetylation antibody staining intensity was always detectable throughout any inhibitor concentration.

Another report describes the pharmacological assessment of the inhibition of ectopically expressed JMJD3 (KDM6B) demethylase enzyme, using H3K27me3 as assay readout [207]. In contrast to the EZH2 HCA assay, a restoration of H3K27me3 after inhibition of exogenous JMJD3 was quantified, using Hoechst stain for nuclei recognition. The described platform has been used to prosecute a screen of 87.500 compounds resulting in a selection of JMJD3 chemotypes with intrinsic cellular permeability and potency. In the present work, a modulation of H3K27me3 and other histone modification marks was quantified after the application of siRNA nucleotides or small-molecule inhibitors, targeting different endogenous

HKMTs. Sufficient assay accuracy and sensitivity was assured through optimized staining protocols and image analysis algorithms, such as filtering the segmented nuclei for size, shape and highly elevated signal intensity to exclude possible non-viable cells or metaphase nuclei (see chapter 2.1.7.1).

In general, HCA combines robust statistical significance with high informational yield of cellular imaging. Performing the EZH2 HCA assay, 600 - 800 cells per well were analyzed individually with multiple replicates per sample across different treatment conditions, allowing a high degree of statistical reliability, compared to a determination of averaged cell population effects. I have demonstrated the assay's accuracy to differentiate cellular inhibitor potency and efficacy by benchmarking the different inhibitors UNC0638, BIX01294, DZNep or the EZH2 tool inhibitor, inducing a concentration-dependent decrease in global H3K9me2 or H3K27me3 (as can be seen in figure 3.6 A and 3.11 A and C). The demonstrated ability to analyze the genome-wide modification shift from H3K27me3 to H3K27ac (fig. 3.12, 3.13 and 3.14) as well as different histone marks in parallel (in form of multiplexed assays, fig. 3.9) forms an appropriate dual-readout to monitor small-molecule EZH2 inhibitors by their cellular activity with more validity and informative value. False positive hits (e.g. technical H3K27me3 staining artefact) will be discovered due to a lack of change in global levels of H3K27ac. Moreover, selective modulation of global H3K27me3 will be assured through parallel assessment of different modification marks. Altogether, the EZH2 HCA assay enables a phenotypic and mechanistic characterization of compounds possibly inhibiting endogenous EZH2 with high informational value (e.g. cellular downstream and morphological effects via multiplexing or heterogenic effects through the analysis of single nuclei).

4.2 Characteristics of H3K27me3 reduction in response to EZH2 inhibition

4.2.1 Identification of a dynamic, cell cycle independent H3K27me3 fraction

Methylation of H3K27 is considered to be a dynamically regulated process [57-59]. EZH2 (the “writer”) and the antagonistic demethylase enzymes (the “erasers”) identified to date, UTX and JMJD3, are suggested to govern a steady-state balance [59, 95-98]. Nevertheless, methylated lysine residues appear to be chemically more stable than other modifications on

histones and are therefore proposed to be of less transient nature [47-49, 155]. Therefore, I found the observation, that inhibitor treated MDA-MB-231 cells displayed a reduction in global H3K27me3 of already 25% after six hours of EZH2 inhibition, very intriguing (figure 3.12 A). An inhibition of H3K27me3, beginning earlier than 24 hours and reaching a maximum after two days, was reported previously for a selective small-molecule inhibition of EZH2 in diffuse large B-cell lymphoma (DLBCL) [92]. Moreover, I showed a phenotypic and mechanistic monitoring of siRNA-mediated knockdown of EZH2 and its direct effect on the global H3K27me3 level in a time-course experiment (displayed in figure 3.4 and 3.5). The data demonstrated an EZH2 depletion very closely correlated to a reduction in global H3K27me3 level, indicating an immediate H3K27me3 turnover without delay. This immediate answer to the EZH2 knockdown in the form of a direct decrease in H3K27me3 emphasizes histone methylation being a flexible and dynamic process.

Different models describing how the repressive mark H3K27me3 is maintained throughout the cell cycle (the generally excepted model of the 'self- propagation mechanism' of PRC2 is described in 1.4). When EZH2 is inhibited (inhibition of de novo methylation), a dilution of the mark through DNA replication occurs. Considering this, I took up the observations described above in order to elucidate if an early effect on H3K27me3, induced by small-molecule EZH2 inhibition, may basically depend on dilution of the mark through DNA replication or rather active removal (e.g. by histone exchange or demethylases).

The cells used in the former experiment were in different cell cycle phases, as I did not apply any synchronizing agents to minimize other induced effects that could interfere with the turnover of H3K27me3. Therefore, cells that display a reduction in H3K27me3 of already 25% after six hours of EZH2 inhibition may have been representing replicating cells in S-phase that had not been able to methylate newly deposited nucleosomes on the DNA daughter strands due to the inhibition of EZH2. Instead, a discrimination of the cells into the different cell cycle phases, based on an image analysis with subsequent quantification of global H3K27me3, showed that cells in G1-, S- and G2-phase all underwent a similar decrease in H3K27me3 after six hours of EZH2 inhibition (figure 3.17 A). The cell cycle phase in which the cells were in, seemed not to be a determining parameter for the observed early H3K27me3 reduction.

Thus, there has to be a cell cycle independent action reducing the level of H3K27me3 about 25%.

I supported this hypothesis by accurately determining cells which have not synthesized new DNA during the inhibition of EZH2 over six hours, but showed a remarkable H3K27me3 reduction, using an approach different from the one used above. The cells which have not newly synthesized DNA during the inhibition of EZH2 were determined by their lack of EdU incorporation. EdU (a fluorescently labeled thymidine analogue) is incorporated into DNA during its synthesis. Using image analysis, I discriminated $38 \pm 0.08\%$ cells of the total population, lacking EdU (figure 3.17 B). Moreover, I quantified an H3K27me3 reduction of 35% within these cells (fig. 3.17 C). They represent a cell population which was not replicating in S-phase during EZH2 inhibition. Thus, a reduction in H3K27me3 was not induced by H3K27me3 dilution due to the cells being hindered to methylate newly deposited nucleosomes on the DNA daughter strands, caused by an inhibition of EZH2. Altogether, the data suggests an H3K27me3 turnover, which is independent from replication. It may result from a dynamic H3K27me3 fraction, which seems to be constantly maintained by PRC2.

The two JmjC domain-containing demethylases, UTX and JMJD3, catalyze a reversal of H3K27 methylation. They preferentially demethylate H3K27me3, followed by H3K27me2, and have been suggested to ensure a dynamic switch of transcriptional repression by active mechanisms of H3K27me3 reduction [59, 95-98]. With the aim to monitor a possible contribution of UTX and JMJD3 on the turnover of H3K27me3, I conducted a siRNA knockdown experiment, depleting EZH2 in comparison to EZH2 combined with UTX (siEZH2/siUTX), and with JMJD3 (siEZH2/siJMJD3), as shown in figure 3.18 and 3.19.

At day three after knockdown, a pure depletion of EZH2 (using two different knockdown conditions; siEZH2 and siEZH2/siCon) lead to an H3K27me3 reduction of 73% (fig. 3.18, B). Notably, the double knockdowns implying the demethylases, UTX or JMJD3 (siEZH2/siUTX and siEZH2/siJMJD3) lead to a significant smaller reduction in H3K27me3 to 57 - 64%. Thus, a siRNA-mediated depletion of UTX and JMJD3, respectively, retained 9% to 16% of global H3K27me3 at day three of siRNA-mediated H3K27me3 reduction.

However, it is not clear whether the difference between the EZH2 mRNA levels for the knockdown conditions siEZH2/siCon and siEZH2/siUTX or siEZH2/siJMJD3, as shown in figure 3.20, was biologically significant and directly translated into different levels of EZH2 protein. The western blot analysis shown in figure 3.21 did not suggest this. It demonstrated comparable reduced EZH2 protein levels for the different conditions. Overall, the quantified effect of a knockdown of the two demethylases UTX and JMJD3 by HCA (figure 3.18), demonstrating a significantly reduced EZH2 knockdown effect on methylation, displayed a result with the largest statistical reliability, as 1500-2000 single nuclei were analyzed.

Interestingly, there was no effect on the H3K27me3 turnover at two days after a siRNA-mediated knockdown by JMJD3 or UTX, while a reduction in H3K27me3 was already visible (as shown in figure 3.18 A). This might be caused to differences in the half-life of EZH2 protein and the two demethylases UTX and JMJD3. The time until a possible knockdown effect is detectably translated into the mechanistic readout H3K27me3 depends among other factors on the stability of the targeted protein. However, it is notable that a knockdown of both demethylase enzymes caused a comparable effect on global H3K27me3 at day three after knockdown (as shown in figure 3.18 B), suggesting that both enzymes, UTX and JMJD3, contribute to a turnover of H3K27me3 to a similar extent. However, UTX and JMJD3 are suggested to not function redundantly. This is based on the finding that UTX proteins contain tetratricopeptide repeats (TPRs) at their N-terminal regions but JMJD3 does not [59, 95-98]. TPRs are structural motifs identified in a variety of proteins and are important for protein-protein interactions [208].

Altogether, the data show evidence for a detectable contribution of the two demethylases UTX and JMJD3 to a reduction in H3K27me3, while EZH2 is depleted or presumably as well inhibited. However, non-detectable differences in the level of EZH2 protein may have biased the observed results demonstrated in figure 3.18 and 3.19. Moreover, a detectable contribution of UTX and JMJD3 to a reduction in H3K27me3 may depend on the cellular context. Nevertheless, UTX and JMJD3 are the two only known demethylases to date shown to catalyze a reversal of H3K27 methylation [59, 95-98]. I demonstrated earlier that active removal of H3K27me3 occurred within six hours of EZH2 inhibition; therefore a detectable contribution of the two demethylases on the H3K27me3 turnover is very likely.

Overall, the data strengthen the suggestion that active removal of the H3K27me3 mark seems to be an important mechanism to modulate a considered dynamically regulated H3K27me3 level [57-59]. They indicate that a decrease in global H3K27me3, induced by EZH2 inhibition, comprises two distinct mechanisms: the inhibition of de novo methylation establishment, and a dynamic, replication independent, H3K27me3 turnover. However, considering the fact that an EZH2 inhibition over three days is necessary to achieve maximal H3K27me3 reduction (figure 3.12 A), the portion of dynamic H3K27me3 removal versus the inhibition of de novo methylation establishment seems to be minor. The data show that EZH2 inhibition over three days generated an increasing reduction of H3K27me3, with a maximum inhibition of 92%, suggesting the inhibition of de novo methylation establishment to be the main cause for H3K27me3 reduction (i.e. incorporation of unmethylated H3K27 into chromatin through histone turnover and replacement). The data are in line with observed H3K27me3 reduction in mutant EZH2 bearing lymphoma cells induced with the indazole inhibitors EPZ005687 and GSK126 [92, 93]. Moreover, a similar characteristic was reported for a reduction of H3K79me2, after potent and selective DOT1L inhibition with the inhibitor EPZ004777 in MLL-rearranged leukemia cell lines [133]. Both reports describe an H3K27me3- or H3K79me2 diminution, which was apparent after 24 hours and not fully realized until day four to five. Notably, there is no histone demethylase specific for H3K79 reported so far and a turnover rate of methylated H3K79 with $t_{1/2} \sim 1.1$ to 1.8 days, was determined to be similar to that of histone H3 itself ($t_{1/2} \sim 1.3$ days) [47, 209]. Thus, as for H3K27me3, an inhibition of de novo methylation establishment seems to be a main driver for H3K79me2 reduction after DOT1L inhibition. In summary, an inhibition of EZH2 or DOT1L (and presumably other HKMTs) displays particular characteristics of a cellular response [21]. When using H3K27me3 reduction as a pharmacodynamic readout for cellular EZH2 inhibitor activity, there will be always a time of days between exposure to the inhibitor and full pharmacodynamics response (as shown in figure 3.12 A)

4.2.2 Distinct separation of H3K27me3 reduction and proliferative effects

To accurately assess cellular viability, we used the morphologic parameters, nuclei size and shape. The cell lines MDA-MB-231, MCF-7 and HeLa S3, bearing homozygous wild-type EZH2, demonstrated a distinct separation of H3K27me3 reduction and proliferative effects after the

inhibition of EZH2 over three days, as shown in figure 3.6. Moreover, proliferative effects only occurred with highest inhibitor concentration at 30 μ M for HeLa S3 and 10 μ M for MDA-MB-231 cells. A profound H3K27me3 reduction in MCF-7 cells, as shown in figure 3.6 B, occurred with no proliferative effect even at the highest inhibitor concentration (10 μ M). The prompt decrease in proliferation with higher inhibitor concentrations suggests an anti-proliferative effect rather caused by compound cytotoxicity than mechanistically by H3K27me3 reduction.

Using the non-specific inhibitor DZNep, the data showed a concomitant, dose-dependent effect on proliferation in HeLa S3 and MDA-MB-231 cells (as can be seen in figure 3.11 B and D) which was not linked to an H3K27me3 reduction in the tested cell lines (as proven by selective inhibition of EZH2 using the tool inhibitor).

WT EZH2 overexpression and increased levels of H3K27me3 are correlated with poor prognosis and promote metastasis in different solid tumors including breast, prostate and B-cell lymphoma [6, 7, 43, 110-112]. However, previously published data reported a treatment up to 11 days with indazole inhibitors of similar structure, potency and EZH2 selectivity than the used EZH2 tool inhibitor (e.g. EPZ005687 [93] and GSK126 [92]), which induced limited impact on the growth of homozygous wild-type EZH2-containing lymphoma cells, approving the observed results described above. In contrast, apoptotic killing of different mutant EZH2 bearing DLBCL cells with growth IC_{50} values of 28 nM to 861 nM (heterozygous for EZH2 point-mutations at either Tyr641 or Ala677) was described, suggesting a critical dependency on EZH2 activity for cells carrying point-mutated EZH2 [92, 93]. Further, EZH2 inhibition using the inhibitor GSK126 was reported to markedly inhibit the growth of EZH2 mutant DLBCL xenografts in mice [92]. In addition, a depletion of switch/sucrose nonfermentable complex component (SMARCB1) in pediatric malignant rhabdoid tumors (MRTs) displayed oncogenic dependency on EZH2. Here as well, selective small-molecule inhibition of EZH2 using EPZ-6438 induced apoptosis and differentiation. A treatment of xenograft-bearing mice caused a dose-dependent regression of MRTs with correlative diminution of intratumoral levels of H3K27me3 [171].

One explanation or feature of the EZH2 dependency may be that the EZH2 Tyr641 mutation for instance appears to be an unusual gain-of-function mutation, as described in 1.5 [24]. It was postulated that this mutation may change EZH2 target gene specificity and so alter DNA

methylation at PcG targets [4]. Moreover, Tyr641 EZH2 mutation was shown to have an aberrant functional cooperation with the wild-type EZH2 resulting in an hyper-trimethylated state causing gene repression [3]. Chromatin immunoprecipitation (ChIP) of EZH2 from Tyr641 EZH2 mutated DLBCL cells, followed by microarray analysis (ChIP on chip), demonstrated the hyper-trimethylation and repression of several key cell cycle-related tumor-suppressor genes (e.g. *CDKN1a*, *CDKN1b*) which may contribute to the malignant transformation of normal germinal center (GC) B cells into DLBCL cells [118].

An impact on cellular proliferation induced by an inhibition of EZH2 was reported to be measurable already after two to three days for the most sensitive mutant EZH2 bearing Pfeiffer cell line but with latency periods in other mutant EZH2 bearing lymphoma cells. They were showing an H3K27me3 diminution apparent after 24 hours and not fully realized until day four, followed by a period from day four to 11 in which the impact on cellular proliferation was realized [92, 93]. A similar behavior was reported for a H3K79me2 reduction in MLL-rearranged leukemia cell lines, induced by potent and selective DOT1L inhibition, suggesting this delay in proliferation effect may be a frequent feature of protein methyltransferase inhibition [133]. Co-occurring alterations may override the dependence of the cell on EZH2 activity, making it less sensitive to EZH2 inhibition. Among EZH2 mutant cell lines, sensitivity to the inhibition of EZH2 was reported to modestly correlate with an inhibition of H3K27me3 but with no correlation to EZH2 protein levels [92]. Although only three different cell lines were analyzed, this is in line with the observation that an evaluation of the EZH2 tool inhibitors cellular inhibitory activity generated decreasing IC₅₀ values of 5 μ M, 442 nM and 133 nM for HeLa S3-, MCF7- and MDA-MB-231 cells, respectively, demonstrating different degrees in sensitivity towards EZH2 inhibition with respect to a reduction in H3K27me3 (figure 3.8). I observed no correlation between sensitivity towards EZH2 inhibition (reduction of H3K27me3) and EZH2 protein levels or doubling times (as shown in figure 3.17 and figure 6.3 in the appendix). Overall, additional lymphoma and other solid tumor cells need to be characterized genomically and epigenomically combined with a treatment of small-molecule EZH2 inhibitors, to reveal determinants of sensitivity against an inhibition of EZH2.

In mammals, epigenetic regulation of gene expression is normally represented by different engaging epigenetic layers. In addition to histone modification, DNA methylation and mammalian messenger RNA (mRNA)/long noncoding RNA (lncRNA) modification are involved in gene regulation. In fact, mRNA and lncRNA contain a variety of internal transcriptional chemical modifications. The most abundant modification is N⁶-methyladenosine (m⁶A) [210, 211]. For the modification m⁶A in mRNA/lncRNA, “writers”, “erasers” and “readers” have now been identified, highlighting the idea that RNA modifications may act in epigenetic control, similarly to DNA methylation [212, 213]. DNA methylation, the addition of a methyl group at the carbon 5 position of the cytosine ring in CpG dinucleotides (5mC), is the predominant epigenetic modification in mammals and the key mechanism of epigenetic regulation. It is established and maintained by DNA methyltransferases (DNMTs) [214]. By inhibition of EZH2 and prevention of *de novo* methylation of H3K27, only one layer of presumably various, altogether executing gene repression, is modulated, and may therefore not be sufficient to impact growth of a range of homozygous wild-type EZH2-containing malignancies. In contrast, in an aberrant system, like for instance in mutant EZH2 bearing DLBCL cells or depleted SMARCB1 bearing MRTs, critical addiction to EZH2 is observed. Here, a modulation of only one layer of the epigenetic system seems to be sufficient to induce an impact on gene regulation.

Another observation was described regarding a treatment of epithelial ovarian cancer cells (EOC) with another structurally related indazole EZH2 inhibitor GSK343. The inhibitor was reported to decrease the level of H3K27Me3, with profound effect at day three, but exhibited only limited effects on the cell growth of EOC cells. Here, a treatment of the same cells but cultured in 3D matrigel extracellular matrix (ECM), instead of 2D cell culture, significantly suppressed the growth of EOC cells after EZH2 inhibition induced by the inhibitor GSK343 after 12 days [215], indicating possible additional determinants of sensitivity of solid tumor cells to selective EZH2 inhibition.

In this study, to precisely quantify small-molecule modulated levels of H3K27me3 and other histone modifications for screening purposes or functional investigation of reduction mechanisms (as we conducted in chapter 3.2), a distinct separation of functional and proliferative effects was desirable. I therefore chose cancer cell lines for this work which

were relevant regarding aberrant EZH2 expression and cancer, which were suitable for the use in HCA (e.g. appropriate morphology) but were not sensitive towards EZH2 inhibitor treatment. However, for investigating EZH2 inhibited cells, bearing a critical dependency on EZH2 activity for proliferation [92, 93], the multi-parametrically designed HCA approach, simultaneously measuring as many of the relevant cellular processes as possible, may represent an eligible tool as well. In experimental setups with prolonged treatment times, possible time- and concentration-depending correlations between an inhibitor induced impact on different cellular processes and H3K27me3 reduction may be analyzed.

4.2.3 Reversibility of H3K27me3 modulation

Altogether, the data shows that an inhibitor induced reduction of global H3K27me3 is followed by a H3K27me3 recovery, in every cell of the tested population (figure 3.22, 3.23 and 3.24). Moreover, with the genes *HOXC8*, *IFI27*, *POU5F1* (*OCT-4*), *SLIT*, *SOX2* and *TNFRSF21*, I was able to demonstrate full reversibility of the inhibitor treatment to occur locally on different Polycomb regulated genes as well (figure 3.25). The relative plasticity as a feature of epigenetic changes in malignancy (in contrast to genetic changes to DNA sequence that are essentially permanent) has important clinical relevance, making these malignancies more amenable to inhibitor therapies that reverse the epigenetic alterations. However, a similar important clinical relevance for the potential use of EZH2 inhibitors has the finding of full reversibility of the inhibitor treatment. This finding may indicate that healthy tissues would not be permanently affected by a modulation of the methylation mark.

A recovery of a reduced methylation mark was also reported for a reduction in H3K79 methylation after an inhibition of the MLL-AF4 expressing acute leukemia cell line MV4-11 with the DOT1L inhibitor EPZ-5676 [2]. Different to the data in this work, measuring H3K27me3, H3K79me2 demonstrated a lag phase of three days in which no increase of H3K79me2 was observed. This might be due to a larger drug-target residence time, as observed in different biochemical assays for EPZ-5676 [216]. The time required to rebuild global H3K27me3 in this study was 10 days, after inhibitor removal. The time necessary for H3K27me3 to recover may be determined by the drug-target residence time of the tool inhibitors as well.

It has been shown that H3K27me3 binds the non-enzymatic PRC2 component EED and, as a consequence, allosterically activates EZH2 in its HKMT activity [102]. It was recently reported, that this activation leads to an increased residence time inhibition of EZH2. This was described for the structurally related EZH2 inhibitor GSK126, suggesting that the pyridone ring is structurally important for a slow release of the inhibitor from allosterically activated EZH2 [217].

The described increased residence time inhibition of EZH2 is presumably reflected by the observation that an EZH2 inhibition of six hours is sufficient to induce an ongoing reduction of H3K27me3, reaching a maximal measurable reduction at day three (as shown in figure 3.16). An evaluation of the cellular inhibitory activity of the EZH2 tool inhibitor generated decreasing IC₅₀ values for treatment times of six hours, one day, two days and three days, respectively. Here, it would have been interesting to be able to test different selective inhibitors targeting EZH2, demonstrating short drug-target residence times to compare with. However, it is not clear how to interpret the differences in IC₅₀ values between the different treatment times. Although reproduced in two independent experiments, the differences were rather minor. It is possible that the difference in IC₅₀ values are caused by global H3K27me3, already started to recover for the various inhibitor concentrations, especially for a treatment of six hours.

Concerning the mechanisms involved in the modulation of H3K27me3, the finding of an H3K27me3 recovery after H3K27me3 reduction to an almost undetectable level, poses so far unresolved questions regarding the mechanisms involved in an H3K27me3 reestablishment. The described self-propagation mechanism of PRC2 ensuring an H3K27me3 stability throughout the cell cycle does not satisfactorily explain the observed H3K27me3 re-establishment [99-102]. The described recognition of pre-existing H3K27me3 is proposed as a mechanism to maintain repressed chromatin domains by re-establishing H3K27me3 onto nascent nucleosomes being incorporated during DNA synthesis. This would presume a basal level of H3K27me3. However, the profoundness of H3K27me3 reduction as shown in figure 3.22, 3.23 but also 3.12 may not ensure this. Instead of the model of self-propagation, suggested mechanisms for initial PRC2 recruitment, comprising interactions of the different PRC2 complex partners with DNA or histones (among others) may be involved [94].

Moreover, yet unknown mechanisms, enabling the complete re-establishment of H3K27me3, may function here additionally or exclusively.

Figure 3.25 shows that the Polycomb regulated genes *HOXC8*, *IFI27*, *POU5F1* (*OCT-4*), *SLIT*, *SOX2* and *TNFRSF21* [92, 218-226] were all significantly upregulated to different degrees after H3K27me3 reduction induced by EZH2 inhibition over three days. An upregulation was observed particularly for the two transcription factors, *POU5F1* and *SOX2*, showing a 15-fold and 12-fold expression compared to the DMSO control. The data demonstrate that small-molecule inhibition of EZH2, followed by profound H3K27me3 reduction, can lead to an increased expression of known repressed Polycomb target genes. This was shown before in different diffuse large B-cell lymphoma cell lines [92, 93]. The same group exhibited broad enrichment of H3K27me3 on the analyzed Polycomb regulated target genes using chromatin immunoprecipitation followed by sequencing (ChIP-seq), proving that the analyzed genes are Polycomb regulated genes truly marked by H3K27me3 [92].

However, the observed upregulation for the genes *HOXC8*, *IFI27*, *POU5F1* (*OCT-4*), *SLIT*, *SOX2* and *TNFRSF21* is less pronounced compared to the reported reactivation of target gene expression in sensitive cell lines. A reactivation of *TNFRSF21* was shown for one of the most sensitive DLBCL cell lines KARPAS-422, of 300-fold over the DMSO control [92]. The data revealed an upregulation of *TNFRSF21* 2.6-fold of the DMSO control. In this experiment, I used the WT EZH2 bearing, basal-B like cell line MDA-MB-231, which was not suppressed by EZH2 inhibitor treatment, despite profound H3K27me3 reduction. I analyzed genes which were Polycomb repressed and therefore expressed at very low levels. A temporary moderate upregulation (over ~10 days) may not be sufficient to bear biological relevance. As described in 4.2.2, different reports demonstrated that cell lines which were sensitive towards EZH2 inhibition (with regard to proliferation) displayed significant transcriptional effects while the insensitive cell lines displayed no or just minor effects on their transcription of Polycomb regulated genes [92, 227], possibly determined by functional epigenetic regulation of gene expression by different engaging epigenetic layers in parallel. Despite intense inhibitor induced H3K27me3 reduction, the genes *ADRB2*, *APOL3*, *CDH1* and *DAB2IP/AIP1* [92, 218-226] did not show an effect on their mRNA levels. All analyzed genes are described as

Polycomb regulated genes [92, 218-226]. Overall, an effect through H3K27me3 modulation on gene expression seem to strongly depend on the cellular context [92].

H3K27me3 is generally considered to be a hallmark of gene-silencing, because its genome-wide distribution coincides with Polycomb complexes [94, 228-230]. However, the mechanism by which H3K27me3 actually promotes gene silencing is still not known. As described in 1.4, one common suggestion is that H3K27me3 is a main determinant of recruiting PRC1 to chromatin, which catalyzes lysine 119 monoubiquitination of histone H2A (H2AK119Ub1) [65, 85]. However, recent findings challenge this view and there may be other possible consequences of nucleosomes being modified with H3K27me3. Any covalent histone modification may function as a docking site for a regulatory complex, or may directly alter nucleosome interactions *rev.* [75, 89]. In fact, there are studies suggesting that H3K27me3 might be not a cause but rather a secondary byproduct of gene-silencing (described in 1.4) [90].

4.3 Outlook

After this study was accomplished, the HCA assay was successfully miniaturized and automated from 384- to 1536-well plate format, in order to enable its realization in an HTS-capable format in the course of project work. Through this, we increased throughput and reduced consumable costs, enabling a complex and 96 hours long cellular assay being suitable for HTS, or specifically, high-content screening (HCS) of large scale screening libraries.

We investigated the assay performance, while testing the possibility of lowering the assay volume and adapting the assay protocol in terms of automation. We obtained an HTS-sufficient assay signal with applying ready-to-use cryopreserved cell culture samples, reducing the assay volume from 40 μ l to 6 μ l and completely automating the assay. For this purpose, we employed a fully robotic system containing incubators, several dispensers and pipettors for liquid handling, stacker and robotic arms for plate handling and a complex screening software. Due to the assay being an end-point measurement with fixed cells, the assay plates were able to be batch-processed within a stacker-equipped imaging platform, using the same exposure settings for the two laser channels throughout plate batches. The

imaging time required per plate was 20 minutes, enabling a processing of 72 1536-well plates per day, when only one imaging plate reader was used. Unattended, fully automated image acquisition allowed the imaging over 24 hours on seven days a week with a subsequent batch-processed image analysis considerably faster than the image acquisition.

However, miniaturizing the assay aroused several challenges e.g. evaporation due to the long assay procedure over several days or a higher proneness to errors. As a consequence of miniaturization and automation, the robustness of the assay lessened from $Z' = 0.67$ to $Z' = 0.32$, as shown in figure 6.1. The tool- and three structurally related EZH2 inhibitors were picked for comparison of the concentration response, obtained in MDA-MB-231 cells, after performing the HCA assay in each of the two plate formats. All four EZH2 inhibitors induced a dose-dependent H3K27me3 reduction to barely detectable levels at the highest concentration (10 μ M) using both formats for the assay, as shown in figure 6.2. For the 384-well plate format, cellular inhibitory activities generated IC₅₀ values of 7.11, 7.84, 30.01 and 95.9 nM for compound 2, compound 3, the tool inhibitor and compound 1, respectively. Due to miniaturization and automation, a general decrease in inhibitor potency (up to 9-fold shift in IC₅₀) with the same order in potency occurred using the 1536-well plate format.

To conclude, although inevitably compromising the assay performance, we obtained an assay signal which was sufficient for HTS and HCS, indicating a robust and high-quality EZH2 HCA assay. This assay is now used as inherent part of different screening projects comprising epigenetic chromatin modulation. It is likely to contribute to the identification of novel, cellular-active small-molecule inhibitors in the epigenetic field, thus, represents a benefit for epigenetic drug discovery, completing other currently used *in vitro* histone methyltransferase assay systems, as described in chapter 1.7.

5. Summary

Abstract

It has been shown that the inhibition of EZH2 is able to decrease global levels of the repressive mark H3K27me3, and thereby, reactivates silenced tumor suppressor genes such as *TNFRSF21*, *TXNIP* in sensitive cell lines. Thus, EZH2 forms an exciting potentially drug target in cancer. In this work, a HCA assay for the cell-based monitoring of small-molecule inhibition of EZH2 was established and applied. The phenotypic assay was established and validated by the use of siRNA and small-molecule inhibitors, confirming previous observations associated with global reduction in H3K9me2 after inhibition of G9a/GLP1 or global reduction in H3K27me3 after EZH2 inhibition or depletion. Based on siRNA-mediated knockdown analysis targeting different HKMTs, EZH2 was picked as the target enzyme of choice for an HCA assay development and a subsequent investigation of the functionality of induced H3K27me3 suppression. The assay consistency and reproducibility qualified the assay to be fit for screening of large compound libraries. Different EZH2 inhibitors were characterized and benchmarked distinguishing selective and cellular active EZH2 inhibition from indirect EZH2 inhibition with concomitant proliferative effect, or from inhibition with non-effectual cellular potency. Through simultaneously encompassing relevant cellular processes (e.g. nuclear morphology together with the measurement of the signal intensity of the site-specific histone modification antibody), inhibitor effects were monitored over broad inhibitor concentration ranges on the physiology of single cells. A loss of histone H3K27me3 loci triggered a symmetrical increase of the H3K27 acetylation mark. The demonstrated ability to analyze the genome-wide modification shift from H3K27me3 to H3K27ac as well as different histone marks in parallel (in form of multiplexed assays) formed appropriate dual-readouts to monitor small-molecule EZH2 inhibitors.

A loss in global H3K27me3, induced by EZH2 inhibition, was shown to comprise two distinct mechanisms: the inhibition of *de novo* methylation establishment, and a dynamic, replication independent, H3K27me3 turnover. Moreover, a measurable contribution of the two known H3K27-demethylases, UTX and JMJD3, on the turnover of H3K27me3 was demonstrated. Finally, full reversibility of the inhibitor treatment was observed, which was demonstrated at

the global level of H3K27me3 but also at the level of gene expression of a set of Polycomb regulated target genes (*HOXC8*, *IFI27*, *POU5F1* (*Oct-4*), *SLIT*, *SOX2* and *TNFRSF21*).

Altogether, the established EZH2 HCA assay enables a phenotypic and mechanistic characterization of compounds, possibly inhibiting EZH2, with high informational value (e.g. cellular downstream and morphological effects via multiplexing or heterogenic effects through the analysis of single nuclei). The assay demonstrated high quality and reproducibility sufficient for screening of large compound libraries. Complementing recent discoveries of selective tool inhibitors targeting EZH2, the assay moreover represents a useful tool for the cellular investigation of H3K27me3 and EZH2 biology.

Zusammenfassung

Die Inhibition von EZH2 führt zu einem Abfall an globalem H3K27me3 Level und gleichzeitig zu einer Reaktivierung von zuvor herunterregulierten Tumorsuppressorgenen. Daher stellen EZH2 und die repressive Modifikation H3K27me3 einen potentiellen Angriffspunkt in der Krebstherapie dar. In dieser Arbeit wurde ein *HCA Assay* zur Charakterisierung von chemischen Inhibitoren von EZH2 und anderen Histonmethyltransferasen etabliert und angewendet. Der phenotypische *Assay* wurde mittels Transfektion von siRNA und der Behandlung verschiedener chemischer Inhibitoren etabliert und validiert. Eine beschriebene Reduktion von H3K9me2 durch Inhibition von G9a/GLP1 und von H3K27me3 durch Inhibition oder Herunterregulation von EZH2 konnte gezeigt werden. Basierend auf einer siRNA Transfektionsanalyse verschiedener Histonmethyltransferasen wurde EZH2 als Enzym zur Entwicklung des *Assays* und einer anschließenden Untersuchung der Modulation von H3K27me3 durch EZH2 Inhibitoren ausgewählt. Die Robustheit und Reproduzierbarkeit des *Assays* ermöglichen dessen Eignung zum *Screening* großer Substanzbibliotheken. Verschiedene EZH2 Inhibitoren wurden mit Hilfe des *Assays* untersucht und gegenübergestellt. Inhibitor Effekte wurden auf der Einzelzelebene über einen breiten Konzentrationsbereich durch das gleichzeitige Ermitteln der Kernmorphologie und der Signalintensität modifikationsspezifischer Antikörper bestimmt. Eine Reduktion von H3K27me3 führte zu einer nahezu symmetrischen Zunahme an H3K27ac. Die parallele Quantifizierung der antagonistischen Modifikation H3K27ac und auch weiterer Histonmodifikationen stellen eine geeignete Dualauslesung des *Assays* dar.

Es konnte außerdem gezeigt werden, dass zum einen eine Inhibition einer *de novo* H3K27 Methylation und zum anderen ein dynamischer, zellzyklusunabhängiger H3K27me3 Umsatz eine Reduktion des globalen H3K27me3 Levels bewirkt. Ein messbarer Beitrag der H3K27-demethylasen, UTX und JMJD3, konnte am Umsatz von H3K27me3 aufgezeigt werden. Darüber hinaus konnte eine Reversibilität der H3K27me3 Modulation gezeigt werden, auf der globalen Ebene aber auch auf dem Level der Expression verschiedener Polycomb-regulierter Zielgene (*HOXC8*, *IFI27*, *POU5F1* (*Oct-4*), *SLIT*, *SOX2* und *TNFRSF21*).

Zusammenfassend ermöglicht der in dieser Arbeit etablierte EZH2 *HCA Assay* eine zelluläre und mechanistische Charakterisierung von möglichen EZH2 Inhibitoren. Die Robustheit und Reproduzierbarkeit des *Assays* ermöglicht ein *Screening* großer Substanzbibliotheken nach Molekülen mit EZH2-inhibierenden Eigenschaften. Zusammen mit den bereits entdeckten selektiven EZH2 Inhibitoren bietet der EZH2 *HCA Assay* außerdem eine geeignete und aussagekräftige Methode zur Untersuchung von H3K27me3 und EZH2 in der Zelle.

6. Appendix

6.1 Follow up: Miniaturization and automation for HTS purposes

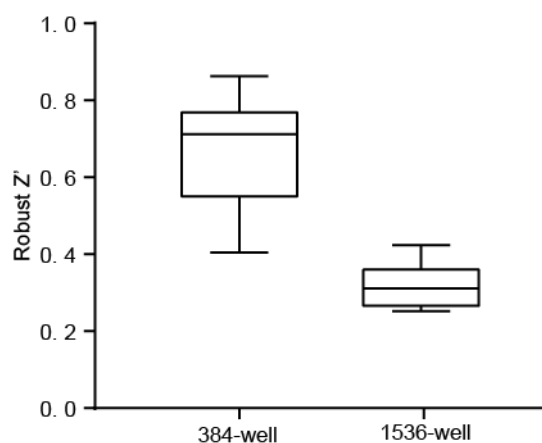


Figure 6.1: Assay robustness lessened through miniaturization and automation for HTS purposes. The robust Z'-factor was calculated for the assay performed in 384- and 1536-well plate format from 13 individual experiments. The average robustness of the assay lessened from $Z' = 0.67 \pm 0.13$ to $Z' = 0.32 \pm 0.05$ as a consequence of miniaturization and automation, transferring the assay from 384-well to 1536-well plate format.

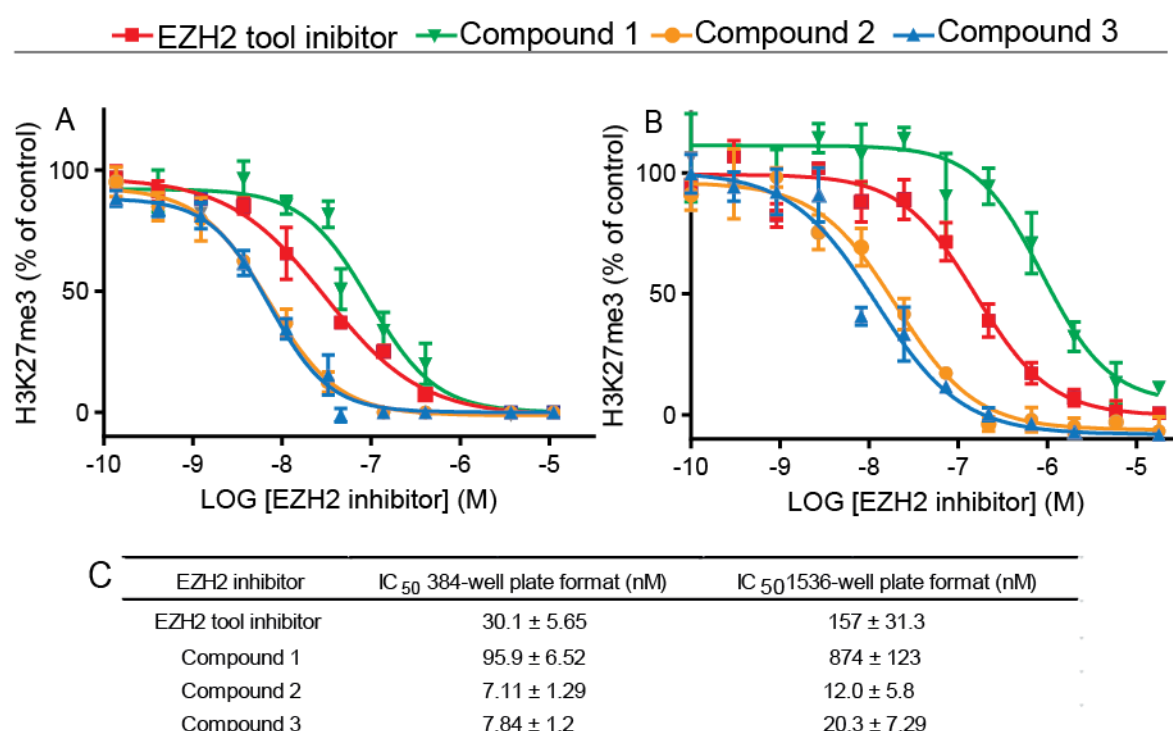


Figure 6.2: A general decrease in inhibitor potency occurred as a result of miniaturization and automation from 384-well plate format to 1536-well plate format with the same order in potency. (A,B) MDA-MB-231 cells were treated with varying concentrations of the EZH2 tool inhibitor and three structurally related EZH2 inhibitors over three days at 37°C in 5% CO₂ using 384-well plate format (A) or 1536-well plate format (B). The

graphs show the concentration response of the different EZH2 inhibitors in the relative H3K27me3 level at the inhibitor concentrations indicated. Responses are plotted as percentage of the DMSO control. Error bars show the standard deviation from three replicates. (C) Overview of the EZH2 inhibitor IC₅₀ values for 384-well plate format and 1536-well plate format. All IC₅₀ values are the average of at least three determinations.

6.2 Proliferation of the cell lines HeLa S3, MDA-MB-231 and MCF-7

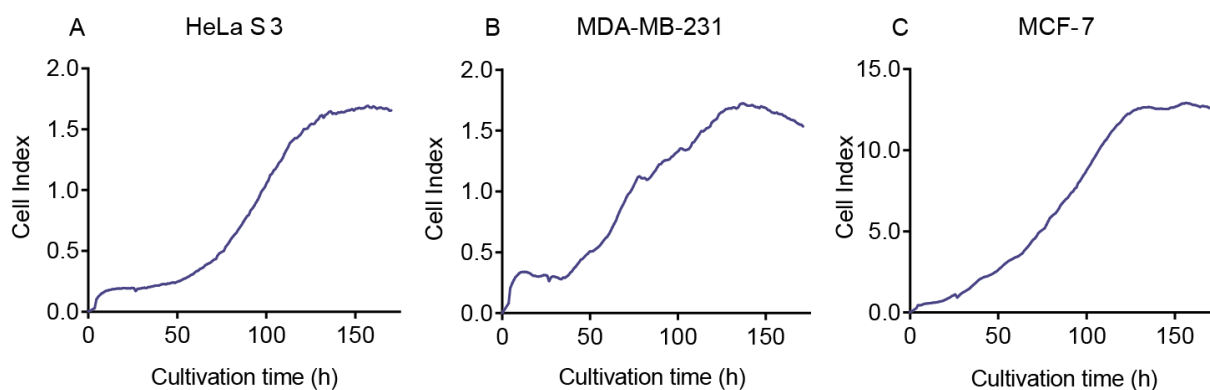


Figure 6.3: Proliferation of HeLa S3, MDA-MB-231 and MCF-7 under recommended culture conditions during a time range of 0 hours and 175 hours. Doubling times for HeLa S3 cells: 25 hours; for MDA-MB-231 cells: 24 hours and for MCF-7 cells: 34 hours.

6.3 Materials and reagents

6.3.1 Applied chemical compounds

The figures 6.4 and 6.5 display the chemical structures of the small-molecule inhibitors used in this work.

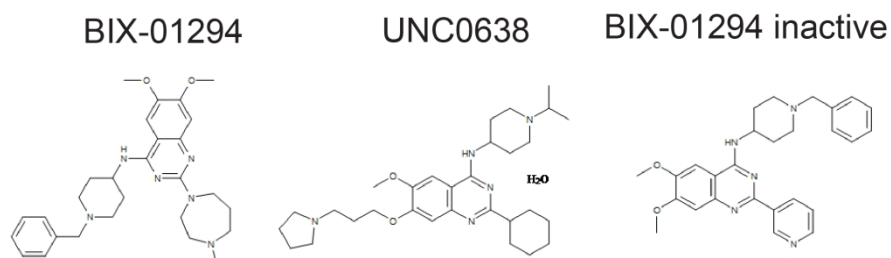


Figure 6.4: Chemical structures of utilized G9a and GLP1 inhibitors.

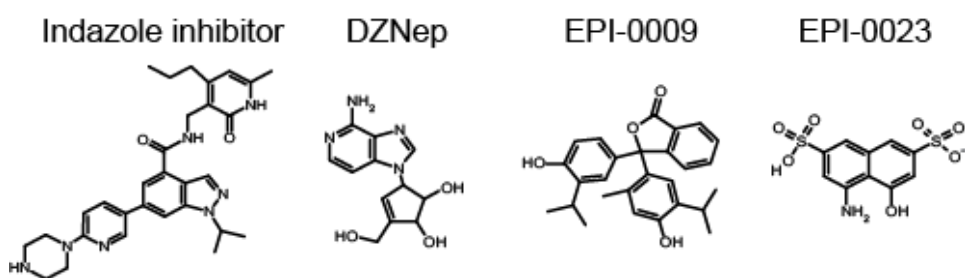


Figure 6.5: Chemical structures of utilized EZH2 inhibitors.

6.3.2 siRNA (small interfering RNA)

The following table displays the different siRNA nucleotides in alphabetical order of their target genes. The sequences of the different nucleotides can be obtained from the supplier websites with the help of the reference number.

Table 6.1: siRNA

Target	Name	Reference number	Supplier
DOT1L	Silencer® Select	S39012	Applied Biosystems®
	Cat. # 4392420	S39010	
	5 nmol	S39011	
EZH2	FlexiTube	SI00063959	Qiagen
	20 nmol	SI02665166	
MLL	Silencer® Select	S8819	Applied Biosystems®
	Cat. # 4392420	S8818	
	5 nmol		
MLL2	Silencer® Select	S15606	Applied Biosystems®
	Cat. # 4392420	S15605	
	5 nmol	S15604	
NSD1	Silencer® Select	S34631	Applied Biosystems®
	Cat. # 4392420	S34630	
	5 nmol	S34629	

SMYD2	Silencer [®] Select	S32470	Applied Biosystems [®]
	Cat. # 4392420	S32468	
	5 nmol	S32469	
UTX	siGenome	D-010140-02	Thermo Scientific Dharmacon
		D-010140-04	
JMJD3	siGenome	D-023013-02	Thermo Scientific Dharmacon
		D-023013-04	

6.3.3 TaqMan[®]-assays

The following table displays the TaqMan[®]-assays in alphabetical order of their target genes. The sequences can be obtained from the supplier websites with the help of the reference number.

Table 6.2: TaqMan[®]-assays

Target	Reference number	Supplier
DOT1L	Hs01588547_m1	Applied Biosystems [®]
EZH2	Hs00544833_m1	Applied Biosystems [®]
JMJD3	Hs00996325_g1	Applied Biosystems [®]
MLL	Hs00610538_m1	Applied Biosystems [®]
MLL2	Hs00231606_m1	Applied Biosystems [®]
NSD1	Hs00328315_m1	Applied Biosystems [®]
SMYD2	Hs00220210_m1	Applied Biosystems [®]
UTX	Hs00958902_m1	Applied Biosystems [®]
18S	Hs03003631_g1	Applied Biosystems [®]

6.3.4 Antibodies

Table 6.3: Antibodies

Antibody	Dilution	Supplier	Isotype	Application
<i>Primary antibodies</i>				
H3K27me3	1:1000, 1:250	Cell Signaling #9733	Rabbit	WB, IF
H3K9me2	1:100	Abcam #ab1220	Mouse	IF
H3K4me3	1:250	Millipore #04-745	Rabbit	IF
H3K36me2	1:100	Active Motif #39255	Rabbit	IF
H3K27ac	1:200	Cell Signaling #8173	Rabbit	IF
H3K79me2	1:200	Abcam #ab3594	Rabbit	IF
H3	1:1000, 1:100	Abcam #ab70550	Rabbit	WB, IF
EZH2	1:1000, 1:150	Cell Signaling #3147, 5246	Mouse, Rabbit	WB, IF
GAPDH	1:1000	Sigma-Aldrich #G8795	Mouse	IF
<i>Secondary antibodies</i>				
DyLight™649, goat anti-rabbit	1:100	Jackson Immuno Research #111- 496-045	goat	IF
DyLight™488, goat anti-rabbit	1:100	Jackson Immuno Research #111- 486-045	goat	IF
DyLight™649, goat anti-mouse	1:100	Jackson Immuno Research #115- 496-062	goat	IF
DyLight™488, goat anti-mouse	1:100	Jackson Immuno Research #115- 486-062	goat	IF
Alexa goat anti	1:1000	Invitrogen	goat	WB

rabbit, 680 nm		#A21109		
Alexa goat anti mouse, 680 nm	1:1000	Invitrogen #A21058	goat	WB

6.3.5 Chemicals and reagents

Table 6.4: Chemicals and reagents

Chemicals and reagents	Supplier
BSA (Bovine Serum Albumin)	Sigma-Aldrich
Complete Protease Inhibitor Cocktail Tablets	Roche
ChromPure Goat IgG, whole molecule	Jackson Immuno Research
Dulbecco's Phosphate-Buffered Saline (DPBS 10 x) without Ca^{2+} , Mg^{2+}	Biochrom
Dimethyl Sulfoxide (DMSO)	Sigma-Aldrich
Estradiol	Sigma-Aldrich
Ethanol, absolut $\geq 99.8\%$ (GC)	Sigma-Aldrich
FCS (Fetal calf serum)	PAA Laboratories GmbH
Glycerol	Merck
Ham's-F12, w/o L-Glutamin	PAA Laboratories GmbH
Hoechst 33342	Molecular Probes
HiPerfect Transfection Reagent	Qiagen
Hoechst 33342	Molecular Probes, Life Technologies
Isopropanol, 5l	Fisher Scientific
Insulin	Sigma-Aldrich
L-Glutamin	Gibco
NuPAGE MES SDS Running Buffer (20 x)	Life Technologies
NuPAGE MOPS SDS Running Buffer (20 x)	Life Technologies

NuPAGE LDS Sample Buffer (4x)	Invitrogen, Technologies	Life
NuPAGE Sample Reducing Agent (10x)	Invitrogen, Technologies	Life
Odyssey Protein Molecular Weight Marker	Li-Cor	
Opti-MEM® I Reduced Serum Media without phenol red	Life Technologies	
Precision Plus Protein Standards	BIO-RAD	
Penicillin / Streptomycin	Gibco	
Paraformaldehyde, EM Grade, Purified	Electron Microscopy Sciences	
PhosStop Tablets	Roche	
Ponceau S solution	Sigma-Aldrich	
5 x siRNA Universal buffer	Dharmacon	
Tris Buffered Saline (TBS 10 x)	Sigma-Aldrich	
TaqMan Universal PCR Master Mix. No AmpErase UNG	Applied Biosystems	
Triton X-100	Sigma-Aldrich	
UltraPure Distilled Water	Invitrogen	

6.3.6 Kits

Table 6.5: Kits

Kit	Supplier
Click-iT® EdU Alexa Fluor® 488 Imaging Kit	Life Technologies
High Capacity RNA-to-cDNA Master Mix	Applied Biosystems
Pierce BCA protein assay kit	ThermoScientific
RNeasy Mini Kit	Qiagen
RNase free DNase I set	Qiagen

6.3.7 Materials

Table 6.6: Materials

Materials	Supplier
Cell Culture flasks	Costar
Microtiter plate 384-well (cell carrier)	Greiner
Microtiter plate 384-well (μ clear)	Greiner
NuPAGE [®] Novex [®] 4-12% Bis-Tris protein gel	Life Technologies
Pipette tips	Thermo Scientific, Eppendorf
Reagent tubes (15, 50 ml)	Costar
Reagent tubes (0.5, 1.5, 2.0 ml)	Eppendorf
Serological pipettes (1, 2, 5, 25, 50 ml)	Costar

6.3.8 Devices

Table 6.7: Devices

Devices	Supplier
Casy Modell TTC	Schärfe Sytem
Centrifuge Bio Fuge fresco	Heraeus
Centrifuge RC5C	Sorvall
CRS Catalyst-5 robot	Thermo Electron Corporation
Cybi TM -Well	CyBio
Electrophoresis power supply	Consort
Electronical multi-channel pipettes	Thermo Scientific, Eppendorf
Incubators	Heraeus

iBlot® Dry Blotting System	Life Technologies
Mastercycler	Eppendorf
Manual single channel pipettes	Eppendorf
Multidrop™ Combi	Thermo Scientific
Odyssey Infrared Imager	Li-Cor Biosciences
Opera™ Reader	Perkin Elmer
Plate shaker	Ecotron
QIAcube	Qiagen
Shaker, Duomax 2030	Heidolph
UV/VIS-spektrometer	Perkin Elmer, Nanodrop
Water bath	Julabo
7900HT Fast Real-Time PCR System	Applied Biosystems

7. Abbreviations

ADME	Absorption, distribution, metabolism, and excretion
ANOVA	Analysis of variance
ATCC	American Type Culture Collection
BacMam	Baculovirus mediated gene transduction of mammalian cells
BSA	bovine serum albumin
bp	Base pairs
cDNA	Complementary DNA
CHIP	DNA microarrays
ChIP	Chromatin immunoprecipitation
DELFI [®]	Dissociation-enhanced lanthanide fluorescence immunoassay
DLBCL	diffuse large B-cell lymphoma
DMSO	Dimethyl sulfoxide
DNA	Deoxyribonucleic acid
DOT1L	DOT1-like
DPBS	Dulbecco's Phosphate-Buffered Saline
DSMZ	Deutsche Sammlung von Mikroorganismen und Zellkulturen
DZNep	3-deazaneplanocin A
EdU	5-ethynyl-2'-deoxyuridine
EHMT1/2	Euchromatin histone methyltransferase 1/2
ELISA	Enzyme-linked immunosorbent assay
EZH2	Enhancer of zeste homolog 2
EED	Embryonic ectoderm development
FCS	Fetal calf serum
FDA	Food and drug administration
GPCRs	G-protein-coupled receptors

HATs	Histone acetylases
HDACs	Histone deacetylases
HCA	High-Content Analysis
HCS	High-Content Screening
HMTs	Histone methyltransferases
HKMTs	Histone lysine methyltransferases
HRMTs	Histone arginine methyltransferases
HTS	High-throughput screening
H3	Histone H3
H3K27me3	Histone H3 lysine 27 trimethylation
KDMs	Histone lysine demethylases
IgG	Immunoglobulin G
JMJD3	Jumonji domain-containing protein 3
lncRNA	long noncoding RNA
LSD-1	Flavin-dependent monoamine oxidase lysine-specific demethylase
MLL	Mixed-lineage leukemia proteins
mRNA	Messenger RNA
nl, µl, ml,	Nano, micro, milli litre
nm	Nano meter
NSD	Nuclear receptor binding SET domain family
PBS	Dulbecco's phosphate-buffered saline
PcG	Polycomb-group
PCR	Polymerase chain reaction
qRT-PCR	Quantitative real-time PCR
PFA	Paraformaldehyde
Pg, ng, µg, mg, g	Pico, nano, micro, milli, gram

PPTases	Histone kinases and phosphatases
PRC1/2	Polycomb repressive complex 1/2
PTMs	Posttranslational modifications
RNA	Ribonucleic acid
ROI	Region of interest
Rpm	Revolutions per minute
RT	Room temperature
S, min, h	Second, minute, hour
SAH	S-adenosyl-L-homocysteine
SAM	S-adenosyl-methionine
SAR	Structure-activity relationship
siRNA	Small interfering RNA
SMYD2	SET and MYND domain-containing protein 2
SUZ12	Polycomb repressive complex 2 subunit
TBS	Tris Buffered Saline
TR-FRET	Time resolved fluorescence resonance energy transfer
Tyr641	Tyrosine 641
UTX	Ubiquitously transcribed tetratricopeptide repeat
UV/VIS	Ultraviolet/Visible
WT	Wild type

8. Figures and tables

Figures

Figure 1.1: Gene silencing: a model for a collaboration of PRC2 and HDAC

Figure 1.2: Model for the 'self- propagation' mechanism of PRC2: Transmission of H3K27me3 through the cell cycle.

Figure 2.1: The standardized image-analysis module ("Count Nuclei") provided by the image analysis software MetaXpress®.

Figure 2.2: Algorithm I: Nuclei segmentation and quantification of histone methylation mark.

Figure 2.3: Algorithm II (subsequently to algorithm I): Scoring for cells with low enzyme expression, quantification of histone methylation mark and export to a spread sheet.

Figure 2.4: The standardized image-analysis module ("Cell Cycle") provided by the image analysis software MetaXpress®

Figure 2.5: Algorithm III, part 1: Generating nuclei masks based on cell cycle phases and superimpose with images showing the histone modification-specific antibody signal.

Figure 2.6: Algorithm III, part 2: Quantify the integrated signal intensities of every nucleus in distinctive cell cycle stage and export to a spread sheet.

Figure 3.1: Schematic image analysis for phenotypically quantifying cellular EZH2 and H3K27me3 using HCA.

Figure 3.2: Phenotypic quantification revealed different effects on global levels of respective histone methylation marks after siRNA-mediated knockdown of six selected HKMTs.

Figure 3.3: Reduced mRNA levels were observed for the six HKMTs, targeted in a time course using siRNA.

Figure 3.4: Representative confocal immunofluorescence images presenting an increasing suppression of global H3K27me3 with time, induced by a knockdown of EZH2 using siRNA.

Figure 3.5: A quantification of EZH2 and global H3K27me3 shows that the methylation mark was directly suppressed in a time depending manner, induced by siRNA-mediated knockdown of EZH2.

Figure 3.6: The G9a and GLP 1 inhibitors UNC0638 and BIX-01294 demonstrated distinguished cellular inhibitory activity on H3K9me2.

Figure 3.7: No dose-dependent H3K27me3 suppression or cell number reduction was observed with DMSO percentages up to 0.5% under assay conditions, using a 384-well plate format.

Figure 3.8: EZH2 inhibition using the selective tool inhibitor induced a profound demethylation of H3K27-me3, distinctively separated from cytotoxicity in the cell lines HeLa S3, MDA-MB-231 and MCF7.

Figure 3.9: Selective EZH2 inhibition using the tool inhibitor did not alter several histone methylation marks except for H3K27me3 while the non-selective inhibitor DZNep induced a dose-dependent reduction in H3K27me3 and H3K4me3.

Figure 3.10: Z'-factor determination, in order to evaluate the assay quality, generated a value of 0.7 (qualified for screening [18]) for modulating H3K27me3 by EZH2 inhibition in a 384-well-plate format.

Figure 3.11: EZH2 inhibitors demonstrated distinguished cellular inhibitory activity on H3K27me3 and proliferative effects.

Figure 3.12: Small-molecule EZH2 inhibition induced a progressive H3K27me3 suppression over three days accompanied by a genome-wide modification switch from H3K27me3 to H3K27ac in MDA-MB-231 cells.

Figure 3.13: Representative confocal immunofluorescence images display a genome-wide modification switch from H3K27me3 to H3K27ac induced by small-molecule EZH2 inhibition in MDA-MB-231 cells.

Figure 3.14: EZH2 inhibition induces a genome-wide modification switch from H3K27me3 to H3K27ac in HeLa S3- and MCF7 cells.

Figure 3.15: EZH2 protein levels vary for non-treated MCF7-, HeLa S3- and MDA-MB-231 cells, as determined in western blot analysis.

Figure 3.16: An EZH2 inhibition of six hours is sufficient to induce a reduction of H3K27me3, reaching a maximal measureable H3K27me3 suppression at day three.

Figure 3.17: Small-molecule EZH2 inhibition reveals a dynamic, cell cycle independent H3K27me3 fraction.

Figure 3.18: A knockdown of the demethylases UTX and JMJD3 significantly reduced EZH2 knockdown effects on methylation.

Figure 3.19: Representative confocal immunofluorescence images presenting a reduced EZH2 knockdown effect on methylation due to a parallel knockdown of the demethylases UTX or JMJD3, respectively.

Figure 3.20: Reduced mRNA levels were observed at two days after combinational siRNA knockdown comprising EZH2 with UTX or EZH2 with JMJD3.

Figure 3.21: A western blot analysis demonstrates reduced EZH2 protein to comparable levels for all paralleled knockdown conditions quantified in figure 3.18.

Figure 3.22: H3K27me3 restores after profound reduction, induced by previous EZH2 inhibition.

Figure 3.23: Representative confocal immunofluorescence images of H3K27me3 being restored after strong reduction induced by EZH2 inhibition.

Figure 3.24: H3K27me3 reduction and recovery occurred homogenously for every cell of the inhibitor treated population, with marginal effects on the cell cycle.

Figure 3.25: H3K27me3 reduction was paralleled with an upregulation of the expression of the polycomb regulated genes HOXC8, IFI27, POU5F1 (Oct-4), SLIT, SOX2 and TNFRSF21, while a subsequent H3K27me3 recovery occurred together with repression of these genes.

Figure 3.26: Reduced mRNA levels were observed at two days after combinational siRNA knockdown comprising EZH2 with UTX or EZH2 with JMJD3.

Figure 6.1: Assay robustness lessened through miniaturization and automation for HTS purposes.

Figure 6.2: A general decrease in inhibitor potency occurred as a result of miniaturization and automation from 384-well plate format to 1536-well plate format with the same order in potency.

Figure 6.3: Proliferation of HeLa S3, MDA-MB-231 and MCF-7 under recommended culture conditions during a time range of 0 hours and 175 hours.

Figure 6.4: Chemical structures of utilized G9a and GLP1 inhibitors.

Figure 6.5: Chemical structures of utilized EZH2 inhibitors.

Tables

Table 1.1: Selected HKMTs and their disease indications:

Table 1.2: Small-molecule inhibitors of selected HKMTs:

Table 2.1: Working solutions immunofluorescence:

Table 2.2: Click-iT[®] reaction solution:

Table 2.3: cDNA synthesis preparation:

Table 2.4: qRT-PCR sample preparation:

Table 3.1: Determination of Z'-factors and S/B values for a set of six discrete 384-well-plates.

Table 6.1: siRNA

Table 6.2: TaqMan[®] -assays

Table 6.3: Antibodies

Table 6.4: Chemicals and reagents

Table 6.5: Kits

Table 6.6: Materials

Table 6.7: Devices

9. References

1. Bernt, K.M., et al., *MLL-rearranged leukemia is dependent on aberrant H3K79 methylation by DOT1L*. Cancer Cell, 2011. **20**(1): p. 66-78.
2. Daigle, S.R., et al., *Potent inhibition of DOT1L as treatment of MLL-fusion leukemia*. Blood, 2013. **122**(6): p. 1017-25.
3. Sneeringer, C.J., et al., *Coordinated activities of wild-type plus mutant EZH2 drive tumor-associated hypertrimethylation of lysine 27 on histone H3 (H3K27) in human B-cell lymphomas*. Proc Natl Acad Sci U S A, 2010. **107**(49): p. 20980-5.
4. Morin, R.D., et al., *Somatic mutations altering EZH2 (Tyr641) in follicular and diffuse large B-cell lymphomas of germinal-center origin*. Nat Genet, 2010. **42**(2): p. 181-5.
5. He, A., et al., *PRC2 directly methylates GATA4 and represses its transcriptional activity*. Genes Dev, 2012. **26**(1): p. 37-42.
6. Varambally, S., et al., *The polycomb group protein EZH2 is involved in progression of prostate cancer*. Nature, 2002. **419**(6907): p. 624-9.
7. Kleer, C.G., et al., *EZH2 is a marker of aggressive breast cancer and promotes neoplastic transformation of breast epithelial cells*. Proc Natl Acad Sci U S A, 2003. **100**(20): p. 11606-11.
8. Vedadi, M., et al., *A chemical probe selectively inhibits G9a and GLP methyltransferase activity in cells*. Nat Chem Biol, 2011. **7**(8): p. 566-74.
9. Yuan, Y., et al., *A small-molecule probe of the histone methyltransferase G9a induces cellular senescence in pancreatic adenocarcinoma*. ACS Chem Biol, 2012. **7**(7): p. 1152-7.
10. Hess, J.L., *MLL: a histone methyltransferase disrupted in leukemia*. Trends Mol Med, 2004. **10**(10): p. 500-7.
11. Krivtsov, A.V. and S.A. Armstrong, *MLL translocations, histone modifications and leukaemia stem-cell development*. Nat Rev Cancer, 2007. **7**(11): p. 823-33.
12. Schneider, R., A.J. Bannister, and T. Kouzarides, *Unsafe SETs: histone lysine methyltransferases and cancer*. Trends Biochem Sci, 2002. **27**(8): p. 396-402.
13. Wang, G.G., et al., *NUP98-NSD1 links H3K36 methylation to Hox-A gene activation and leukaemogenesis*. Nat Cell Biol, 2007. **9**(7): p. 804-12.
14. Zhao, F., et al., *Role of triptolide in cell proliferation, cell cycle arrest, apoptosis and histone methylation in multiple myeloma U266 cells*. Eur J Pharmacol, 2010. **646**(1-3): p. 1-11.

15. Rosati, R., et al., *NUP98 is fused to the NSD3 gene in acute myeloid leukemia associated with t(8;11)(p11.2;p15)*. Blood, 2002. **99**(10): p. 3857-60.
16. Rayasam, G.V., et al., *NSD1 is essential for early post-implantation development and has a catalytically active SET domain*. EMBO J, 2003. **22**(12): p. 3153-63.
17. Walter, M.J., et al., *Acquired copy number alterations in adult acute myeloid leukemia genomes*. Proc Natl Acad Sci U S A, 2009. **106**(31): p. 12950-5.
18. Zhang, J.H., T.D. Chung, and K.R. Oldenburg, *A Simple Statistical Parameter for Use in Evaluation and Validation of High Throughput Screening Assays*. J Biomol Screen, 1999. **4**(2): p. 67-73.
19. Komatsu, S., et al., *Overexpression of SMYD2 relates to tumor cell proliferation and malignant outcome of esophageal squamous cell carcinoma*. Carcinogenesis, 2009. **30**(7): p. 1139-46.
20. Ferguson, A.D., et al., *Structural basis of substrate methylation and inhibition of SMYD2*. Structure, 2011. **19**(9): p. 1262-73.
21. Helin, K. and D. Dhanak, *Chromatin proteins and modifications as drug targets*. Nature, 2013. **502**(7472): p. 480-8.
22. Allis, C.D., Jenuwein, T., Reinberg, D., *Epigenetics*. 2007: Cold Spring Harbor Laboratory Press
23. Waddington, C.H., *The Strategy of the Genes, a Discussion of Some Aspects of Theoretical Biology* 1957: G. Allen and Unwin
24. Lund, K., P.D. Adams, and M. Copland, *EZH2 in normal and malignant hematopoiesis*. Leukemia, 2014. **28**(1): p. 44-9.
25. Luger, K., et al., *Crystal structure of the nucleosome core particle at 2.8 Å resolution*. Nature, 1997. **389**(6648): p. 251-60.
26. McGhee, J.D. and G. Felsenfeld, *Nucleosome structure*. Annu Rev Biochem, 1980. **49**: p. 1115-56.
27. Kornberg, R.D., *Structure of chromatin*. Annu Rev Biochem, 1977. **46**: p. 931-54.
28. Owen-Hughes, T., *Colworth memorial lecture. Pathways for remodelling chromatin*. Biochem Soc Trans, 2003. **31**(Pt 5): p. 893-905.
29. Saha, A., J. Wittmeyer, and B.R. Cairns, *Chromatin remodelling: the industrial revolution of DNA around histones*. Nat Rev Mol Cell Biol, 2006. **7**(6): p. 437-47.
30. Cheung, P., C.D. Allis, and P. Sassone-Corsi, *Signaling to chromatin through histone modifications*. Cell, 2000. **103**(2): p. 263-71.

31. Jenuwein, T. and C.D. Allis, *Translating the histone code*. Science, 2001. **293**(5532): p. 1074-80.
32. Strahl, B.D. and C.D. Allis, *The language of covalent histone modifications*. Nature, 2000. **403**(6765): p. 41-5.
33. Cosgrove, M.S., *Histone proteomics and the epigenetic regulation of nucleosome mobility*. Expert Rev Proteomics, 2007. **4**(4): p. 465-78.
34. Campos, E.I. and D. Reinberg, *Histones: annotating chromatin*. Annu Rev Genet, 2009. **43**: p. 559-99.
35. Sterner, D.E. and S.L. Berger, *Acetylation of histones and transcription-related factors*. Microbiol Mol Biol Rev, 2000. **64**(2): p. 435-59.
36. Chuikov, S., et al., *Regulation of p53 activity through lysine methylation*. Nature, 2004. **432**(7015): p. 353-60.
37. Lachner, M., R.J. O'Sullivan, and T. Jenuwein, *An epigenetic road map for histone lysine methylation*. J Cell Sci, 2003. **116**(Pt 11): p. 2117-24.
38. Tan, J.Z., et al., *EZH2: biology, disease, and structure-based drug discovery*. Acta Pharmacol Sin, 2014. **35**(2): p. 161-74.
39. Albert, M. and K. Helin, *Histone methyltransferases in cancer*. Semin Cell Dev Biol, 2010. **21**(2): p. 209-20.
40. Pan, G., et al., *Whole-genome analysis of histone H3 lysine 4 and lysine 27 methylation in human embryonic stem cells*. Cell Stem Cell, 2007. **1**(3): p. 299-312.
41. Bernstein, B.E., et al., *A bivalent chromatin structure marks key developmental genes in embryonic stem cells*. Cell, 2006. **125**(2): p. 315-26.
42. Zhang, Y. and D. Reinberg, *Transcription regulation by histone methylation: interplay between different covalent modifications of the core histone tails*. Genes Dev, 2001. **15**(18): p. 2343-60.
43. Martin, C. and Y. Zhang, *The diverse functions of histone lysine methylation*. Nat Rev Mol Cell Biol, 2005. **6**(11): p. 838-49.
44. Benevolenskaya, E.V., *Histone H3K4 demethylases are essential in development and differentiation*. Biochem Cell Biol, 2007. **85**(4): p. 435-43.
45. Steger, D.J., et al., *DOT1L/KMT4 recruitment and H3K79 methylation are ubiquitously coupled with gene transcription in mammalian cells*. Mol Cell Biol, 2008. **28**(8): p. 2825-39.

46. Barski, A., et al., *High-resolution profiling of histone methylations in the human genome*. Cell, 2007. **129**(4): p. 823-37.
47. Zee, B.M., et al., *In vivo residue-specific histone methylation dynamics*. J Biol Chem, 2010. **285**(5): p. 3341-50.
48. Byvoet, P., *In vivo turnover and distribution of radio-N-methyl in arginine-rich histones from rat tissues*. Arch Biochem Biophys, 1972. **152**(2): p. 887-8.
49. Duerre, J.A. and C.T. Lee, *In vivo methylation and turnover of rat brain histones*. J Neurochem, 1974. **23**(3): p. 541-7.
50. Lachner, M., et al., *Methylation of histone H3 lysine 9 creates a binding site for HP1 proteins*. Nature, 2001. **410**(6824): p. 116-20.
51. Shi, Y., et al., *Histone demethylation mediated by the nuclear amine oxidase homolog LSD1*. Cell, 2004. **119**(7): p. 941-53.
52. Tsukada, Y., et al., *Histone demethylation by a family of JmjC domain-containing proteins*. Nature, 2006. **439**(7078): p. 811-6.
53. Yamane, K., et al., *JHDM2A, a JmjC-containing H3K9 demethylase, facilitates transcription activation by androgen receptor*. Cell, 2006. **125**(3): p. 483-95.
54. Metzger, E., et al., *LSD1 demethylates repressive histone marks to promote androgen-receptor-dependent transcription*. Nature, 2005. **437**(7057): p. 436-9.
55. Kooistra, S.M. and K. Helin, *Molecular mechanisms and potential functions of histone demethylases*. Nat Rev Mol Cell Biol, 2012. **13**(5): p. 297-311.
56. Mosammamarast, N. and Y. Shi, *Reversal of histone methylation: biochemical and molecular mechanisms of histone demethylases*. Annu Rev Biochem, 2010. **79**: p. 155-79.
57. Shi, Y. and J.R. Whetstine, *Dynamic regulation of histone lysine methylation by demethylases*. Mol Cell, 2007. **25**(1): p. 1-14.
58. Klose, R.J., et al., *Demethylation of histone H3K36 and H3K9 by Rph1: a vestige of an H3K9 methylation system in Saccharomyces cerevisiae?* Mol Cell Biol, 2007. **27**(11): p. 3951-61.
59. Lan, F., et al., *A histone H3 lysine 27 demethylase regulates animal posterior development*. Nature, 2007. **449**(7163): p. 689-94.
60. Turner, B.M., *Histone acetylation and an epigenetic code*. Bioessays, 2000. **22**(9): p. 836-45.

61. Lan, F., et al., *Recognition of unmethylated histone H3 lysine 4 links BHC80 to LSD1-mediated gene repression*. Nature, 2007. **448**(7154): p. 718-22.
62. Jones, D.O., I.G. Cowell, and P.B. Singh, *Mammalian chromodomain proteins: their role in genome organisation and expression*. Bioessays, 2000. **22**(2): p. 124-37.
63. Pek, J.W., A. Anand, and T. Kai, *Tudor domain proteins in development*. Development, 2012. **139**(13): p. 2255-66.
64. Berger, S.L., *Histone modifications in transcriptional regulation*. Curr Opin Genet Dev, 2002. **12**(2): p. 142-8.
65. Fischle, W., et al., *Molecular basis for the discrimination of repressive methyl-lysine marks in histone H3 by Polycomb and HP1 chromodomains*. Genes Dev, 2003. **17**(15): p. 1870-81.
66. Henikoff, S., *Histone modifications: combinatorial complexity or cumulative simplicity?* Proc Natl Acad Sci U S A, 2005. **102**(15): p. 5308-9.
67. Schreiber, S.L. and B.E. Bernstein, *Signaling network model of chromatin*. Cell, 2002. **111**(6): p. 771-8.
68. Rando, O.J., *Combinatorial complexity in chromatin structure and function: revisiting the histone code*. Curr Opin Genet Dev, 2012. **22**(2): p. 148-55.
69. Santos-Rosa, H., et al., *Methylation of H3 lysine 4 at euchromatin promotes Sir3p association with heterochromatin*. J Biol Chem, 2004. **279**(46): p. 47506-12.
70. Bernstein, B.E., et al., *Genomic maps and comparative analysis of histone modifications in human and mouse*. Cell, 2005. **120**(2): p. 169-81.
71. Lippman, Z., et al., *Role of transposable elements in heterochromatin and epigenetic control*. Nature, 2004. **430**(6998): p. 471-6.
72. Martens, J.H., et al., *The profile of repeat-associated histone lysine methylation states in the mouse epigenome*. Embo j, 2005. **24**(4): p. 800-12.
73. Ringrose, L., H. Ehret, and R. Paro, *Distinct Contributions of Histone H3 Lysine 9 and 27 Methylation to Locus-Specific Stability of Polycomb Complexes*. Molecular Cell, 2004. **16**(4): p. 641-653.
74. Lewis, E.B., *A gene complex controlling segmentation in Drosophila*. Nature, 1978. **276**(5688): p. 565-70.
75. Simon, J.A. and R.E. Kingston, *Occupying chromatin: polycomb mechanisms for getting to genomic targets, stopping transcriptional traffic, and staying put*. Mol Cell, 2013. **49**(5): p. 808-24.

76. Francis, N.J., et al., *Polycomb proteins remain bound to chromatin and DNA during DNA replication in vitro*. Cell, 2009. **137**(1): p. 110-22.
77. Kennison, J.A., *The Polycomb and trithorax group proteins of Drosophila: trans-regulators of homeotic gene function*. Annu Rev Genet, 1995. **29**: p. 289-303.
78. Morey, L. and K. Helin, *Polycomb group protein-mediated repression of transcription*. Trends Biochem Sci, 2010. **35**(6): p. 323-32.
79. Pasini, D., et al., *Suz12 is essential for mouse development and for EZH2 histone methyltransferase activity*. Embo j, 2004. **23**(20): p. 4061-71.
80. He, G.P., S. Kim, and H.S. Ro, *Cloning and characterization of a novel zinc finger transcriptional repressor. A direct role of the zinc finger motif in repression*. J Biol Chem, 1999. **274**(21): p. 14678-84.
81. Cao, R., et al., *Role of histone H3 lysine 27 methylation in Polycomb-group silencing*. Science, 2002. **298**(5595): p. 1039-43.
82. Kuzmichev, A., et al., *Different EZH2-containing complexes target methylation of histone H1 or nucleosomal histone H3*. Mol Cell, 2004. **14**(2): p. 183-93.
83. Tie, F., et al., *CBP-mediated acetylation of histone H3 lysine 27 antagonizes Drosophila Polycomb silencing*. Development, 2009. **136**(18): p. 3131-41.
84. Cao, R., Y. Tsukada, and Y. Zhang, *Role of Bmi-1 and Ring1A in H2A ubiquitylation and Hox gene silencing*. Mol Cell, 2005. **20**(6): p. 845-54.
85. Min, J., Y. Zhang, and R.M. Xu, *Structural basis for specific binding of Polycomb chromodomain to histone H3 methylated at Lys 27*. Genes Dev, 2003. **17**(15): p. 1823-8.
86. Wang, H., et al., *Role of histone H2A ubiquitination in Polycomb silencing*. Nature, 2004. **431**(7010): p. 873-8.
87. Endoh, M., et al., *Histone H2A mono-ubiquitination is a crucial step to mediate PRC1-dependent repression of developmental genes to maintain ES cell identity*. PLoS Genet, 2012. **8**(7): p. e1002774.
88. Vire, E., et al., *The Polycomb group protein EZH2 directly controls DNA methylation*. Nature, 2006. **439**(7078): p. 871-4.
89. Simon, J.A. and R.E. Kingston, *Mechanisms of polycomb gene silencing: knowns and unknowns*. Nat Rev Mol Cell Biol, 2009. **10**(10): p. 697-708.
90. Yuan, W., et al., *Dense chromatin activates Polycomb repressive complex 2 to regulate H3 lysine 27 methylation*. Science, 2012. **337**(6097): p. 971-5.

91. Henikoff, S. and A. Shilatifard, *Histone modification: cause or cog?* Trends Genet, 2011. **27**(10): p. 389-96.
92. McCabe, M.T., et al., *EZH2 inhibition as a therapeutic strategy for lymphoma with EZH2-activating mutations*. Nature, 2012. **492**(7427): p. 108-12.
93. Knutson, S.K., et al., *A selective inhibitor of EZH2 blocks H3K27 methylation and kills mutant lymphoma cells*. Nat Chem Biol, 2012. **8**(11): p. 890-6.
94. Margueron, R. and D. Reinberg, *The Polycomb complex PRC2 and its mark in life*. Nature, 2011. **469**(7330): p. 343-9.
95. Agger, K., et al., *UTX and JMJD3 are histone H3K27 demethylases involved in HOX gene regulation and development*. Nature, 2007. **449**(7163): p. 731-4.
96. De Santa, F., et al., *The histone H3 lysine-27 demethylase Jmjd3 links inflammation to inhibition of polycomb-mediated gene silencing*. Cell, 2007. **130**(6): p. 1083-94.
97. Hong, S., et al., *Identification of JmjC domain-containing UTX and JMJD3 as histone H3 lysine 27 demethylases*. Proc Natl Acad Sci U S A, 2007. **104**(47): p. 18439-44.
98. Lee, M.G., et al., *Demethylation of H3K27 regulates polycomb recruitment and H2A ubiquitination*. Science, 2007. **318**(5849): p. 447-50.
99. Hansen, K.H., et al., *A model for transmission of the H3K27me3 epigenetic mark*. Nat Cell Biol, 2008. **10**(11): p. 1291-300.
100. Hansen, K.H. and K. Helin, *Epigenetic inheritance through self-recruitment of the polycomb repressive complex 2*. Epigenetics, 2009. **4**(3): p. 133-8.
101. Lanzuolo, C., et al., *PcG complexes set the stage for epigenetic inheritance of gene silencing in early S phase before replication*. PLoS Genet, 2011. **7**(11): p. e1002370.
102. Margueron, R., et al., *Role of the polycomb protein EED in the propagation of repressive histone marks*. Nature, 2009. **461**(7265): p. 762-7.
103. Lanzuolo, C. and V. Orlando, *Memories from the Polycomb Group Proteins*. Annu Rev Genet, 2012.
104. Pollock, R.M. and V.M. Richon, *Epigenetic approaches to cancer therapy*. Drug Discovery Today: Therapeutic Strategies, 2009. **6**(2): p. 71-79.
105. Baylin, S.B. and P.A. Jones, *A decade of exploring the cancer epigenome - biological and translational implications*. Nat Rev Cancer, 2011. **11**(10): p. 726-34.
106. Portela, A. and M. Esteller, *Epigenetic modifications and human disease*. Nat Biotechnol, 2010. **28**(10): p. 1057-68.

107. Robinson, G., et al., *Novel mutations target distinct subgroups of medulloblastoma*. Nature, 2012. **488**(7409): p. 43-8.
108. Ryan, R.J. and B.E. Bernstein, *Molecular biology. Genetic events that shape the cancer epigenome*. Science, 2012. **336**(6088): p. 1513-4.
109. Shih, A.H., et al., *The role of mutations in epigenetic regulators in myeloid malignancies*. Nat Rev Cancer, 2012. **12**(9): p. 599-612.
110. Wagener, N., et al., *Enhancer of zeste homolog 2 (EZH2) expression is an independent prognostic factor in renal cell carcinoma*. BMC Cancer, 2010. **10**: p. 524.
111. Bracken, A.P., et al., *EZH2 is downstream of the pRB-E2F pathway, essential for proliferation and amplified in cancer*. EMBO J, 2003. **22**(20): p. 5323-35.
112. Takawa, M., et al., *Validation of the histone methyltransferase EZH2 as a therapeutic target for various types of human cancer and as a prognostic marker*. Cancer Sci, 2011. **102**(7): p. 1298-305.
113. van Haaften, G., et al., *Somatic mutations of the histone H3K27 demethylase gene UTX in human cancer*. Nat Genet, 2009. **41**(5): p. 521-3.
114. Dalgliesh, G.L., et al., *Systematic sequencing of renal carcinoma reveals inactivation of histone modifying genes*. Nature, 2010. **463**(7279): p. 360-3.
115. Pasqualucci, L., et al., *Analysis of the coding genome of diffuse large B-cell lymphoma*. Nat Genet, 2011. **43**(9): p. 830-7.
116. Ryan, R.J., et al., *EZH2 codon 641 mutations are common in BCL2-rearranged germinal center B cell lymphomas*. PLoS One, 2011. **6**(12): p. e28585.
117. Yap, D.B., et al., *Somatic mutations at EZH2 Y641 act dominantly through a mechanism of selectively altered PRC2 catalytic activity, to increase H3K27 trimethylation*. Blood, 2011. **117**(8): p. 2451-9.
118. Velichutina, I., et al., *EZH2-mediated epigenetic silencing in germinal center B cells contributes to proliferation and lymphomagenesis*. Blood, 2010. **116**(24): p. 5247-55.
119. Copeland, R.A., M.P. Moyer, and V.M. Richon, *Targeting genetic alterations in protein methyltransferases for personalized cancer therapeutics*. Oncogene, 2013. **32**(8): p. 939-46.
120. Simon, J.A. and C.A. Lange, *Roles of the EZH2 histone methyltransferase in cancer epigenetics*. Mutat Res, 2008. **647**(1-2): p. 21-9.
121. Okada, Y., et al., *hDOT1L links histone methylation to leukemogenesis*. Cell, 2005. **121**(2): p. 167-78.

122. Tachibana, M., et al., *Histone methyltransferases G9a and GLP form heteromeric complexes and are both crucial for methylation of euchromatin at H3-K9*. Genes Dev, 2005. **19**(7): p. 815-26.
123. McGarvey, K.M., et al., *Silenced tumor suppressor genes reactivated by DNA demethylation do not return to a fully euchromatic chromatin state*. Cancer Res, 2006. **66**(7): p. 3541-9.
124. Huang, J., et al., *G9a and Glp methylate lysine 373 in the tumor suppressor p53*. J Biol Chem, 2010. **285**(13): p. 9636-41.
125. Muntean, A.G. and J.L. Hess, *Epigenetic dysregulation in cancer*. Am J Pathol, 2009. **175**(4): p. 1353-61.
126. Ayton, P.M. and M.L. Cleary, *Transformation of myeloid progenitors by MLL oncoproteins is dependent on Hoxa7 and Hoxa9*. Genes Dev, 2003. **17**(18): p. 2298-307.
127. Huntsman, D.G., et al., *MLL2, the second human homolog of the Drosophila trithorax gene, maps to 19q13.1 and is amplified in solid tumor cell lines*. Oncogene, 1999. **18**(56): p. 7975-84.
128. Lucio-Eterovic, A.K., et al., *Role for the nuclear receptor-binding SET domain protein 1 (NSD1) methyltransferase in coordinating lysine 36 methylation at histone 3 with RNA polymerase II function*. Proc Natl Acad Sci U S A, 2010. **107**(39): p. 16952-7.
129. Brown, M.A., et al., *Identification and characterization of Smyd2: a split SET/MYND domain-containing histone H3 lysine 36-specific methyltransferase that interacts with the Sin3 histone deacetylase complex*. Mol Cancer, 2006. **5**: p. 26.
130. Wu, H., et al., *Structural biology of human H3K9 methyltransferases*. PLoS One, 2010. **5**(1): p. e8570.
131. Wagner, T. and M. Jung, *New lysine methyltransferase drug targets in cancer*. Nat Biotechnol, 2012. **30**(7): p. 622-3.
132. Clinicaltrials.gov, *Clinicaltrials.gov/show/NCT01897571*. linicaltrials.gov, 2014.
133. Daigle, S.R., et al., *Selective killing of mixed lineage leukemia cells by a potent small-molecule DOT1L inhibitor*. Cancer Cell, 2011. **20**(1): p. 53-65.
134. Innovation., o., *Drug Discover and Development. (M.S. Chorghade, Ed.), in Pharmaceutical Research and Manufacturers of America. . 2007, Hoboken, NJ, USA: John Wiley & Sons, Inc.*
135. Sundberg, S.A., *High-throughput and ultra-high-throughput screening: solution- and cell-based approaches*. Curr Opin Biotechnol, 2000. **11**(1): p. 47-53.

136. Macarron, R., et al., *Impact of high-throughput screening in biomedical research*. Nat Rev Drug Discov, 2011. **10**(3): p. 188-95.
137. Zheng, W., N. Thorne, and J.C. McKew, *Phenotypic screens as a renewed approach for drug discovery*. Drug Discov Today, 2013. **18**(21-22): p. 1067-73.
138. Drews, J., *Genomic sciences and the medicine of tomorrow*. Nat Biotechnol, 1996. **14**(11): p. 1516-8.
139. Hopkins, A.L. and C.R. Groom, *The druggable genome*. Nat Rev Drug Discov, 2002. **1**(9): p. 727-30.
140. Imming, P., C. Sinning, and A. Meyer, *Drugs, their targets and the nature and number of drug targets*. Nat Rev Drug Discov, 2006. **5**(10): p. 821-34.
141. Rask-Andersen, M., M.S. Almen, and H.B. Schioth, *Trends in the exploitation of novel drug targets*. Nat Rev Drug Discov, 2011. **10**(8): p. 579-90.
142. Carey, M.F., *Chromatin Immunoprecipitation (ChIP)*. Cold Spring Harb. Protoc., 2009.
143. Wang, J.C., et al., *Chromatin immunoprecipitation (ChIP) scanning identifies primary glucocorticoid receptor target genes*. Proc Natl Acad Sci U S A, 2004. **101**(44): p. 15603-8.
144. Ralston, A., *Examining Histone Modifications with Chromatin Immunoprecipitation and Quantitative PCR*. Nature Education, 2008.
145. Su, Z., et al., *ChIP-less analysis of chromatin states*. Epigenetics Chromatin, 2014. **7**: p. 7.
146. Schena, M., *DNA Microarrays*. 1999.
147. Cheng, C.S., et al., *Semiconductor-based DNA sequencing of histone modification states*. Nat Commun, 2013. **4**: p. 2672.
148. Sanger, F., S. Nicklen, and A.R. Coulson, *DNA sequencing with chain-terminating inhibitors*. Proc Natl Acad Sci U S A, 1977. **74**(12): p. 5463-7.
149. Sanger, F. and A.R. Coulson, *A rapid method for determining sequences in DNA by primed synthesis with DNA polymerase*. J Mol Biol, 1975. **94**(3): p. 441-8.
150. Mackeen, M.M., et al., *Small-molecule-based inhibition of histone demethylation in cells assessed by quantitative mass spectrometry*. J Proteome Res, 2010. **9**(8): p. 4082-92.
151. Britton, L.M., et al., *Breaking the histone code with quantitative mass spectrometry*. Expert Rev Proteomics, 2011. **8**(5): p. 631-43.

152. Zee, B.M., N.L. Young, and B.A. Garcia, *Quantitative proteomic approaches to studying histone modifications*. Curr Chem Genomics, 2011. **5**(Suppl 1): p. 106-14.
153. Bielefeld-Sevigny, M., *AlphaLISA immunoassay platform- the "no-wash" high-throughput alternative to ELISA*. Assay Drug Dev Technol, 2009. **7**(1): p. 90-2.
154. Machleidt, T., et al., *TR-FRET Cellular Assays for Interrogating Posttranslational Modifications of Histone H3*. J Biomol Screen, 2011. **16**(10): p. 1236-46.
155. Qian, J., et al., *Development of Multiple Cell-Based Assays for the Detection of Histone H3 Lys27 Trimethylation (H3K27me3)*. Assay Drug Dev Technol, 2013.
156. Zanella, F., J.B. Lorens, and W. Link, *High content screening: seeing is believing*. Trends Biotechnol, 2010. **28**(5): p. 237-45.
157. Denner, P., J. Schmalowsky, and S. Prechtel, *High-content analysis in preclinical drug discovery*. Comb Chem High Throughput Screen, 2008. **11**(3): p. 216-30.
158. Haney, S.A., et al., *High-content screening moves to the front of the line*. Drug Discov Today, 2006. **11**(19-20): p. 889-94.
159. Lang, P., et al., *Cellular imaging in drug discovery*. Nat Rev Drug Discov, 2006. **5**(4): p. 343-56.
160. Cho, M.H., et al., *A bioluminescent cytotoxicity assay for assessment of membrane integrity using a proteolytic biomarker*. Toxicol In Vitro, 2008. **22**(4): p. 1099-106.
161. Inglese, J., et al., *High-throughput screening assays for the identification of chemical probes*. Nat Chem Biol, 2007. **3**(8): p. 466-79.
162. Taylor, D.L., E.S. Woo, and K.A. Giuliano, *Real-time molecular and cellular analysis: the new frontier of drug discovery*. Curr Opin Biotechnol, 2001. **12**(1): p. 75-81.
163. Giuliano, K.A., *High-Content Screening: A New Approach to Easing Key Bottlenecks in the Drug Discovery Process*. J Biomol Screen, 1997. **2**(4).
164. Giuliano, K.A., *Advances in high-content screening for drug discovery*. Assay Drug Dev Technol, 2003. **1**.
165. Portugal, J. and M.J. Waring, *Assignment of DNA binding sites for 4',6-diamidine-2-phenylindole and bisbenzimidazole (Hoechst 33258). A comparative footprinting study*. Biochim Biophys Acta, 1988. **949**(2): p. 158-68.
166. Yoo, K.H. and L. Hennighausen, *EZH2 methyltransferase and H3K27 methylation in breast cancer*. Int J Biol Sci, 2012. **8**(1): p. 59-65.
167. Kubicek, S., et al., *Reversal of H3K9me2 by a small-molecule inhibitor for the G9a histone methyltransferase*. Mol Cell, 2007. **25**(3): p. 473-81.

168. Diaz, E., et al., *Development and validation of reagents and assays for EZH2 peptide and nucleosome high-throughput screens*. J Biomol Screen, 2012. **17**(10): p. 1279-92.
169. Qi, W., et al., *Selective inhibition of Ezh2 by a small molecule inhibitor blocks tumor cells proliferation*. Proc Natl Acad Sci U S A, 2012. **109**(52): p. 21360-5.
170. Verma, S.K., *Identification of Potent, Selective, Cell-Active Inhibitors of the Histone Lysine Methyltransferase EZH2*. ACS Med. Chem. Lett., 2012.
171. Knutson, S.K., et al., *Durable tumor regression in genetically altered malignant rhabdoid tumors by inhibition of methyltransferase EZH2*. Proc Natl Acad Sci U S A, 2013. **110**(19): p. 7922-7.
172. Konze, K.D., et al., *An orally bioavailable chemical probe of the Lysine Methyltransferases EZH2 and EZH1*. ACS Chem Biol, 2013. **8**(6): p. 1324-34.
173. Probes., S.G.C.C., http://www.thesgc.org/scientists/chemical_probes. SGC,2013.
174. Kondo, Y., et al., *Gene silencing in cancer by histone H3 lysine 27 trimethylation independent of promoter DNA methylation*. Nat Genet, 2008. **40**(6): p. 741-50.
175. Duquenne, C., *Indazoles*. 2011.
176. Chiang, P.K. and G.L. Cantoni, *Perturbation of biochemical transmethylation by 3-deazaadenosine in vivo*. Biochem Pharmacol, 1979. **28**(12): p. 1897-902.
177. Miranda, T.B., et al., *DZNep is a global histone methylation inhibitor that reactivates developmental genes not silenced by DNA methylation*. Mol Cancer Ther, 2009. **8**(6): p. 1579-88.
178. Reinberg, D., *Selective Inhibitors for transferases*. 2007.
179. Reinberg, D., *USPatent US2009/0306201 A1*. 2009.
180. Min, J., et al., *An oncogene-tumor suppressor cascade drives metastatic prostate cancer by coordinately activating Ras and nuclear factor-kappaB*. Nat Med, 2010. **16**(3): p. 286-94.
181. Bryant, R.J., et al., *EZH2 promotes proliferation and invasiveness of prostate cancer cells*. Prostate, 2007. **67**(5): p. 547-56.
182. Bryant, R.J., et al., *The Polycomb Group protein EZH2 regulates actin polymerization in human prostate cancer cells*. Prostate, 2008. **68**(3): p. 255-63.
183. Karanikolas, B.D., M.L. Figueiredo, and L. Wu, *Comprehensive evaluation of the role of EZH2 in the growth, invasion, and aggression of a panel of prostate cancer cell lines*. Prostate, 2010. **70**(6): p. 675-88.

184. Zhang, X., et al., *Structural basis for the product specificity of histone lysine methyltransferases*. Mol Cell, 2003. **12**(1): p. 177-85.
185. Schuettengruber, B., et al., *Genome regulation by polycomb and trithorax proteins*. Cell, 2007. **128**(4): p. 735-45.
186. Cao, R. and Y. Zhang, *The functions of E(Z)/EZH2-mediated methylation of lysine 27 in histone H3*. Curr Opin Genet Dev, 2004. **14**(2): p. 155-64.
187. Margueron, R., et al., *Ezh1 and Ezh2 maintain repressive chromatin through different mechanisms*. Mol Cell, 2008. **32**(4): p. 503-18.
188. Tachibana, M., et al., *Set domain-containing protein, G9a, is a novel lysine-preferring mammalian histone methyltransferase with hyperactivity and specific selectivity to lysines 9 and 27 of histone H3*. J Biol Chem, 2001. **276**(27): p. 25309-17.
189. Wu, H., et al., *Histone methyltransferase G9a contributes to H3K27 methylation in vivo*. Cell Res, 2011. **21**(2): p. 365-7.
190. Jenuwein, T., *The epigenetic magic of histone lysine methylation*. Febs j, 2006. **273**(14): p. 3121-35.
191. Schultz, D.C., et al., *SETDB1: a novel KAP-1-associated histone H3, lysine 9-specific methyltransferase that contributes to HP1-mediated silencing of euchromatic genes by KRAB zinc-finger proteins*. Genes Dev, 2002. **16**(8): p. 919-32.
192. Tan, J., et al., *Pharmacologic disruption of Polycomb-repressive complex 2-mediated gene repression selectively induces apoptosis in cancer cells*. Genes Dev, 2007. **21**(9): p. 1050-63.
193. Zhou, J., et al., *The histone methyltransferase inhibitor, DZNep, up-regulates TXNIP, increases ROS production, and targets leukemia cells in AML*. Blood, 2011. **118**(10): p. 2830-9.
194. Hayden, A., et al., *S-adenosylhomocysteine hydrolase inhibition by 3-deazaneplanocin A analogues induces anti-cancer effects in breast cancer cell lines and synergy with both histone deacetylase and HER2 inhibition*. Breast Cancer Res Treat, 2011. **127**(1): p. 109-19.
195. Puppe, J., et al., *BRCA1-deficient mammary tumor cells are dependent on EZH2 expression and sensitive to Polycomb Repressive Complex 2-inhibitor 3-deazaneplanocin A*. Breast Cancer Res, 2009. **11**(4): p. R63.
196. Zheng, Y., et al., *Total kinetic analysis reveals how combinatorial methylation patterns are established on lysines 27 and 36 of histone H3*. Proc Natl Acad Sci U S A, 2012. **109**(34): p. 13549-54.

197. Lindroth, A.M., et al., *Antagonism between DNA and H3K27 methylation at the imprinted Rasgrf1 locus*. PLoS Genet, 2008. **4**(8): p. e1000145.
198. Pasini, D., et al., *Characterization of an antagonistic switch between histone H3 lysine 27 methylation and acetylation in the transcriptional regulation of Polycomb group target genes*. Nucleic Acids Res, 2010. **38**(15): p. 4958-69.
199. Miller, J.H., *A short course in bacterial genetics: A laboratory Manual and Handbook for Escherichia coli and Related Bacteria*. 1992: Cold Spring Harbor Laboratory Press.
200. Rall, W.F. and G.M. Fahy, *Ice-free cryopreservation of mouse embryos at -196 degrees C by vitrification*. Nature, 1985. **313**(6003): p. 573-5.
201. Karlsson, J.O., et al., *Nucleation and growth of ice crystals inside cultured hepatocytes during freezing in the presence of dimethyl sulfoxide*. Biophys J, 1993. **65**(6): p. 2524-36.
202. Kligman, A.M., *TOPICAL PHARMACOLOGY AND TOXICOLOGY OF DIMETHYL SULFOXIDE. 1*. Jama, 1965. **193**: p. 796-804.
203. Ahkong, Q.F., *Mechanisms of cell fusion*. Nature, 1975. **253**(5288).
204. Maclean, N., *Cell Commitment and Differentiation*. 1987.
205. Yu, Z.W. and P.J. Quinn, *Dimethyl sulphoxide: a review of its applications in cell biology*. Biosci Rep, 1994. **14**(6): p. 259-81.
206. Narayan, P.J. and M. Dragunow, *High content analysis of histone acetylation in human cells and tissues*. J Neurosci Methods, 2010. **193**(1): p. 54-61.
207. Mulji, A., et al., *Configuration of a High-Content Imaging Platform for Hit Identification and Pharmacological Assessment of JMJD3 Demethylase Enzyme Inhibitors*. J Biomol Screen, 2012. **17**(1): p. 108-20.
208. Das, A.K., P.W. Cohen, and D. Barford, *The structure of the tetratricopeptide repeats of protein phosphatase 5: implications for TPR-mediated protein-protein interactions*. Embo j, 1998. **17**(5): p. 1192-9.
209. Sweet, S.M., et al., *Kinetics of re-establishing H3K79 methylation marks in global human chromatin*. J Biol Chem, 2010. **285**(43): p. 32778-86.
210. Meyer, K.D., et al., *Comprehensive analysis of mRNA methylation reveals enrichment in 3' UTRs and near stop codons*. Cell, 2012. **149**(7): p. 1635-46.
211. Dominissini, D., et al., *Topology of the human and mouse m6A RNA methylomes revealed by m6A-seq*. Nature, 2012. **485**(7397): p. 201-6.

212. He, C., *Grand challenge commentary: RNA epigenetics?* Nat Chem Biol, 2010. **6**(12): p. 863-5.
213. Yi, C., *Cellular Dynamics of RNA Modification*. Acc Chem Res., 2011. **44**(12): p. 1380-1388.
214. Denis, H., M.N. Ndlovu, and F. Fuks, *Regulation of mammalian DNA methyltransferases: a route to new mechanisms*. EMBO Rep, 2011. **12**(7): p. 647-56.
215. Amatangelo, M.D., et al., *Three-dimensional culture sensitizes epithelial ovarian cancer cells to EZH2 methyltransferase inhibition*. Cell Cycle, 2013. **12**(13): p. 2113-9.
216. Copeland, R.A., D.L. Pompliano, and T.D. Meek, *Drug-target residence time and its implications for lead optimization*. Nat Rev Drug Discov, 2006. **5**(9): p. 730-9.
217. Van Aller, G.S., et al., *Long Residence Time Inhibition of EZH2 in Activated Polycomb Repressive Complex 2*. ACS Chem Biol, 2013.
218. Chen, H., S.W. Tu, and J.T. Hsieh, *Down-regulation of human DAB2IP gene expression mediated by polycomb Ezh2 complex and histone deacetylase in prostate cancer*. J Biol Chem, 2005. **280**(23): p. 22437-44.
219. Boyer, L.A., D. Mathur, and R. Jaenisch, *Molecular control of pluripotency*. Curr Opin Genet Dev, 2006. **16**(5): p. 455-62.
220. Bracken, A.P., et al., *Genome-wide mapping of Polycomb target genes unravels their roles in cell fate transitions*. Genes Dev, 2006. **20**(9): p. 1123-36.
221. Lee, T.I., et al., *Control of developmental regulators by Polycomb in human embryonic stem cells*. Cell, 2006. **125**(2): p. 301-13.
222. Yu, J., et al., *Integrative genomics analysis reveals silencing of beta-adrenergic signaling by polycomb in prostate cancer*. Cancer Cell, 2007. **12**(5): p. 419-31.
223. Cao, Q., et al., *Repression of E-cadherin by the polycomb group protein EZH2 in cancer*. Oncogene, 2008. **27**(58): p. 7274-84.
224. Herranz, N., et al., *Polycomb complex 2 is required for E-cadherin repression by the Snail1 transcription factor*. Mol Cell Biol, 2008. **28**(15): p. 4772-81.
225. Yu, J., et al., *The neuronal repellent SLIT2 is a target for repression by EZH2 in prostate cancer*. Oncogene, 2010. **29**(39): p. 5370-80.
226. Tsang, *Epigenetic regulation of signaling pathways in cancer: Role of the histone methyltransferase EZH2*. Gastroenterology and Hepatology, 2011. **26**: p. 19-27.

- 227. Garapaty-Rao, S., et al., *Identification of EZH2 and EZH1 small molecule inhibitors with selective impact on diffuse large B cell lymphoma cell growth*. Chem Biol, 2013. **20**(11): p. 1329-39.
- 228. Boyer, L.A., et al., *Polycomb complexes repress developmental regulators in murine embryonic stem cells*. Nature, 2006. **441**(7091): p. 349-53.
- 229. Tolhuis, B., et al., *Genome-wide profiling of PRC1 and PRC2 Polycomb chromatin binding in Drosophila melanogaster*. Nat Genet, 2006. **38**(6): p. 694-9.
- 230. Schuettengruber, B., et al., *Functional anatomy of polycomb and trithorax chromatin landscapes in Drosophila embryos*. PLoS Biol, 2009. **7**(1): p. e13.